Microscopically-viewed Relationship between Structure and Mechanical Property of High-strength High-modulus Poly-*p*-phenylenebenzobisoxazole Fibers

A Doctoral Thesis

by

Tooru Kitagawa

Submitted to the Graduate School of Science,

Osaka University

February, 2001

To my wife, Hiromi

Acknowledgements

The present study has been carried out under the direction of Professor Kohji Tashiro of Department of Macromolecular Science, Graduate School of Science, Osaka University. I would like to express my gratitude to him for his cordial guidance and critical discussion. Part of works of this thesis was performed under the direction of Professor Robert J. Young of Manchester Materials Science Center, University of Manchester and UMIST (United Kingdom) to whom sincere thanks are due. I wish to express my gratefulness to Dr. Kazuyuki Yabuki of Toyobo Co., Ltd. for his continuing encouragement, directions, and critical discussion. Thanks are also extended to Dr. Katsuhiko Kato, Dr. Hiroshi Yasuda, Dr. Tohru Mizukami, Dr. Hisashi Ubara and the late Dr. Yoshinori Ogino for their kind guidance. Part of experiments and discussion in this thesis was made possible by the help and advice of Dr. Andrew C. Wright, Mr. Peter Kenway, Mr. Yasuo Ohta, Mr. Yoshihiko Teramoto, Mr. Hiroki Murase, Mr. Michio Ishitobi and Mr. Ihachiro Iba to whom thanks are extended. I would like to express my gratitude to all the members of Professor Tashiro's laboratory of Department of Macromolecular Science, Osaka University, and the members of Polymer Research Department, Zylon Department and Analytical Research Center of Toyobo Co., Ltd. Finally, I sincerely thank to Dr. Tetsuo Ukai, President of Toyobo Research Center Co., Ltd., for his kind encouragement and understanding.

Tooru Kitagawa

February, 2001

Contents

Chapter 1

General Introduction

This thesis is concerned with the mechanical properties of poly-*p*-phenylenebenzobisoxazole (PBO, commercial name Zylon™, Toyobo Co., Ltd.) fiber from the morphological point of view and its molecular structure (Figure 1-1). In 1970s the advent of poly-*p*-phenyleneterephthalamide (PPTA, commercial name Kevlar™, DuPont) fiber was a big surprise to people dealing with physical properties of synthetic fibers, because PPTA is made of the so-called extended chain structure and has high mechanical properties.[1-3] This nature depends on such a structure that the polymer has a straight molecular backbone parallel to the fiber axis with small-occupied volume in the crystal structure.[4] Control of the fiber morphology was carried out by the aid of a dry-jet wet spinning method.[5] The molecule is so rigid that it is aligned along the same direction spontaneously in the solution to form a liquid crystal. As a result it shows high crystalline orientation. Other high-modulus and high-strength fibers such as Technora™ (Teijin Co., Ltd.)[6] and Vectran™ (Kuraray Co., Ltd.)[7] made through the liquid-crystalline state, have followed the PPTA in 1980s.

There are plenty of studies[1-16] regarding morphology of high-modulus and high-strength fibers and many structural models[1-3,17,18] have been proposed to understand their excellent mechanical properties. PPTA fiber, for example, is made of small crystallites that have an angle against the fiber axis and form the pleated-sheet structure.[1,8] Selecting the heat-treatment condition under tension gives large crystallite size with an absence of the pleated-sheet structure,[8] which has higher Young's modulus close to the theoretical limit. But we still have an unresolved theme about the clarification of an intimate relationship between molecular structure, morphology and mechanical properties of the fibers.

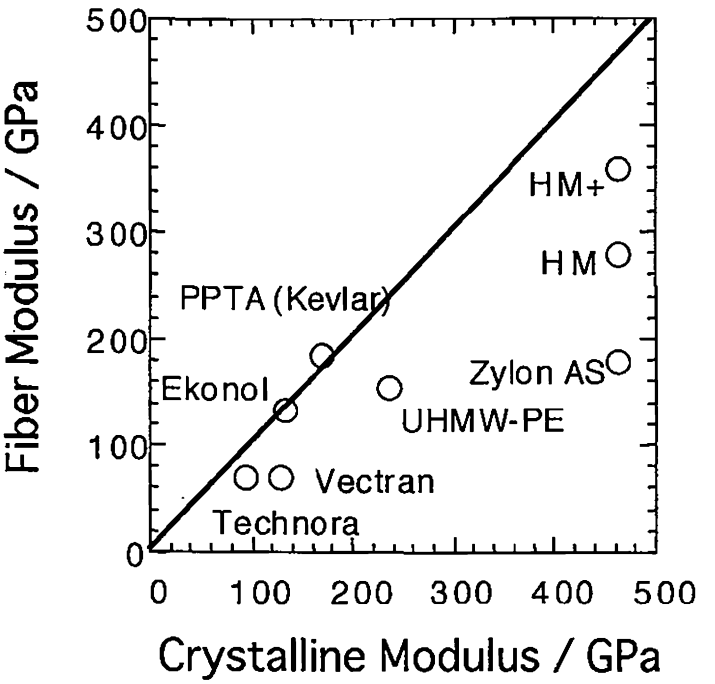

Figure 1-2. The relationship between fiber modulus and crystalline modulus for high-modulus fibers.

It is not true to conclude that only rigid-rod molecules can provide high-modulus and high-strength fibers. The fact that ultra-high molecular weight polyethylene (UHMW-PE) can be formed into a high-modulus and high-strength fiber gave another impact.[9-11] Polyethylene (PE) molecule is so flexible that the drawing ratio was limited to a certain level due to the chain entanglement in a usual melt-spinning method. As a result the mechanical properties of PE fibers were in the medium level.[10] To break such difficulty, the crystal-growth method from polymer solution was invented.[12] For industrial mass production, this invention was grown up to the gel spinning method.[9] The polymer solutions were kept in semi-dilute solution state in which the entanglement started to occur but the degree was not so much. In fact UHMW-PE fiber can be spun by the gel-spinning method to the ultra-drawn state. The mechanical properties reach very high level close to or higher than PPTA fibers. The fiber morphology[13-16] was also investigated and was revealed to be in a state of very high degree of molecular orientation with less inhomogeneity along the fiber axis.

PBO is one of rigid-rod polymers and the fiber shows highly excellent mechanical properties. This polymer has been developed by the US Air Force to search a light-weight material to replace metals for space or aviation usage.[19] As far as organic materials are concerned, neither PPTA nor UHMW-PE fibers can exceed the modulus of steel in a unit area but PBO shows the mechanical properties twice as high as PPTA and exceeds even steel in Young's modulus.[19] In addition the fiber shows excellent high heat resistance.[20,21] In order to understand this excellent physical property of PBO fiber, the structure and its relation with the physical property must be clarified in detail based on physicochemical methods and some theoretical approach.

As for the theoretical study to predict mechanical properties of polymers, many trials have been made since 1950s. One of important interests in the development of high-modulus high-strength fibers is to calculate theoretical (ultimate) modulus and

compare the value with actually-measured crystalline modulus. To do so, many theoretical techniques have been developed. The lattice dynamics is one of the most useful methods because the suitableness of molecular parameters used in the calculation can be checked and modified by vibrational spectroscopic measurements. In fact we know many cases reaching successful agreement between the observed and predicted moduli. Many research groups[22-26] (Shimanouchi et al., Miyazawa et al., Tadokoro-Kobayashi-Tashiro et al.) are devoted to developing this lattice-dynamics method to apply to polymers. In particular, Tashiro et al.[27,28] revealed the method how to trace the deformation process of molecules under stress. A method[29,30] to get the modulus by solving quantum-mechanics equations is also available. The theoretical prediction has given an incentive to synthetic-fiber manufacturers to find new materials having extremely high modulus that we have never obtained so far.

As for the crystalline modulus of PBO, Adams[31] and Tashiro[32] calculated the crystalline modulus (theoretical limit) by the semi-empirical molecular orbital calculation and the lattice dynamics, respectively. The predicted values are different from each other, but the Tashiro's value comes closer to the crystalline modulus measured by Lenhert et al.,[33] Nishino et al.,[34] and the author himself.

There have been published many morphological studies[35-46] about PBO fibers. Krause et al.[35] reported the crystallite size, microfibril texture and molecular orientation of PBO by X-ray diffraction and electron microscopic methods. The fiber is made of highly oriented but the crystallite size is small compared with that of PPTA. Shimamura et al.[36] is the first to observe the molecular chain alignment and defects included in the PBO crystal by high-resolution electron microscopy (HREM). Martin et al.[37] also examined the PBO molecular orientation and translational disorder of chains along the fiber axis by HREM and electron diffraction (ED). Crystal structure information is also important to understand the morphological characteristics and the

relation between structure and mechanical property of PBO. Fratini et al.[38] proposed the crystal structure model by X-ray study. Tashiro et al.[39] proposed another type of crystal structure model by X-ray diffraction and computer simulation methods. Takahashi[40] proposed also a model of PBO by neutron diffraction. In this way, at present, the crystal structure has not yet been established definitely. The relationship between the process and microfibril structure formation was investigated by Bai et al. and Kumar et al.[41-44] using a small-angle X-ray scattering (SAXS). Raman spectra also provide unique information on the molecular deformation caused by tensile force. Young et al.[45] applied this method to a stressed PBO fiber and estimated the Raman band shift with stress.

One of the most important problems to be solved for PBO fiber is to catch any idea to explain the difference of the limiting modulus or the crystalline modulus and the observed modulus. As mentioned above, the crystalline modulus is about 460 GPa, while the fiber shows only 180 – 360 GPa. We need to clarify the reason for this large gap between crystalline (theoretical) and fiber moduli. PBO fiber consists of fully extended chains.[36] Most of the so called super (high-modulus and high-strength) fibers also consist of highly-oriented chains and show the modulus closer to the crystalline (theoretical) modulus.[47,48] But the PBO fiber fills only 60 % of its potential even for the HM (heat-treated high-modulus type) fiber in spite of its fully extended chain structure (Figure 1-2). In general the tensile modulus of the super fibers is said to be controlled by the degree of molecular orientation.[49] It has already been found[37] that the HM fiber takes highly-oriented molecular structure, the orientation of which exceeds that of PPTA. But it was also confirmed by SAXS that the HM fiber includes periodical density fluctuation along the fiber axis.[41-43] The presence of this periodicity is one of structural characteristics of heat-treated PBO fiber produced by aqueous coagulation and has not been found in high-modulus type PPTA.[8] This periodical

PBO

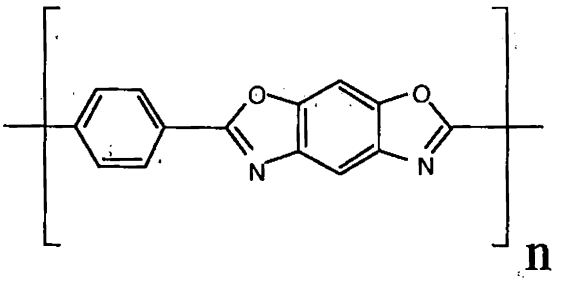

PPTA

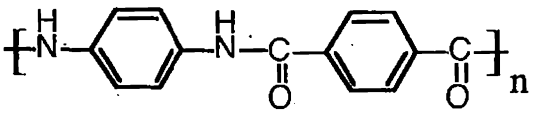

Technora

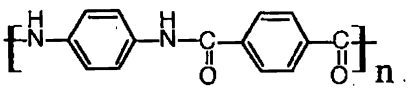

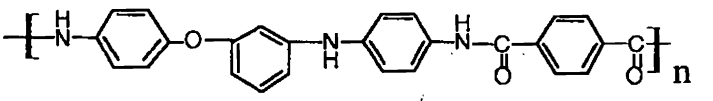

Vectran

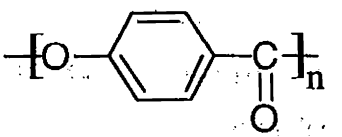

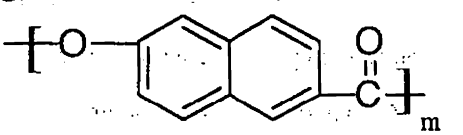

Figure 1-1. Molecular structure of high-modulus high-strength fibers.

density fluctuation may be one of the reasons to reduce the fiber modulus from the theoretical value. Translational disorder[50,51] of chains included in PBO crystal is another factor to be taken into consideration. In the case of PBO crystal the interactions between the neighboring chains are weak[52,53] because the molecular chains are connected only by the van der Waals forces and electrostatic forces. This weak intermolecular interaction might induce the slippage of the neighboring chains by applying a tension along the fiber and reduce the fiber modulus. In such a meaning, a structural investigation of the PBO chains under deformation is important to understand the mechanism of modulus improvement.

This doctoral thesis aims at clarifying the morphology of PBO fibers and relating this morphology with the mechanical property of this fiber viewed from nano-scale to crystallite scale and to molecular chain level. At the same time, the molecular deformation mechanism[54,55] is needed to be clarified by carrying out experiments for the stressed PBO fibers, which will give us a useful information on the difference of limiting modulus and fiber modulus from the molecular level. Therefore, the comprehension of this fiber from the viewpoints of deformation process and structure will suggest an idea of a certain production method to realize actual fiber modulus close to the limiting value.

This thesis consists of the following chapters. In Chapters 2 and 3, the morphology of current commercial PBO fibers (AS and HM) and a new ultra-high modulus PBO fiber (HM+) has been examined by X-ray and electron microscope methods. The fibers have been improved in tenacity than those discussed in the previous literatures.[34-45] Modulus is also improved in the newly invented HM+ fiber by 80 GPa from the HM fiber, the reason of which is discussed in these two chapters. In Chapter 4, molecular orientation change under stress is measured. Stress-strain curve is predicted and compared with the observed data. It is found that there are gaps

between the theoretically-predicted and the measured strains for the three types of fibers but the difference become less in the order of fiber modulus. In Chapter 5 the lattice distortion with stress is measured and analyzed on the basis of the theory of the second kind of disorder. The stress-induced internal strain is probed again by the Raman scattering method in Chapter 6. It is noted that PBO fiber shows not only Raman band shift but also peak broadening under stress. The rate of the broadening depends on fiber modulus. Therefore the analysis of this band broadening will be useful for the investigation of the morphology effect on the molecular deformation process. In Chapter 7, more detailed study is made for the whole range of Raman spectra. The Raman band shift factor is evaluated for many important bands and the result is compared with values calculated on the basis of the lattice dynamics under the quasi-harmonic approximation. The Raman band shifts are found to depend on the PBO fibers used in the measurement. This comes from the difference in the stress distribution in the fiber. In other words, by analyzing this difference in the Raman data, it may be possible to estimate the relation between the fiber morphology and stress distribution. In this chapter, this type of discussion is made in detail. As mentioned above, PBO is the strongest fiber among many commercially available fiber species at the current stage. Detailed interpretation of the relationship between structure, morphology and mechanical property of this fiber will give us certain good ideas to develop new polymer materials with more excellent mechanical properties.

Chapter 2

X-ray Diffraction Study of Morphological Features of PBO Fibers

2. 1. Introduction

In this chapter, morphological features of PBO fibers is studied by X-ray diffraction to understand the excellent mechanical properties. Many studies have been so far reported on morphology of PBO fibers.[35-45] The tenacity of the fibers (fiber strength) was around 3.5 - 4.9 GPa. Several years after them, the new PBO fibers (Zylon™ AS and HM) were developed by Toyobo Co., Ltd. The tenacity was remarkably higher than the previously used fibers. Improvement of mechanical property should reflect the change in the morphological structure of the fibers. Therefore it is necessary to reinvestigate the relation between morphology and mechanical property in detail. The purpose of this chapter is to clarify the characteristic features of various grades of PBO fibers from the morphological point of view.

2. 2. Experimental

2. 2. 1. Samples

Commercially available PBO fibers (Zylon™) produced by Toyobo Co., Ltd. and a newly prepared PBO fiber were investigated. The AS fiber was spun from polyphosphoric acid solution (dope). The solution was extruded from the spinneret and coagulated in the phosphoric acid bath followed by the washing and the drying processes. The production method is illustrated in Figure 2-1. The HM fiber was produced by heat treatment (600 ℃) from the AS fiber. To increase the fiber modulus

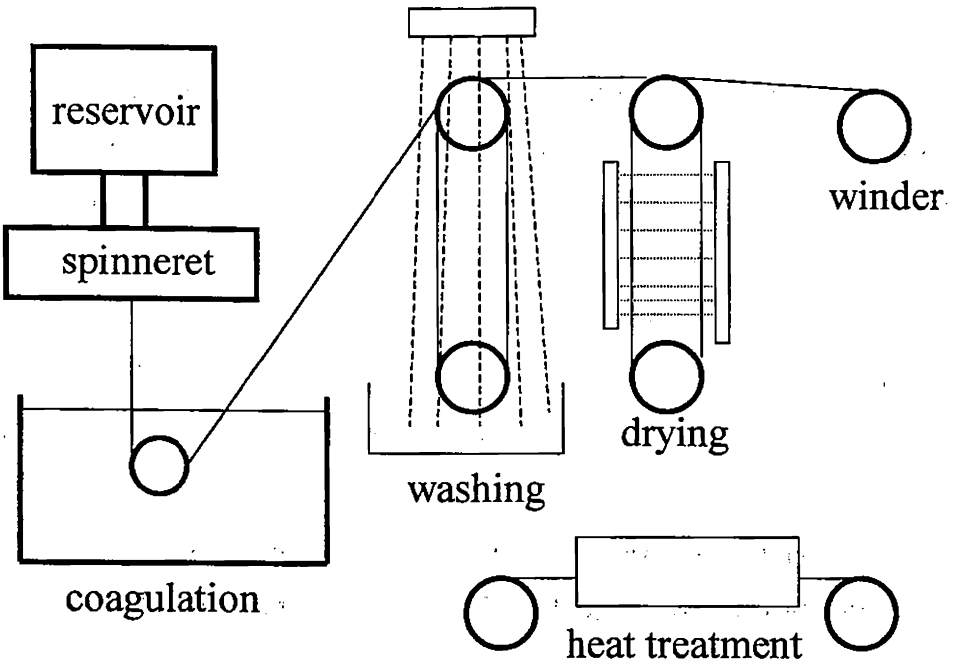

Figure 2-1. Schematic diagram of production facility for PBO fibers.

further, extruded dope filaments were coagulated in the non-aqueous liquid followed by washing, drying and heat-treatment processes, just when solution concentration and composition is same for the commercial fibers. Thus prepared fiber (named as HM+) showed higher modulus with slightly lower strength than the HM fiber.

Intrinsic viscosities for these fibers were measured in methanesulfonic acid saturated with methanesulfonic anhydride. The results for AS and HM fibers were 28 dl/g (118,000 in molecular weight) and 25 dl/g (101,000), respectively; the molecular weights were estimated with the aid of the viscosity equation proposed by Roitman et al.[56]

2. 2. 2. Tensile Properties

Tensile tests were performed on a Tensilon RTM-250 manufactured by Orientec. The sample length was 20 cm and the strain rate was 20 cm per minute. A yarn (166 filaments or 32 filaments) was used for a sample. It was twisted before measurement at the twist factor (*TF*) of 6.0. *TF* is defined as follows.

$$TF = 0.131 \times TPI \times (\text{Denier})^{0.5} \qquad (2\text{-}3)$$

where *TPI* is the turn of twist per inch. The fiber strength (tenacity) was defined as the stress at break. Young's modulus was calculated from the slope of a stress-strain curve in the range from 0.1 to 1.0% elongation. At least 20 yarn samples were measured for each fiber. The result is summarized in Table 2-1. A stress-strain curve for a single filament was also measured and will be presented in Chapter 6. This measurement was performed without giving any twist to the filament (*TF* = 0) and allowed us to discuss the fine shape of the stress-strain curve.

Table 2-1. Mechanical properties of sample PBO fibers (yarns).

	Strength	Modulus	Density
	GPa	GPa	g/cm^3
AS	5.55	187	1.54
HM	5.59	258	1.56
HM+	4.72	352	1.56

Table 2-2. Apparent crystallite size estimated by X-ray diffraction methods.

	D_{app}(Å)		
	(200)	(010)	(003)
AS	55	27	96
HM	110	42	160
HM+	110	46	162

2. 2. 3. Wide-angle and Small-angle X-ray Scattering

The X-ray generator (Rigaku RU-200 rotating anode type) was operated at a power of 40kV x 100mA. The nickel-filtered CuK_α point-collimated beam was used as an X-ray source. WAXS and SAXS patterns were recorded on a flat imaging plate with the camera distances of 40 to 80 mm and 360 mm, respectively. The pinhole collimator for WAXS is 0.15 mm in diameter. A yarn (166 filaments or 32 filaments) of 100 to 500 cm in length was wound on a sample holder. To avoid scattering and absorption by air, a helium gas chamber was used. The sample yarn and the imaging plate were installed in the chamber. Also the goniometer system (Rigaku RAD-rA) with a pulse height analyzed proportional counter was used for the measurement of WAXS profiles on the equatorial and the meridional directions of the fiber sample with the symmetry-transmission method. The diameter of the pinhole collimator was 1mm. The scattered intensities were recorded at 0.2 degrees. The SiO_2 powder was used as a standard to correct for instrumental source beam broadening.

A curve fitting method was applied to estimate half widths of WAXS peaks β_0. A linear combination of Gaussian and Lorentzian functions was adopted for this fitting. The shape of the combination fitted well an observed profile. Then apparent crystallite size (D_{app}) was computed by Scherrer's equation

$$D_{app} = 0.9 \lambda / \beta_0 \cos\theta \qquad (2\text{-}1)$$

where λ is the wavelength of the CuK_α beam, β_0 the half width of the WAXS peak expressed in radian unit after the incident beam broadening correction, θ the half of the scattering angle.

Orientation of crystallites was also analyzed from a WAXS pattern. First, azimuthal intensity distribution of the (200) diffraction was computed from two-

dimensional imaging WAXS data. The distance between the sample and the imaging plate for registry was fixed at 80 mm for all orientation measurements. A straight yarn (166 filaments) was used as a sample without winding. Then the orientation distribution parameter of the crystallite principal axis $<sin^2 \phi>$ was calculated according to the following equation

$$<sin^2 \phi> = \int I(\phi) sin^3 \phi d\phi \; / \int I(\phi) sin \phi d\phi \qquad (2\text{-}2)$$

where ϕ is the azimuthal angle to the fiber axis, $I(\phi)$ the intensity distribution of the (200) diffraction along the azimuthal direction.

2. 2. 4. Imaging Plate Equipment and Data Processing

An imaging plate (FDL UR-V by Fuji Film Co., Ltd.) was used as a recording media for X-ray measurements. Two-dimensional data from the instruments were read out by microluminography (JEOL, PixsysTEM) and processed on a Hewlett-Packard engineering workstation. The data were also calculated on a Macintosh personal computer.

2. 3. Results and Discussion

2. 3. 1. Extended Chain Structure

Fiber diagrams of AS, HM, and HM+ fibers are shown in Figure 2-2. The patterns for the three fibers are the same in principal. Fratini et al.[38] proposed a crystal structure model of PBO for X-ray crystallography. The diffraction spots measured were indexed according to their model. Some sharp diffraction spots on the equator and streak-like layer lines were observed. Off-axis spots were not observed clearly.

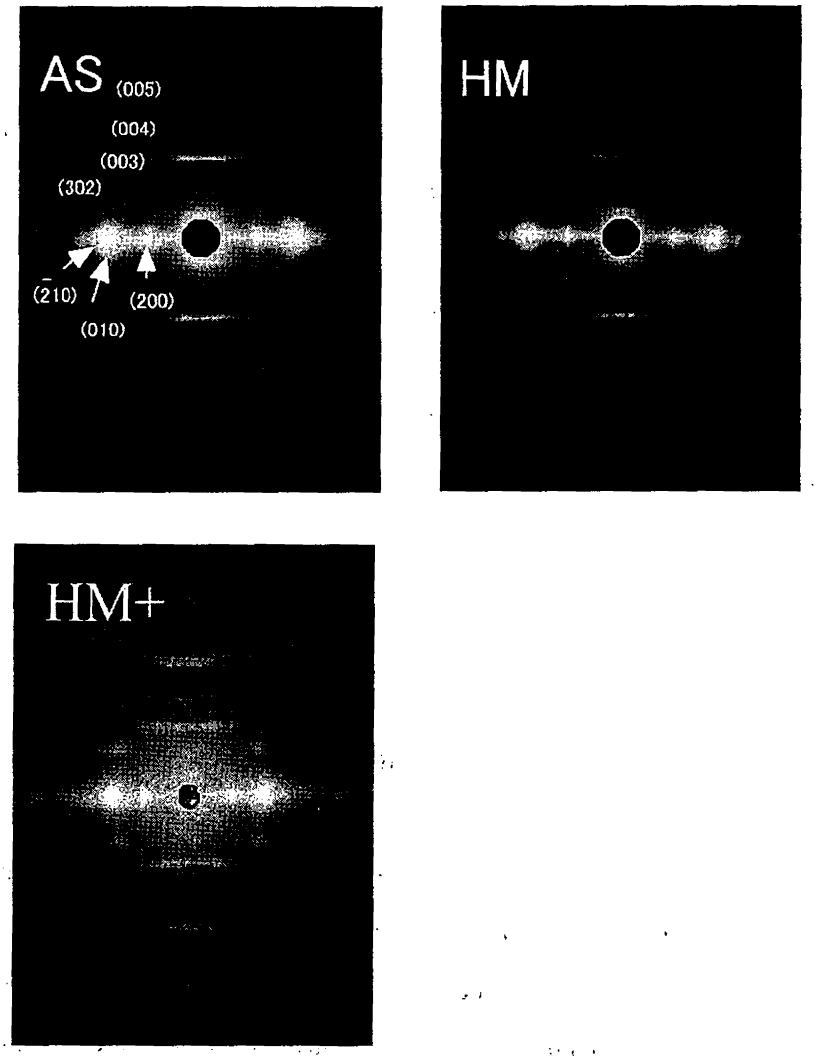

Figure 2-2. Fiber diagrams of the AS, HM and HM+ fibers. The vertical direction of the photographs is set to the fiber direction. The indices are assigned after Fratini's PBO crystal model.

Note that these features do not change much by heat treatment. Some authors[50,51] relate the streak-like layer lines on fiber diagrams to a spatial disorder of crystal along the fiber axis. Shimamura et al. proposed a model to explain such translational disorder on PBZT fiber and named the disorder as axial shift.[57,58] The shape of the spots on the equator was very sharp along the azimuthal direction. It indicates that the alignment of molecules in the PBO fiber is extraordinarily parallel to the fiber direction. The relationship between molecular orientation improvement and fiber modulus is further discussed in the next section. X-ray diffraction intensity profiles measured by the symmetry-transmission method are shown in Figure 2-3. After heat treatment the diffraction spots became sharp and intensified, indicating that the apparent crystallite size was larger. It is interesting to note that the HM+ fiber shows the narrowest peak profiles among the three fibers, implying that the fiber has the biggest crystallite size among them. The estimated apparent crystallite sizes for the three fibers are tabulated in Table 2-2.

2. 3. 2. Molecular Orientation and Fiber Modulus

In general, it is considered that Young's modulus of fibers made of rigid-rod polymers highly depends on the crystal orientation. Northolt et al.[59] proposed a mechanical model on crystal orientation variation under tension for poly-*p*-phenyleneterephthalamide (PPTA) fibers. According to their model, the fiber is regarded as being built up of a parallel array of identical fibrils which are subjected to a uniform stress along the fiber axis. A crystallite in the fibrils is composed of rigid-rod polymer chains running linearly and having an angle with the fiber axis. The effects of the molecular stretch and the orientation change of the molecules were considered in this model. The inverse of the fiber modulus (compliance) can be expressed as a linear function of crystal orientation as follows:

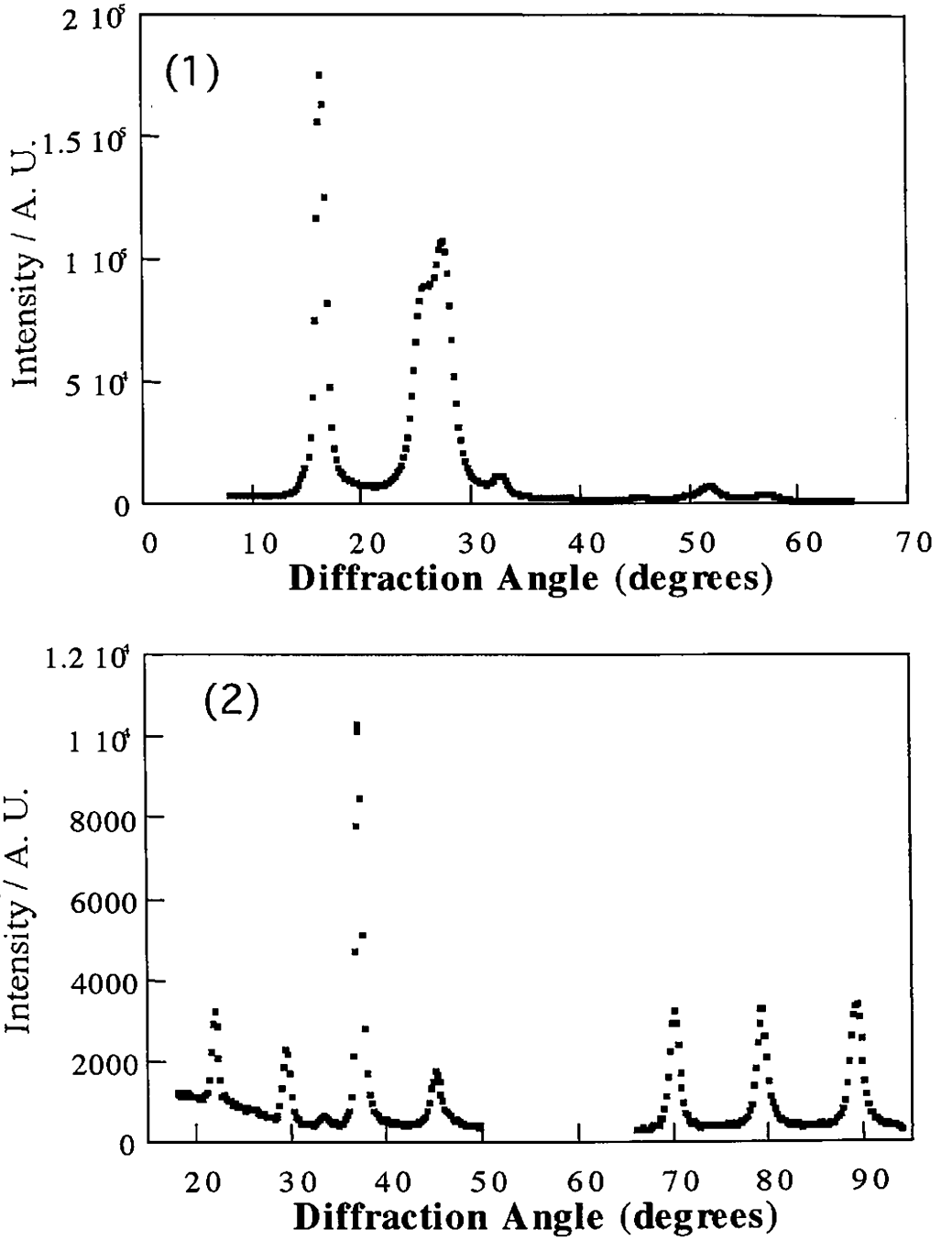

Figure 2-3. Wide-angle X-ray scattering profiles for the HM+ Fiber. (1): Equatorial (2): Meridional.

$$1/E = 1/E_c^{true} + \langle \sin^2 \phi \rangle / 2G \qquad (2\text{-}4)$$

where E is Young's modulus of the fiber, E_c^{true} is the crystalline modulus, G is the shear modulus due to the change of the molecular orientation (the rotation of the crystallites) and ϕ is the angle between the chain axis and the fiber axis. This equation is valid when ϕ is close to zero. The relationship between the applied stress and induced fiber strain on the basis of Northolt's model is given in Chapter 4. They mentioned that the intercept of the measured compliance plotted against orientation $\langle \sin^2 \phi \rangle$ agreed well with the PPTA crystalline modulus.

In order to see whether PBO also follows Northolt's idea, the inverse of Young's modulus for many PBO fibers produced under different processing conditions is plotted against $\langle \sin^2 \phi \rangle$ in Figure 2-4. The crystalline modulus and the shear modulus can be estimated to be 370 GPa and 4 GPa, respectively, from the intercept and the slope of the straight line fitted to the plotted points.

Nishino et al.,[34] Lenhert et al.[33] and the author himself (Chapter 4) measured the crystal strain of Zylon™ HM fiber under tension by X-ray diffraction. They concluded that the measured crystalline modulus was 460 - 480 GPa, which was far higher than that predicted on the base of Northolt's model. This means that Young's modulus of the PBO fiber can not reach the measured crystalline modulus even if all the molecules in the fiber are aligned completely parallel to the fiber direction. PBO fiber contains some disordered region, which would hinder achievement of crystalline modulus as fiber modulus if molecules are perfectly aligned. It is plausible that Northolt's model is too simple to express the modulus of PBO fiber adequately. Some

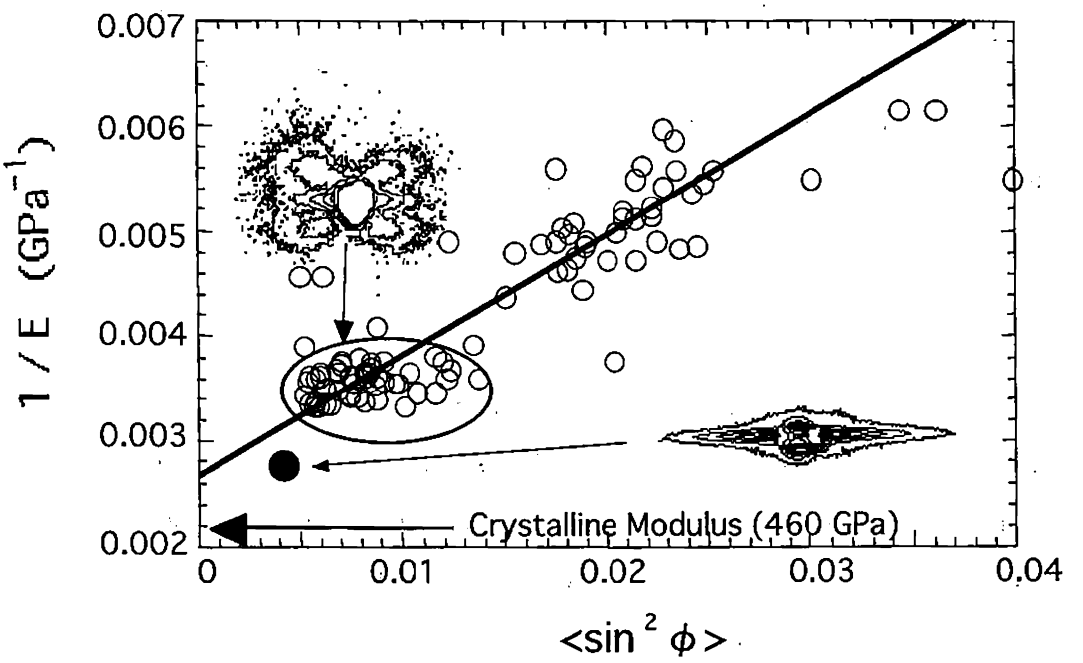

Figure 2-4. The inverse of PBO Young's modulus against <sin^2 ϕ>. ○: coagulated through aqueous phosphoric acid. ●: coagulated through non-aqueous solution.

modification of Northolt's model may be necessary to explain the fiber modulus of PBO quantitatively.

Recently, Martin et al.[60] proposed a model which explains the possibility that a chain end of PBO crystal induced onset of micro strain and contributes to reduction of the Young's modulus. We certainly observed discontinuity of the lattice fringes in the high-resolution electron microscope photograph as discussed in the next chapter even for HM+, implying an existence of the chain end. To understand the modulus as a function of orientation, the effect of disordered region such as discontinuity of the lattice should be taken into consideration.

2. 3. 3. Fine Structure

Current commercial PBO fiber is spun from using an air-gap wet spinning technology. On a coagulation process, fiber structure formation through phase separation should occur. Cohen et al.[61-64] have studied the structure formation of PBZT fiber and film. According to their explanation, firstly doped filaments extruded from a spinneret transforms to swollen microfibrillar network when the nematic rigid-rod solution touches a coagulant. Passing through the coagulation process in the second, the network loses their open spaces and forms dense fibrillar structure. Resident open spaces should become microvoids.

Figure 2-5 shows SAXS patterns of AS and HM fibers. In the AS fiber, streak-like scattering pattern, which would come from microvoids elongated to the fiber direction, appears on the equator. During the heat treatment process this streak disappears and the four-point pattern similar to the shape of a butterfly appears, indicating the existence of density fluctuation along the fiber axis. This kind of striation was reported on PPTA fiber.[49] Bai et al.[42] and Kumar et al.[44] reported the same four-point patterns on their heat-treated PBO fibers. It is interesting that HM

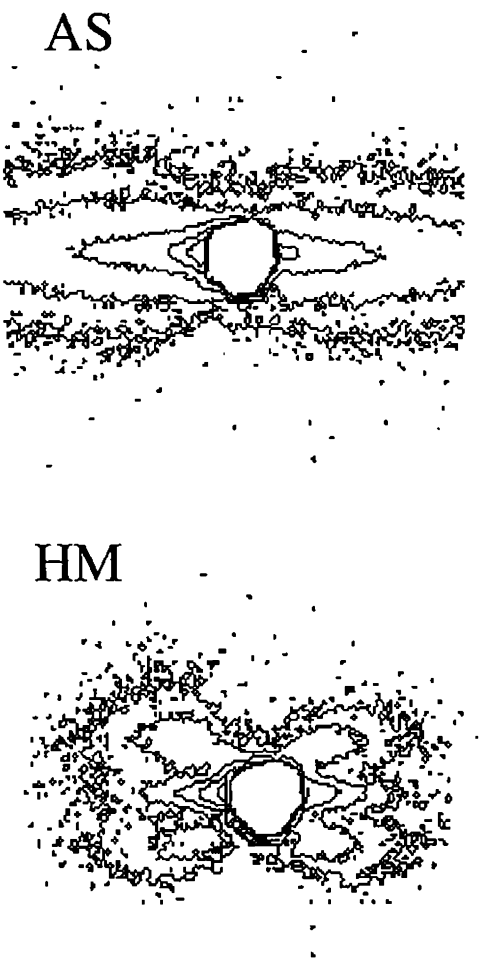

Figure 2-5. SAXS patterns for the AS and HM fibers.

fiber, even stronger than the former fibers in tenacity, shows the same pattern. In the case of high-strength polyethylene fiber,[16] this periodic density fluctuation acts as a weak point on tensile strength.

Because PBO is spun through the process of phase separation,[5] the fiber includes microvoids. In order to estimate the size of the diameter of microvoids of PBO fiber, we tried Guinier's method. Figure 2-6 shows the Guinier plot for AS fiber. An intensity profile along the equator was taken from a two-dimensional SAXS pattern. The logarithm of the intensity after background correction is plotted against the square of the scattering vector. The data exhibit linearity and the slope allows us to give the average diameter of the microvoids, about 24 Å.

The four-point pattern proves the existence of density fluctuation along the fiber axis. Tsvankin et al.[65] proposed an equation that is able to simulate a SAXS pattern pertaining to the fibril structure model. Yabuki et al.[66] modified their equation to be applicable to a fiber having cylindrical symmetry. Figure 2-7 shows the best-fit computed pattern for the PBO four-point SAXS pattern. This implies that inclined periodicity as a parallelogram (250 Å in the long period, 200 Å in the width of the fibril and 60 degrees of the oblique angle) exists in the fiber. The measured dimension of the parallelogram is close to the simulated result. Concerning the origin of the oblique angle, some reports mentioned that the parallelogram came from the shape of three-dimensional PBO crystal and the specific boundary of the (302) plane was strengthened during heat treatment.[37] Martin et al.[37] referred to the necessity to investigate dark-field (DF) images of the (302) plane but the validity is still speculative and further study is necessary.

Figure 2-8 shows the SAXS pattern of the HM+ fiber. It should be noted that HM+ is also made through heat treatment but has no four-point pattern that is characteristic of HM (heat-treated PBO fiber with aqueous coagulation).[42,44] It means

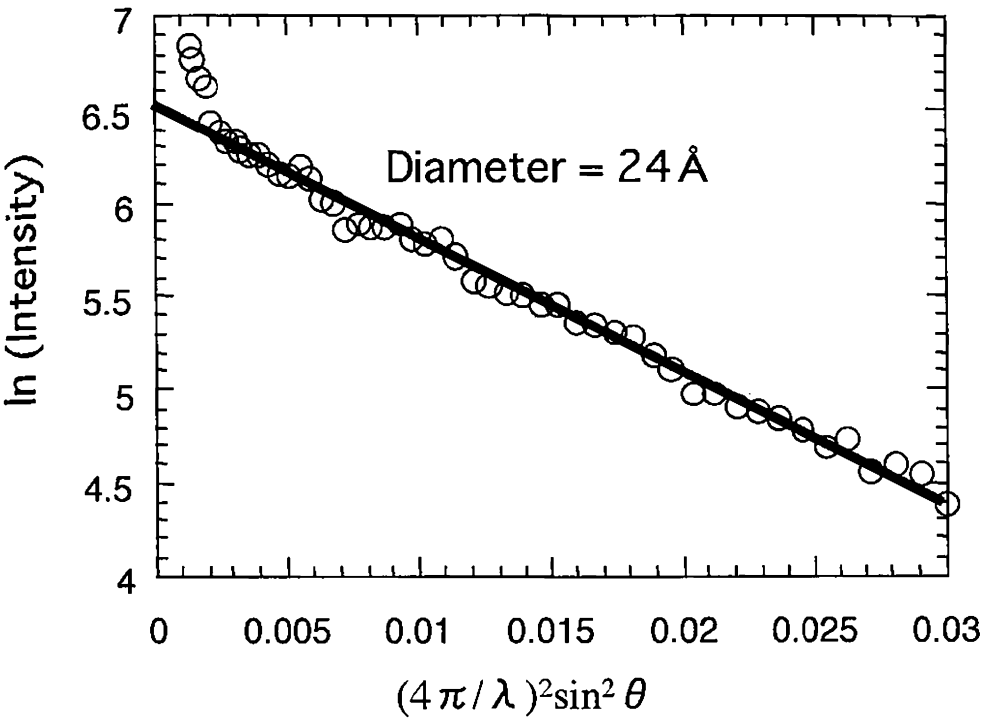

Figure 2-6. Guinier plot for the equatorial streak of SAXS pattern on the AS fiber. Here, λ is the wavelength of the CuK_α line and θ the half of the scattering angle.

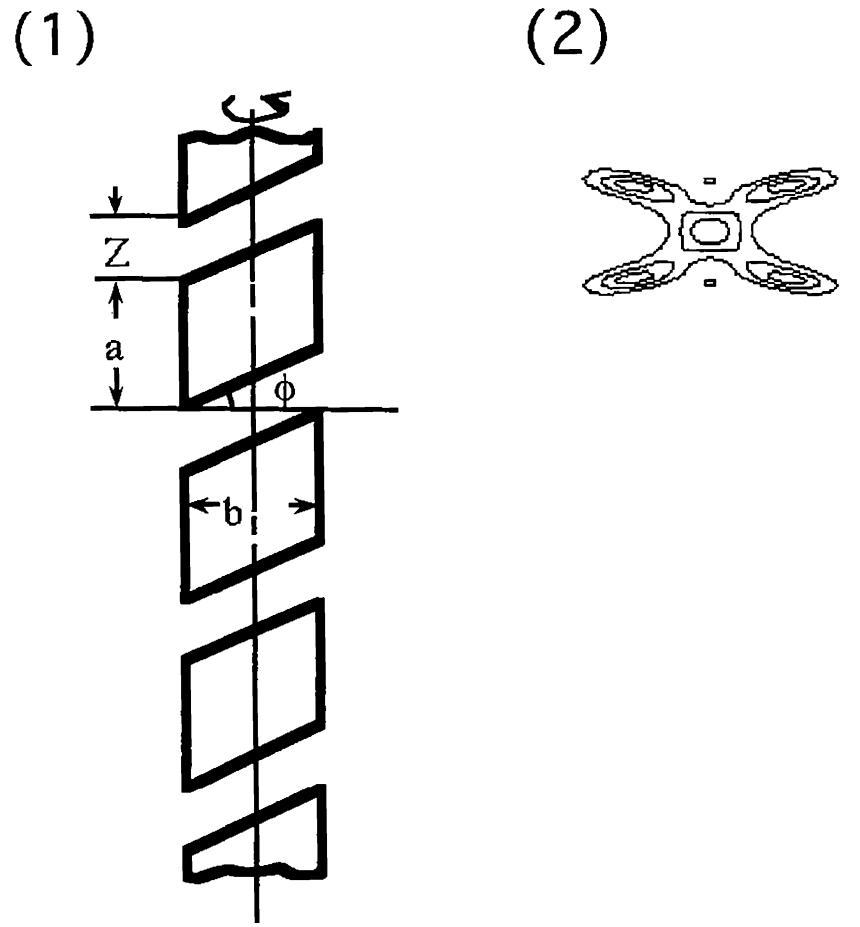

Figure 2-7. (1) Modified Tsvankin's fibril model. (2) Calculated SAXS pattern, a=14nm, b=f=20nm, Z=11nm, ϕ=60° . Here, ϕ represents the depth of the parallelogram-like body vertical to the lines expressed as a and b on the figure.

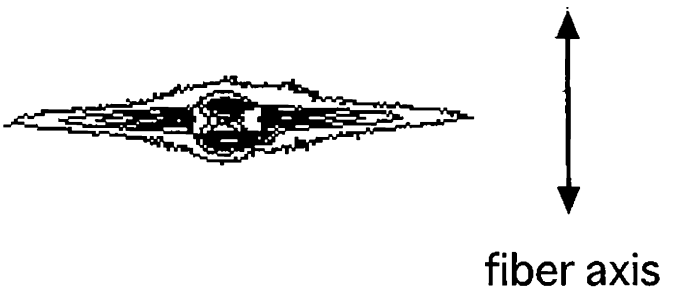

Fiber 2-8. SAXS pattern for the HM+ fiber.

that more homogeneous structure is realized along the fiber axis in the HM+ fiber. It is also noted that the SAXS pattern shows strong equatorial streak as the AS fiber but the size of microvoids is definitely larger (~2 nm) as seen from the analysis by Guinier's method. The source of this streak is unclear, however, improving crystallite size in the fibril of the HM+ fiber would accompany more enhanced boundary than the AS fiber and give such a SAXS streak.

2. 4. Conclusions

Morphological survey was carried out by WAXS and SAXS methods in this chapter. It is interesting to find that Northolt's theory is not good enough to explain the relationship between fiber modulus and molecular orientation but there seems to be unclear intimate correlation between them, which will be investigated again in the consecutive chapters. The second point to be memorized is that the HM+ fiber, which was firstly invented in this study, shows less density fluctuation along the fiber axis as clarified by the analysis of SAXS pattern. Homogeneity in the fiber direction may play an important role to improve fiber modulus.

Chapter 3

Morphology of PBO Fibers Surveyed by Transmission Electron Microscope

3. 1. Introduction

In the previous chapter the morphological characteristics were investigated for the PBO fibers of various treatments by carrying out WAXS and SAXS measurements. More direct observation[35-37, 67] of the morphological structure may give us more useful information necessary for the clarification of relationship between structure and excellent mechanical property. In this chapter, the fiber structure of PBO is observed directly by using a transmission electron microscope (TEM). Selected-area electron diffraction (SAED) patterns, dark-field (DF) image, and high-resolution electron microscope (HREM) images are taken. For samples the PBO HM and PBO HM+ are adopted. Main concern will be focused on structural features that give high modulus and the absence of the SAXS four-point pattern in HM+ fiber.

3. 2. Experimental

3. 2. 1. Transmission Electron Microscopy

In order to prepare a section for TEM observation from the HM and HM+ fibers, the detachment method was adopted.[35] A very thin fragment suitable for TEM observation can be obtained easily from the surface of PBO fibers by detachment. A sample preparation method is mentioned as follows. A solution of collodion (Fisher Scientific UK) that was diluted by three times with iso-amyl acetate was spread onto a glass slide. Sample fibers were placed on the wet collodion immediately and then allowed them for one night to dry solvent up. A solidified collodion membrane with

fibers could be seen on the glass slide. Next the fibers were removed from the collodion by lifting and it was possible to see regions of faint color in the collodion from thin fragments of fibers. A square of 3mm x 3mm region was cut out from the surface with a razor blade and placed onto a 300 mesh copper grid with holey carbon film (Nisshin EM Co., Ltd. or Agar Scientific Ltd.) with the fragment-attached face down. The grid was kept in petridishes with iso-amyl acetate vapor for 24 hours to dissolve collodion. We tried to make a thin section of the AS fiber by detachment but the prepared fragment was not thin enough to give good images by electron microscopic observation.

SAED patterns and DF images were taken on a Philips CM-20 electron microscope at 200 kV and recorded on Agfa Scientific EM (23D56) film. The camera distance for electron diffraction (ED) was 986 mm (corrected for measuring diffraction patterns from thin gold layer) and a magnification for DF was 15,000. High-resolution electron microscope (HREM) images were obtained on a Phillips TEM-430 electron microscope at 300 kV of accelerated voltage and recorded on Kodak SO-163 film with a magnification of 59,000. To make a correction for astigmatism, a live Fourier-transform pattern of granularity on carbon support film on a television monitor screen was made circle at x 200,000 with the aid of the TVIPS TEM Imaging and Image Analysis System. When good focus was obtained in a given area, the illumination beam was once deviated from the area of interest for one minute, then brought it back, and photographs were taken. The reason the above procedure was adopted is to prevent the draft due to frictional movements of the sample stage from ruining the quality of the images. The total time when the given area was exposed to the beam including focus adjustment was kept within 35 % of the radiation damage lifetime. The exposed negative was developed with Kodak D19 developer at full-strength concentration. To digitize information in the negative into a computer form, a

standard magnifier together with a lens (x 5) and a Hewlett Packard Scan Jet ADF scanner was used. To achieve multi-enlargement, an image (x 5) was once printed on a TEM film plate with the standard magnifier and then a x 25 image was re-exposed from the developed x 5 TEM film plate on a printing paper. Or the negatives were taken shots directly on a CCD (Sony XC77CE) camera with a Olympus 50 mm macro lens (x 18). Digital data were processed with Scion Image on a personal computer.

3. 2. 2. Microtoming and Selected-area Electron Diffraction

In order to see skin-core molecular orientation difference, fibers were prepared for transmission electron microscopy (TEM) by microtoming.[45,68] A commercial Spurr epoxy resin was adopted to embed fibers and kept in an oven at 60 ℃ for 24 hours for curing. Then the resin block was microtomed to get ultrathinsections with a Reichert Ultracut E ultramicrotome and a Diatome diamond knife with a cutting angle of 45 degrees. At first, it was polished and trimmed with a freshly made glass knife into a trapezium shape with the fiber at the tip. Then the fiber was microtomed along the direction perpendicular to the fiber axis. The sections so obtained were collected on a 300 mesh copper grid with holey carbon film (Nisshin EM Co., Ltd. or Agar Scientific Ltd.), or collected on a 300 mesh copper grid (Agar Scientific Ltd.) followed by thin carbon coating before inspection. A Philips CM-20 electron microscope was operated at 200 kV to generate SAED patterns with a 0.3 μm selected-area aperture at a camera distance of 986 mm that was corrected for measuring ED diffraction patterns of thin gold layer. The beam intensity was kept at relatively low level to avoid damage. Diffraction patterns were registered on Agfa Scientific EM (23D56) film. The degree of molecular orientation in the diffraction pattern was measured with using a Joyce-Loebl Chromoscan 3 microdensitometer. The data-processing procedure was mentioned in the reference.[68]

3. 3. Results and Discussion

3. 3. 1. Selected-area Diffraction Patterns

High molecular orientation of the PBO fibers can be confirmed in ED patterns (Figure 3-1). As we will report in the latter part of this chapter by ED, the HM+ fiber has high orientation especially in the skin part of the fiber on a ED pattern of an ultramicrotomed section. This also supports the reason why the ED pattern for HM+ shows so sharp diffraction spots.

3. 3. 2. Dark Field Images

With using the beam tilt method,[57] dark-field images are constructed and shown in Figure 3-2. Diffraction spots of the (200), (010), and $(\bar{2}10)$ spots were used for taking DF images of PBO. We can see that there are a lot of small crystallites in the pictures appearing as shining part as reported previously.[35] Average crystallite size was estimated from these figures and they are also tabulated in Table 3-1. There is not big size difference between the PBO HM and HM+.

If we inspect the figures precisely in the direction parallel to the fiber axis, small crystallites can be found aligned along the fiber axis. The series of crystallites is considered to be formed from stackings of shining (crystal) and dark regions that do not satisfy the Bragg condition, which may be amorphous region or crystallites including defects. This alternative stacking structure has been already reported in the previous work.[35] The average distance between crystallites along the fiber axis are 3.13 nm (standard deviation = 0.74) for HM and 3.45 nm (standard deviation = 0.99) for HM+.

It is interesting to compare this stacking structure with Tsvankin's fibril model[65] proposed for PBO HM fiber deduced from the SAXS four-point pattern in Chapter 2. One of characteristics of this model is that the fibril is composed of stackings of rhombohedron structure. The source of contrast giving the SAXS pattern has not been

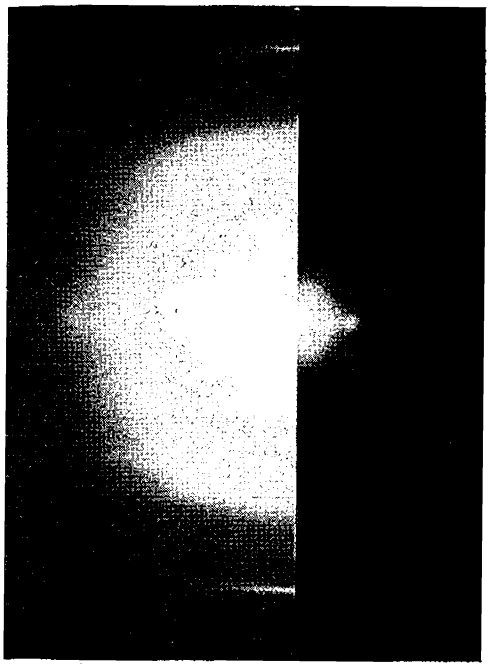

HM

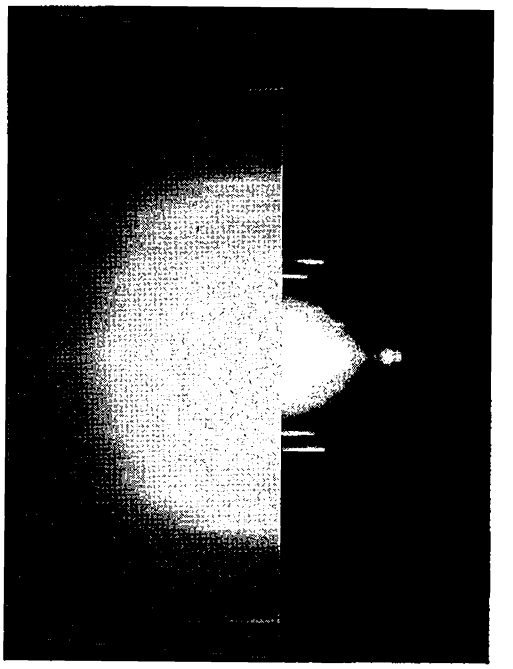

HM+

Figure 3-1. Electron diffraction patterns for the PBO fibers (detachment method). Left half of the figures adopts long exposure time in print to make the weak diffraction spots visible.

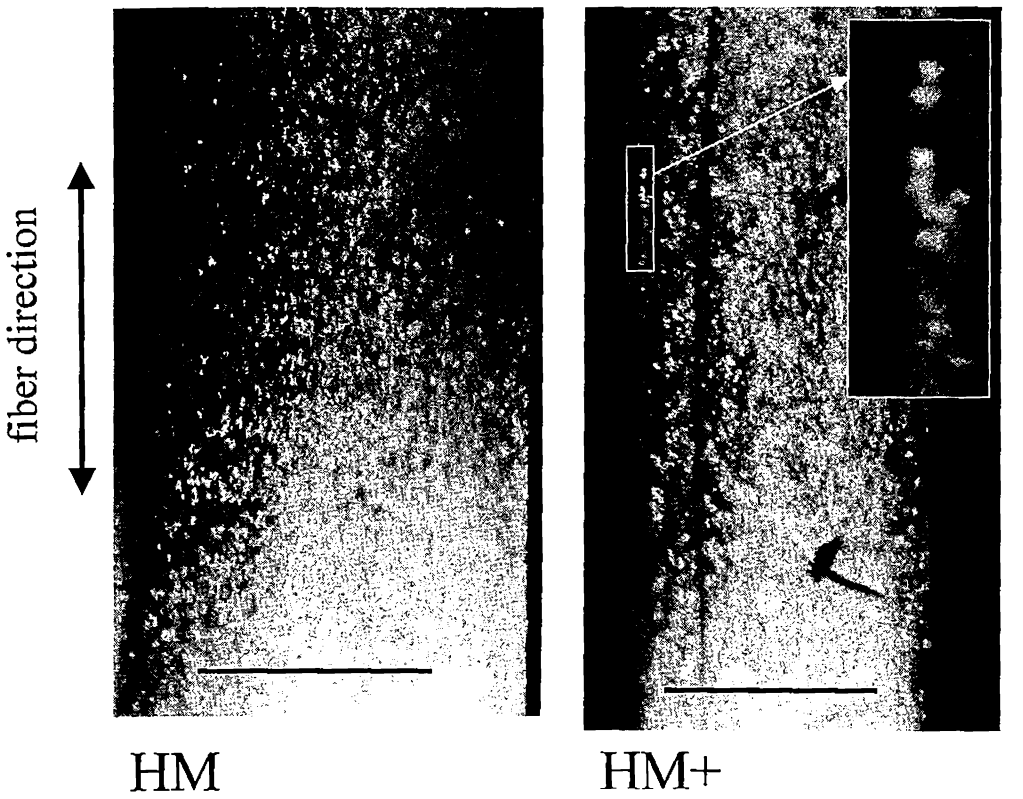

Figure 3-2. Dark field images for the PBO fibers (detachment method). The bars in the figures indicate 500nm in length. A magnified image is inset in the figure.

Table 3-1. Crystallite size of the PBO fibers estimated by dark-field image.

Fiber	HM	HM+
Transverse direction		
Size (nm)	6.69	6.82
Axial direction		
Size (nm)	4.37	4.73

Table 3-2. Molecular orientation estimated from HREM image

Fiber	HM	HM+
Crystal length (nm)	14	22
Orientation angle (degrees)	1.25	0.96
$\langle sin^2 \phi \rangle$	4.79×10^{-4}	2.78×10^{-4}

understood well actually but is considered as contrast of both order and disorder in the crystal region. The size obtained in this DF method is definitely smaller than the estimated values on Tsvankin's fibril model (A 20 nm wide fibril with the meridional periodicity of 13nm long ordered part and 12 nm long amorphous part in the fibril direction). The DF images represent just the (200), (010) and ($\bar{2}$10) planes of PBO. Tsvankin's model suggests the presence of density fluctuation along the fiber axis. It is noted that the crystallites coexist with the disordered part in such a microscopic level.

3. 3. 3. High Resolution Lattice Imaging

Microscopic molecular orientation and observation of defects are mainly carried out with using a high-resolution lattice imaging technique.[36,57] Figure 3-3 shows the HREM images obtained for PBO HM and HM+. In PBO HM and HM+, the lattice fringes of 0.55 nm in spacing is visible. At first, molecular orientation angle is evaluated. The definition[37] of the molecular orientation is an average angle between adjacent crystallites or the domains encircled by solid lines in the image. The average crystallite length along the fiber axis is also estimated, the values so obtained are tabulated in Table 3-2. It is found that PBO HM+ has the smaller molecular orientation angle value than HM and this angle is less than 1 degree. The values of orientation angle estimated from HREM are smaller than those estimated by X-ray methods. The reason for the difference of orientation angle estimated by different methods is unclear and might depend on the area of the fiber focused by X-ray or electron to get images; the value obtained from X-ray represents the average for much wider area than those of ED and HREM.

Crystallite length along the fiber axis is estimated from the persistence length of (200) lattice fringes (average length of the crystallites along the fiber axis) and the result is tabulated in Table 3-2. We understand that the PBO HM+ fiber shows longer

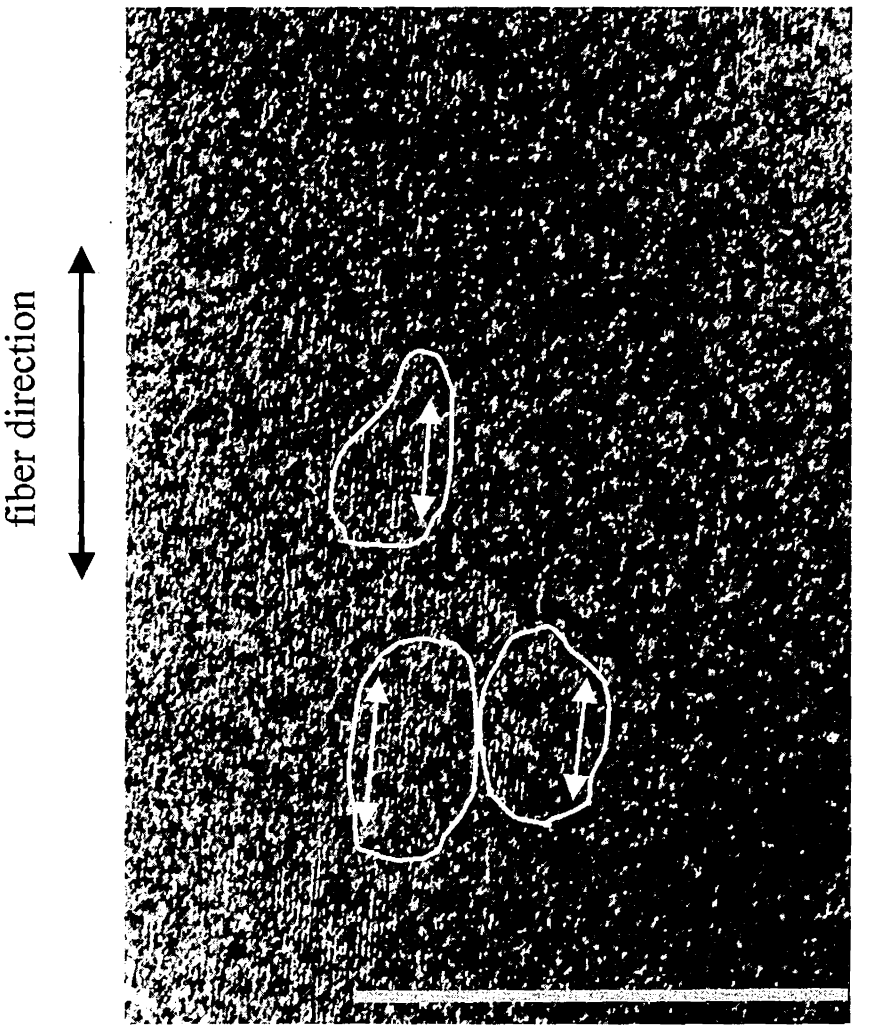

Figure 3-3. High-resolution electron microscope images (detachment method). Bars in the figure show 50 nm in length. Local molecular orientation of 0.55 nm lattice fringes is shown by arrows.

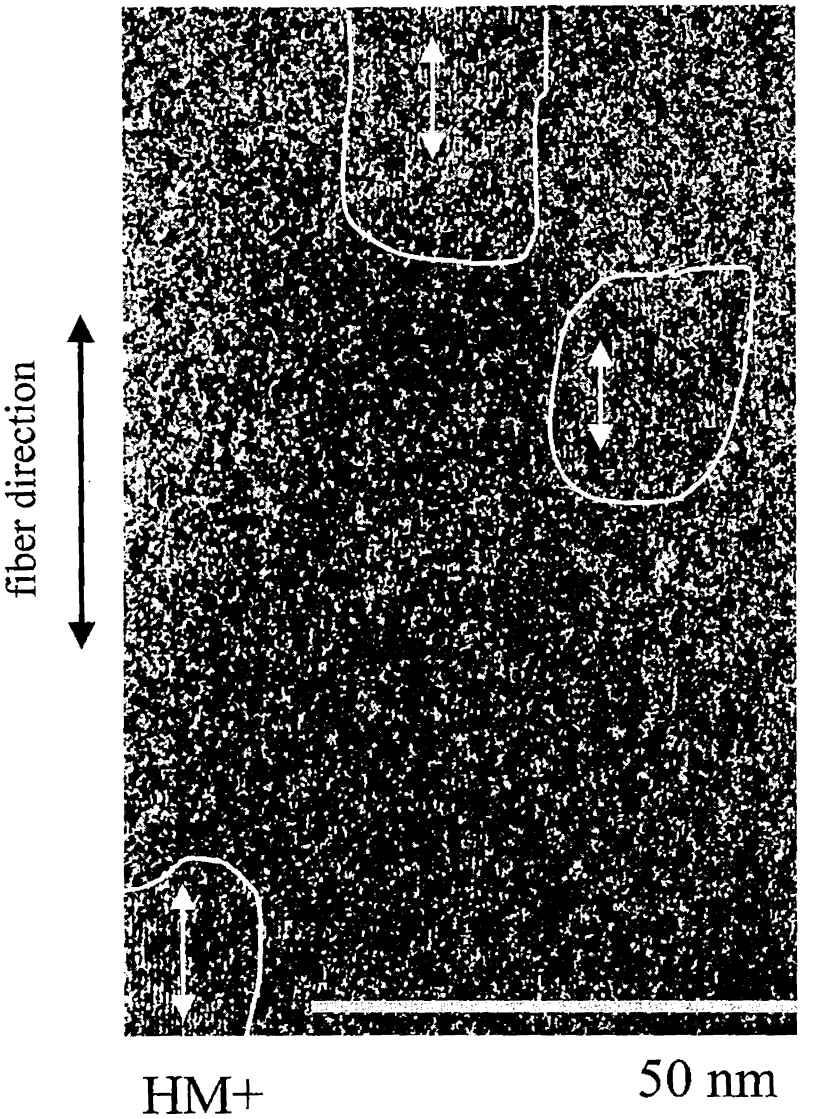

Figure 3-3. Continued.

persistence length in the fiber axis than the HM fiber. It is possible to explain that the reason why the HM+ fiber shows so high modulus from these microscopic high orientation and longer crystallite size. This idea may also explain an absence of the SAXS four-point pattern (Chapter 2), because this well-packed structural feature in HM+ can give less contrast in electron density fluctuation.

If we inspect the image closely along the fiber axis, we can confirm defects in the lattice images. One of such typical examples is shown in Figure 3-4. The same kind of structure is found commonly to both the HM+ and HM fibers. In the figure, there is a part in which one of molecules disconnects and lattice fringes disappears in the neighboring region of the chain ends. Neighboring molecules seem to run through without scission in the no-fringe region. This kind of structure has been already reported by Shimamura et al.[36,57] but the fact that even HM+ fiber has such structure should be noted. This structure feature may be the origin that prevents fiber modulus from achieving the theoretical limit. The length of the disordered region is around 3 - 10 nm, which is shorter than the length of disordered region deduced in Tsvankin's fibril model for PBO HM fiber calculated from the SAXS four-point pattern (Chapter 2). The source of electron density fluctuation giving SAXS scattering may come from conformational irregularity such as chain scission, because the electron density of the disordered region might be lower than the crystal region. We can not find any periodical patterns that may give the SAXS pattern along the fiber axis. To find the relationship between Tsvankin's model and the PBO crystalline structure (such as the stacking of crystallite in DF), we need to proceed further precise inspection.

As we have already confirmed in DF images, small crystallites are lined up along the fibre axis up to 15 in maximum, but the lengths of crystallites and amorphous parts in the fiber axis are smaller than the estimated sizes by Tsvankin's analysis. One of maneuvers for such studies will be to observe the sixth layer lines with a DF technique,

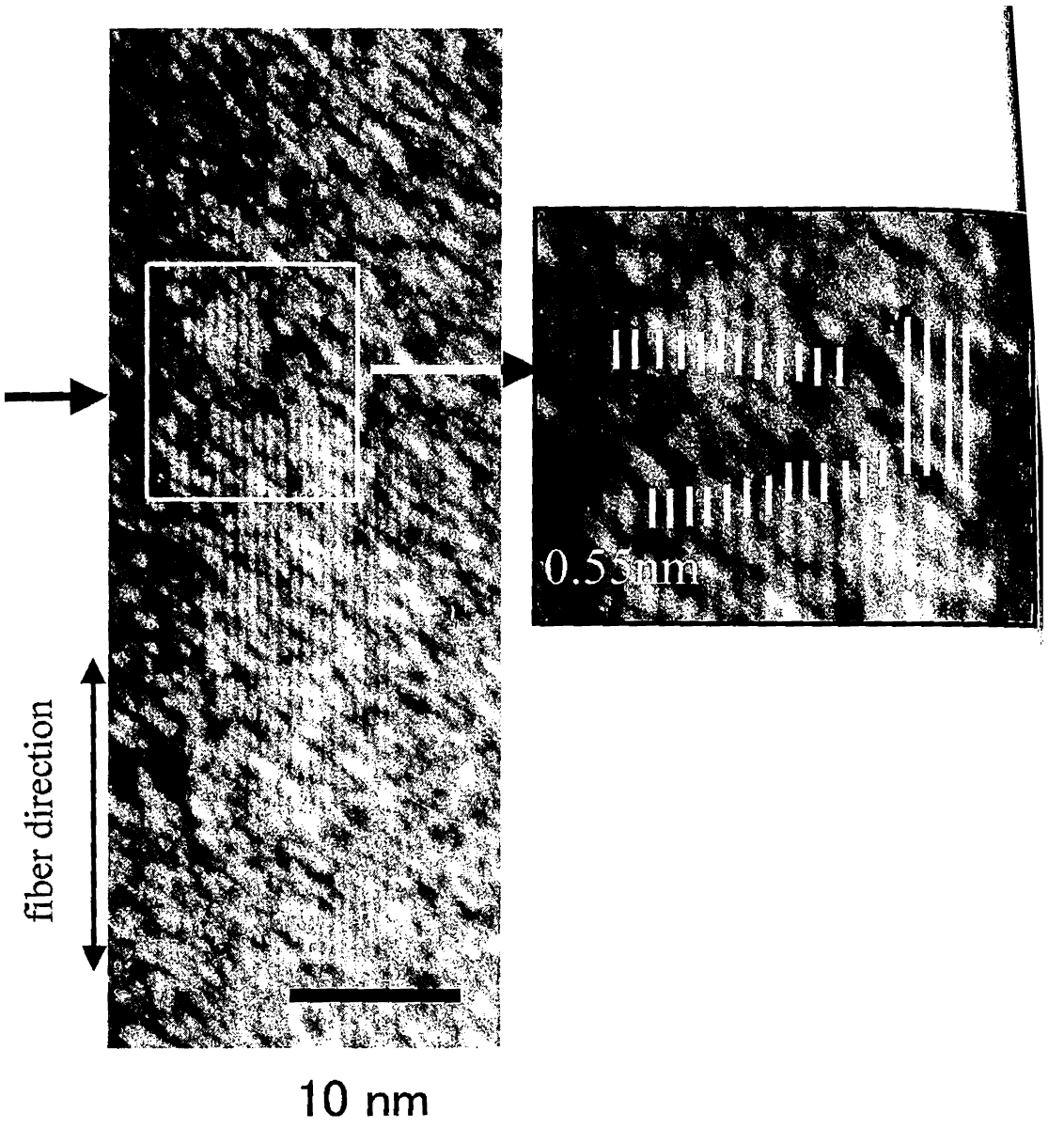

Figure 3-4. Magnification of HREM image for the HM+ fiber (detachment method). The arrow in the figure points the region in which the 0.55 nm lattice fringes fade away.

because the splitting becomes clearer as the fiber modulus is increased in the HM+ fiber and may have some relation with structural feature. The layer lines may reflect the nature of molecular alignments along the fiber axis more directly than the spots on the equator. Another possibility is to try a defocus-contrast method,[69] which enables us to see a direct image proving the density fluctuation inside the fiber structure.

3. 3. 4. Selected-area Electron Diffraction and Molecular Orientation

In this section, we inspect structural difference between skin and core regions in the fiber. In order to elucidate molecular orientation distribution along the radial direction in the cross-section of the fiber, SAED was adopted and the results are shown in Figure 3-5 for HM and in Figure 3-6 for HM+. From the spreads of diffraction spots on the equator along the Debye ring (azimuthal direction) we can estimate molecular orientation distribution.[68] If comparison is made between skin and core regions, the diffraction spots in core expands more than those in skin. Concerning crystallographic structure indexing, we follow Fratini's model[38] and the outer spots on the equator can be characterized as a combination of (010) and $(\bar{2}10)$ diffraction spots. In the bright-field images of Figures 3-5 and 3-6, we can find that the fibers are composed of elongated microfibrils and the diameter is around 100 nm, which value is confirmed to be the same as the AS fiber. There is no big difference in the bright field images between skin and core regions, and also between the AS, HM and HM+ fibers. The result is so similar that the BF and SAED images of the AS fiber are omitted here. It is confirmed that there is not serious knife marks running along the diamond knife movement direction in the bright-field photographs. We believed that suffering damage during cutting the sections was minimized and ED patterns are reliable.

In order to quantify the molecular orientation,[68] the beam spreads of outer spots in ED was digitized with a densitometer along the scanning direction parallel to the

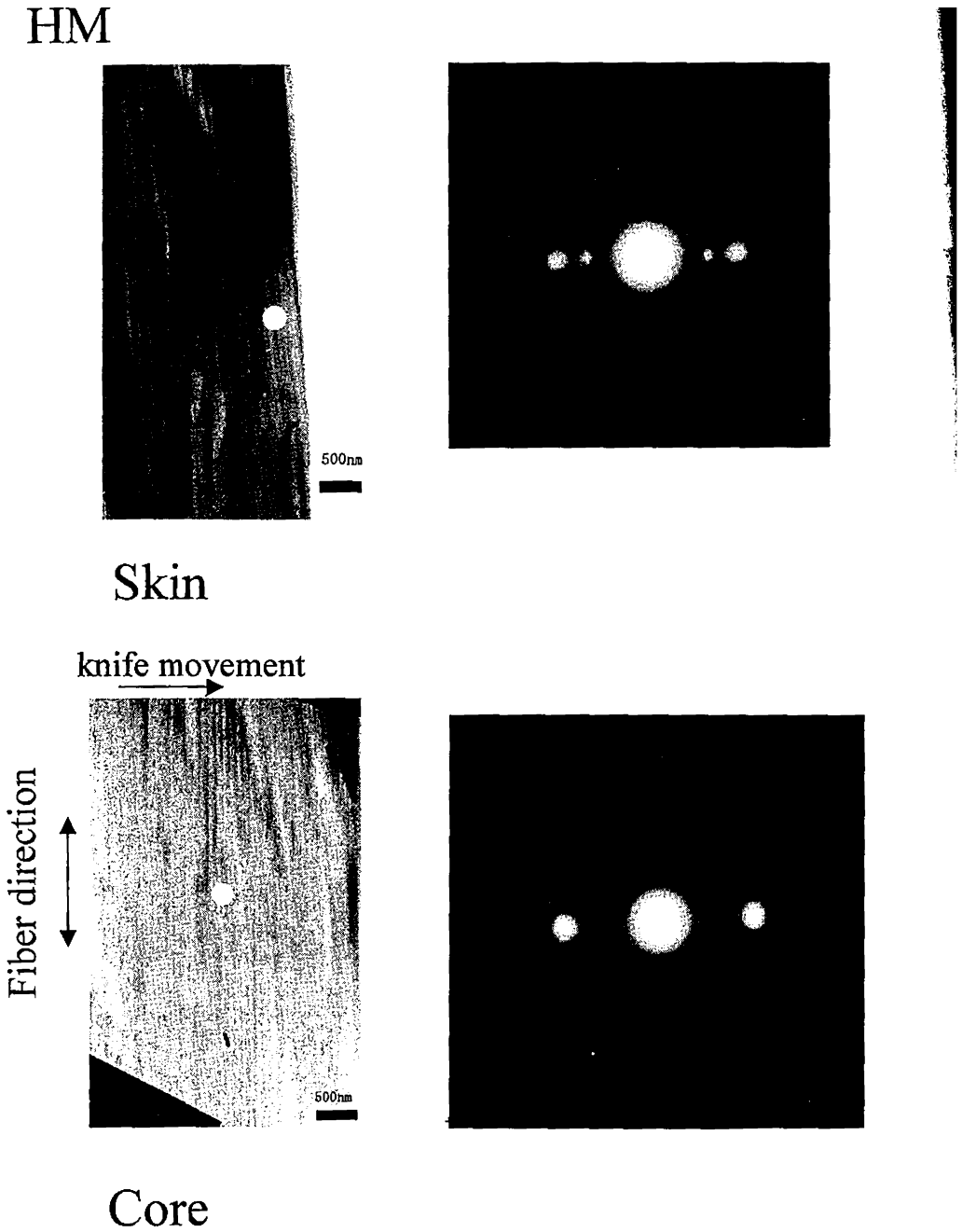

Figure 3-5. Bright field images and electron diffraction patterns for the HM fiber (microtome method). The difference between skin and core is also compared.

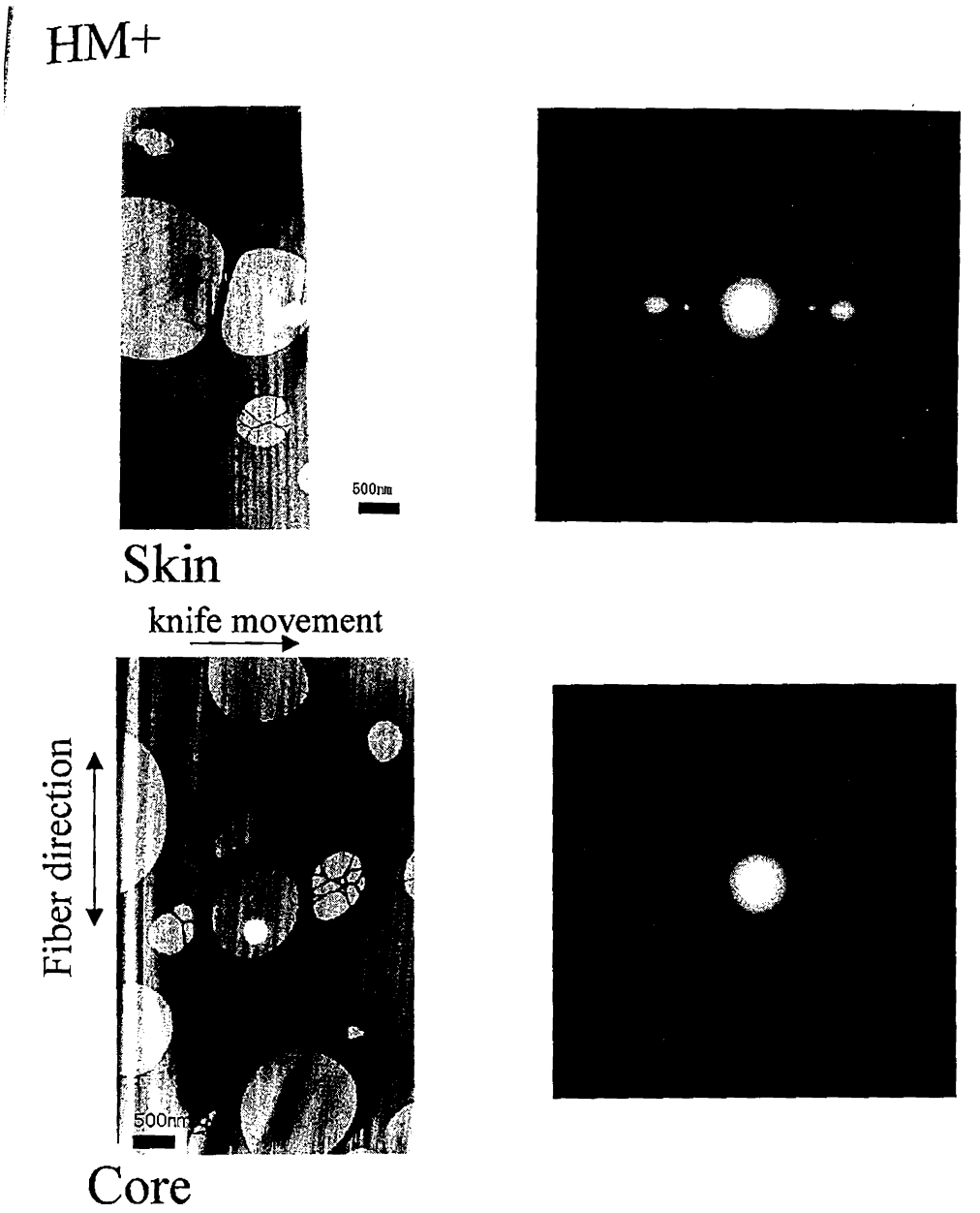

Figure 3-6. Bright field images and electron diffraction patterns for the HM+ fiber (microtome method). The difference between skin and core is also compared.

meridian. Full width at the half-height maximum (FWHM) of the profile is estimated as a measure of molecular orientation and the averaged $<sin^2 \phi>$ is also calculated with the equation proposed by Northolt et al.[59] The detail of the calculation is mentioned in Chapter 2. The distribution thus estimated is plotted in Figure 3-7 against the distance from the core along the radial direction in the cross-section. It is found that orientation in the skin becomes smaller in the order of AS > HM > HM+. There exists little difference in the skin-core structural between the AS and HM fibers as Young et al.[45] reported. And the HM+ fiber shows more enhanced skin-core difference among the three fibers. It seems to be reasonable because the fiber is produced by non-aqueous coagulation, which accompanies relatively slow phase separation process in structure formation.

In order to calculate the average molecular orientation, the values of $<sin^2 \phi>$ at five different positions in the radial direction are averaged with weighting the square of radii. The results are summarized in Table 3-3. HM+ shows the smallest value of molecular orientation in the average values. If we compare the $<sin^2 \phi>$ values of this work with those of X-ray diffraction spots in Chapter 1, we can see that the order is the same but the estimated values of this work are bigger than those of the X-ray study, respectively. It is possible to assume that the reasons for such a difference come from neglect of center beam broadening correction, adopting different diffraction spots to the X-ray study, and scanning intensity distribution along the direction parallel to the meridian (not along the Debye ring) for orientation estimation from ED patterns. A previous paper about PPTA fibers shows the same tendency.[68]

The presence of the skin-core structural difference gives fiber modulus reduction in general.[68] But in PBO case the fiber modulus depends so intensely on molecular orientation (as revealed by average from ED patterns) and homogeneous structure along the fiber axis (SAXS) and therefore HM+ may still keep the highest value among the

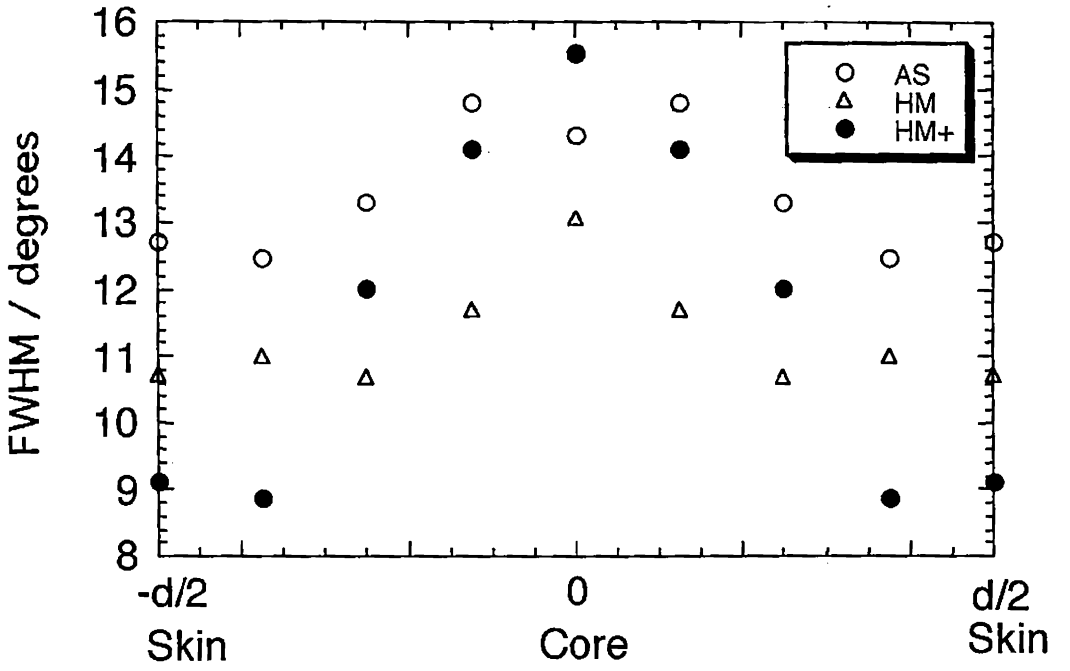

Figure 3-7. Half-height width of the azimuthal intensity distribution of equatrial diffraction spots on the ED patterns is plotted against the radial axis. *d* denotes the diameter of the sample fiber.

Table 3-3. Skin-core difference of molecular orientation estimated by ED with microtomed sections.

Fiber	AS	HM	HM+
Orientation Angle[a] (degrees)			
Skin	12.7	10.7	9.13
Core	14.3	13.1	15.6
Average	12.9	10.9	10.0
$\langle \sin^2 \phi \rangle$			
ED (average)	0.0268	0.0191	0.0161
X-ray	0.0217	0.00833	0.00361

a : Orientation angle is defined as the half width of intensity distribution of the equatorial diffraction spots in ED.

three fibers. If this molecular orientation distribution is suppressed into flat along the radial direction, modulus might be improved more.[68] To maximize modulus by erasing the skin-core structure difference, re-designing the process condition in non-solvent coagulation bath should be inevitable in the future as a new process technology.

3. 4. Conclusions

The PBO HM and HM+ fibers were inspected with a transmission electron microscope. It is found that the HM+ fiber shows higher molecular orientation and longer crystallite length along the fiber axis, which may explain the reason why HM+ gives higher modulus (360 GPa) than HM fiber (280 GPa) and possibly has relation with an absence of the SAXS four-point pattern. It should be also noted that HM+ has more noticeable skin-core difference than AS and HM. Alternative stacking structure of crystallites along the fiber axis is also confirmed in the three fibers, which means a presence of incomplete crystal in the fiber. The structure observed in the ED patterns is similar in periodicity to Tsvankin's fibril model deduced from the SAXS four-point pattern of HM fiber but there is a disagreement in dimension. It is confirmed in HREM that there are defects as disconnection of the lattice fringes in the PBO crystal, which gives relatively small crystallites and a presence of disordered parts in the fiber structure. This would cause fiber modulus reduction from the limiting value.

Chapter 4

Molecular Orientation Change of PBO Fibers Induced by Stress and its Effect on Tensile Strain

4. 1. Introduction

In the previous two chapters, morphological features of the PBO fibers have been discussed by X-ray diffraction and electron microscopy. It is understood that very high molecular orientation of the PBO fiber contributes to high fiber modulus. But there is still a gap toward the theoretical limit even in the HM+ fiber. The reason has been ascribed to the existence of a disordered part in the fiber structure, which is proved by ED and HREM observations in references[36,57] and in Chapter 2. To put more precise insight on this problem, it is important to see how crystallites in the fiber are deformed under tensile stress. This information[70-80] might point out what kind of fibers generates stress and contributes to the modulus reduction. Therefore, in this chapter, the change of fiber structure feature is examined by WAXS for the stressed fiber. The main concern is to evaluate to what extent the molecular orientation changes and how the fiber is deformed in the direction parallel to the fiber axis. Apparent crystalline modulus is also estimated by measuring a change in the Bragg spacing and the comparison of the result is made among the three PBO fibers.

4. 2. Experimental

The commercial PBO fibers (Zylon™ AS (standard type), HM (high modulus type)) and a newly prepared ultra-high modulus PBO fiber (HM+) were investigated. Intensities of X-ray diffraction from the stressed PBO fiber was measured with a

conventional X-ray diffractometer combined with an in-house stress apparatus. A Rigaku RU-200 rotating-anode type X-ray generator was used together with a goniometer (Rigaku Rad-rA system). Ni-filtered CuK_{α} ($\lambda = 0.1548$ nm) line was generated at a power of 40 kV x 100 mA . To put stress on the sample fiber (250 – 500 denier) along the fiber axis, it was fixed to the stress apparatus with screws and epoxy resin at the both ends. The block diagram for the apparatus is illustrated in Figure 4-1. Then the apparatus was mounted on a wide-angle X-ray goniometer to collect scattering intensities from the meridian of the fiber. To measure diffraction angle of the (00m) layer lines (m is integer) with precision, palladium powder was spread on the sample fiber and the diffraction spots of the PBO fiber were measured together with those of palladium in the same diffraction-angle range of imaging plate. For measurement of molecular orientation change of the (200) diffraction spot, the stress apparatus was set on a Rigaku three-point slit small-angle X-ray camera. Those diffraction profiles were registered on an imaging plate (Fuji FDL UR-V) and the measured intensities were read out with a digital microluminography (JEOL PixsysTEM). To estimate half-height width (FWHM, full width at the half-height maximum) and peak top position of the intensity profile along the Debye ring of the (200) diffraction spot with accuracy, measured intensity profiles were approximated with a linear combination of Gaussian and Lorenzian functions. The orientation parameter $<sin^2\phi>$ was calculated with using the following equation:

$$<sin^2\phi> = \int I(\phi) sin^3\phi \, d\phi \; / \int I(\phi) sin\phi \, d\phi \qquad (4\text{-}1)$$

where $I(\phi)$ is the diffraction intensity distribution of the (200) spot along the azimuthal direction.

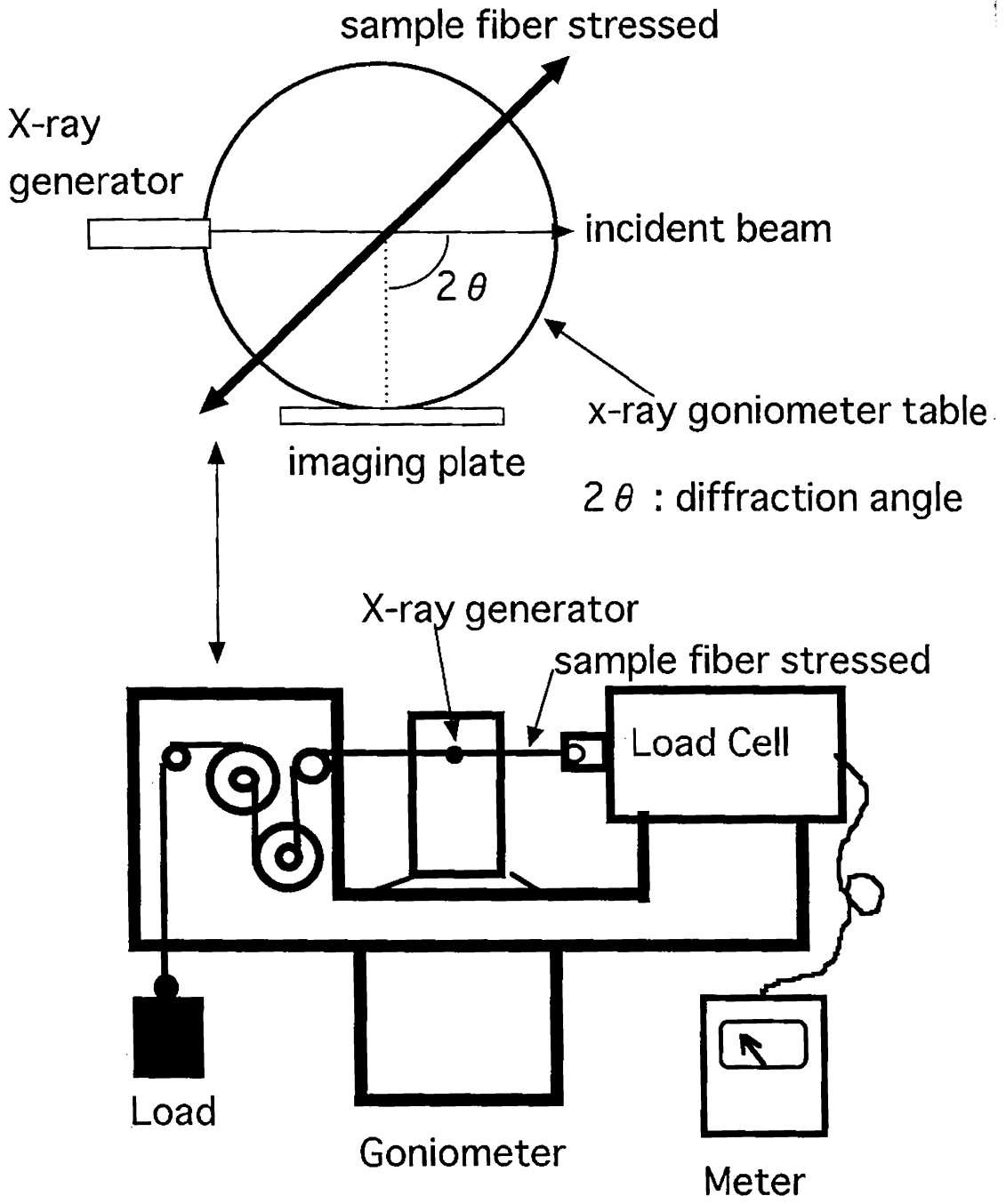

Figure 4-1. Block diagram of in-house stress apparatus and a setting on the wide-angle X-ray goniometer.

4. 3. Results and Discussion

4. 3. 1. Crystalline Modulus

Examples of meridional profiles (HM+) are presented in Figure 4-2. It is seen that the position of the peak top moves toward lower angle and that the breadth of the diffraction profile becomes wider as the applied stress is increased. By analyzing the Bragg spacings of the meridional reflection (the peak top position) as a function of applied stress, the tensile deformation of the polymer chain was calculated by the following equation[81] and the result for the HM+ fiber is plotted in Figure 4-3.

$$\varepsilon_c = -\cot\theta\,\Delta(2\theta)/2 \qquad (4\text{-}2)$$

where 2θ is the diffraction angle of the m-th meridional layer lines and $\Delta(2\theta)$ the difference of the diffraction angle between with and without stress. As shown in the figure, both the diffraction planes ((005) and (00 10)) give the common apparent crystal modulus (E_c^{app}) value. The measurement was carried out for the three types of fibers. Measured apparent crystalline modulus for the HM+ fiber was estimated as 460±20 GPa from the slope of the straight line in the figure, which was almost the same as that of HM (460 GPa), but was different from that of AS (430 GPa) (Table 4-1). Literature values of the crystalline modulus[33,34] and theoretical modulus[32] also give the values of the same range (460 – 480 GPa). It is interesting to notice that the apparent crystalline modulus of PBO does not depend on fiber modulus largely in the HM and HM+ fibers. The value obtained for the HM and HM+ fibers may be a limit and support 460 GPa as the real crystalline modulus. To understand why the AS fiber shows smaller apparent crystalline modulus, the effect of various structural parameters such as real crystallite size, crystalline ordering parameter, shear modulus etc. will be investigated in the following section and in the next chapter.

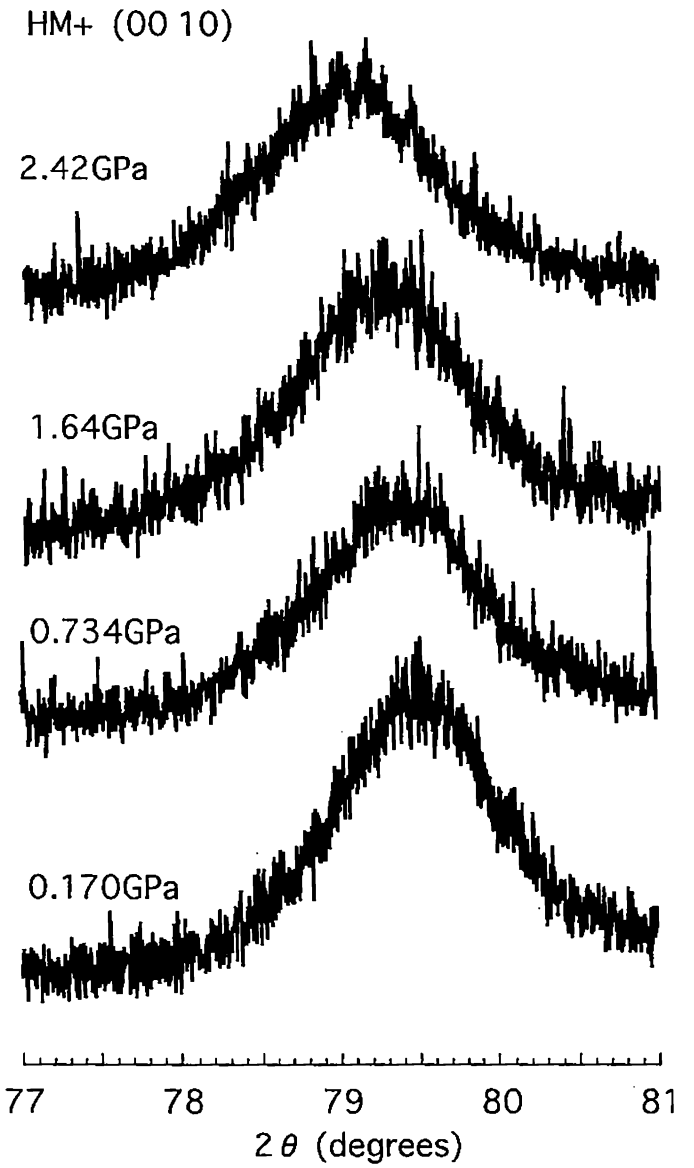

Figure 4-2. Stress dependence of meridional X-ray diffraction profiles.

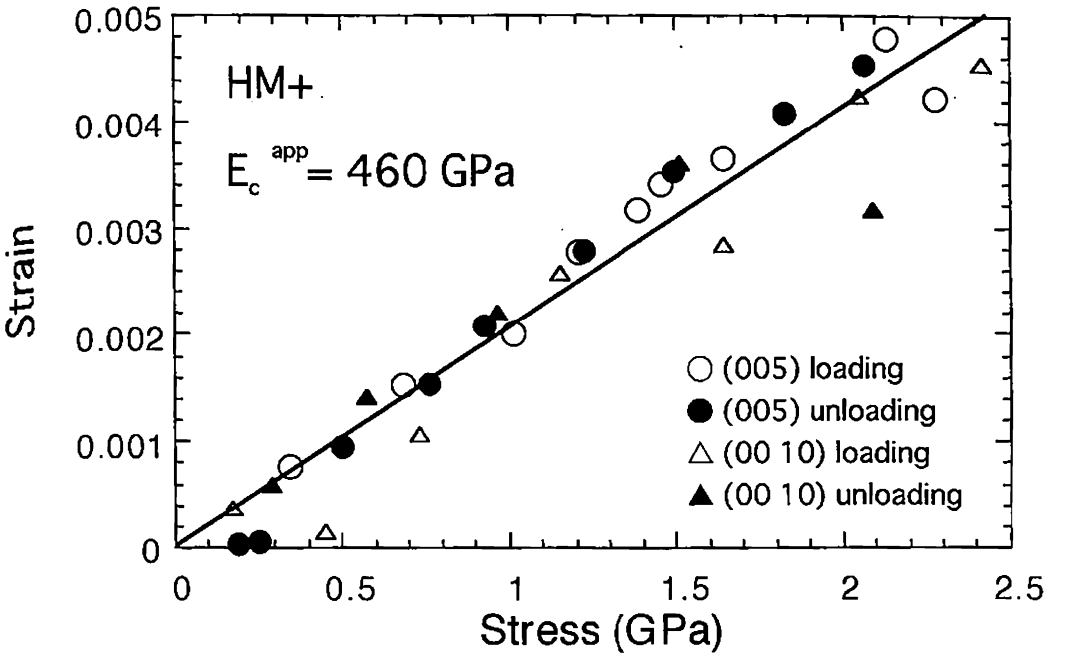

Figure 4-3. Molecular stretch calculated from a change of the Bragg spacing against applied stress.

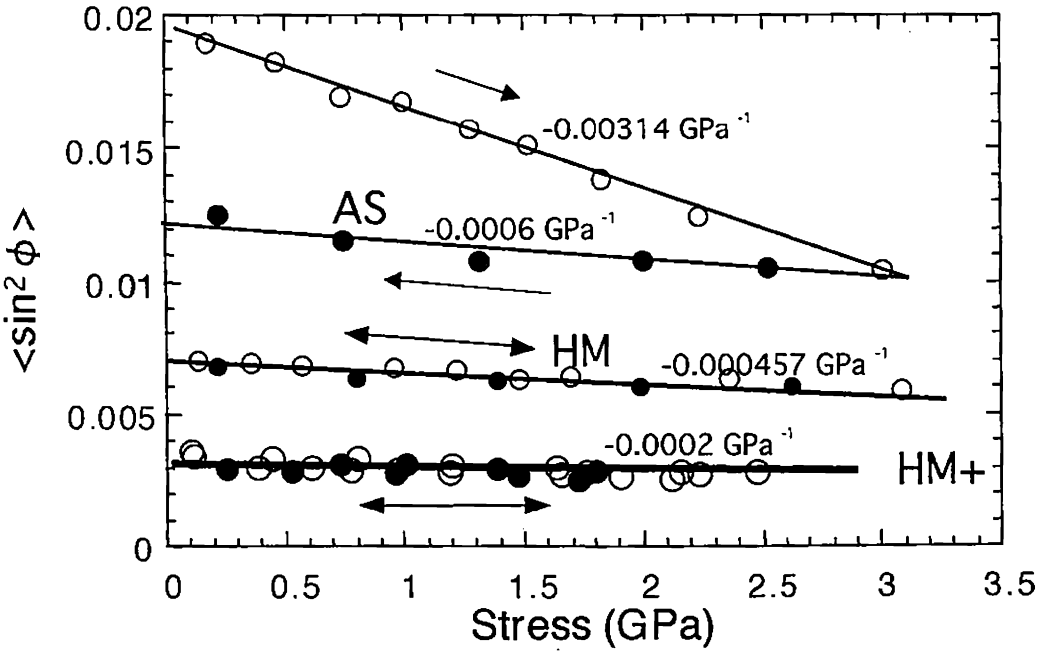

Figure 4-4. The molecular orientation $<sin^2 \phi>$ is plotted against stress. The values of the slope for the lines are attached beside the lines.

Table 4-1. Measured apparent crystalline modulus for the three PBO fibers.

		AS	HM	HM+
E_c^{app}	GPa	430	460	460
G	GPa	5	16	16

4. 3. 2. A Change of Molecular Orientation with Stress

As reported by Northolt et al.,[59] stress-induced molecular orientation change results in the fiber strain along the fiber direction. To understand the feature of high modulus of the HM+ fiber, the orientation of the PBO molecule in the fiber was measured as a function of stress. The distribution of X-ray diffraction intensity along the azimuthal direction for the (200) spot was measured. The result is presented in Figure 4-4. It is seen that the HM+ fiber shows the smallest slope against stress when compared with those of the AS and HM fibers in the figure.

We can calculate the strain due to the molecular orientation change under stress with using the following equation:[59]

$$\varepsilon_r = \langle \cos\phi \rangle / \langle \cos\phi_0 \rangle - 1 \qquad (4\text{-}3)$$

where ϕ is the orientation angle at specified stress and ϕ_0 at zero stress. In Northolt's theory,[59,82] the total fiber strain can be expressed as a sum of strains due to molecular stretch (ε_c) and orientation change (ε_r) as follows:

$$\begin{aligned} \varepsilon &= \varepsilon_c + \varepsilon_r \\ &= \sigma / E_c^{true} + 0.5\langle \sin^2\phi_0 \rangle [1 - exp(-\sigma/G)] \end{aligned} \qquad (4\text{-}4)$$

where E_c^{true} is the crystalline modulus of the PBO fiber, σ is the applied stress and G is the shear modulus due to change of molecular orientation in the fiber under deformation (rotation of the crystallites to the fiber axis). The strain due to change of molecular orientation can be calculated as a function of stress by using equation (4-3) from the $\langle \sin^2\phi \rangle$ data in Figure 4-4. If we compare equation (4-3) and the second

term in equation (4-4), shear modulus due to molecular orientation change (G) can be estimated with a curve-fitting method. Estimated strain calculated from X-ray orientation data is plotted against applied stress and is compared with a theoretical curve in Figure 4-5. The G values for all the three PBO fibers are determined and tabulated in Table 4-1 so that the data points are fitted well. The strain due to molecular orientation is almost the same (AS) as or less (HM and HM+) than that of the stretched PBO molecule in the crystal.

It is interesting to see that the AS fiber shows a smaller G value than those of the HM and HM+ fibers. The value becomes larger in the unloading process of the AS fiber from 1.8% to zero strain than that in the loading process, indicating an occurrence of irreversible structural change (hysteresis). The strain due to molecular orientation decreases as the fiber modulus increases in the order AS, HM and HM+ fibers. This reason may come from the difference of initial molecular orientation of the fiber. More highly oriented fiber (HM and HM+) shows less molecular orientation change when extra-applied stress is given because there seems to remain less room for structural change in the fiber having higher molecular orientation under deformation. This fiber modulus dependence on G may suggest a possibility that the data points should follow the tendency curve that has a convex curvature near perfect orientation and converges into inverse of the crystalline modulus in the Northolt plot (Figure 2-3). This argument on the modification of Northolt's equation should be reexamined in the future. It is also noted that the HM and HM+ fibers give the same shear modulus value (16 GPa), showing that the strength of acting interaction forces between molecules in the PBO fibers might be same in the molecular orientation change. We can understand that these G values of the PBO fibers are higher than those of PPTA fibers (0.5 – 2.0 GPa).[54,59] The reason may be explained as follows. Firstly, PBO molecules in the fibers are highly extended than the PPTA fibers and secondly there is

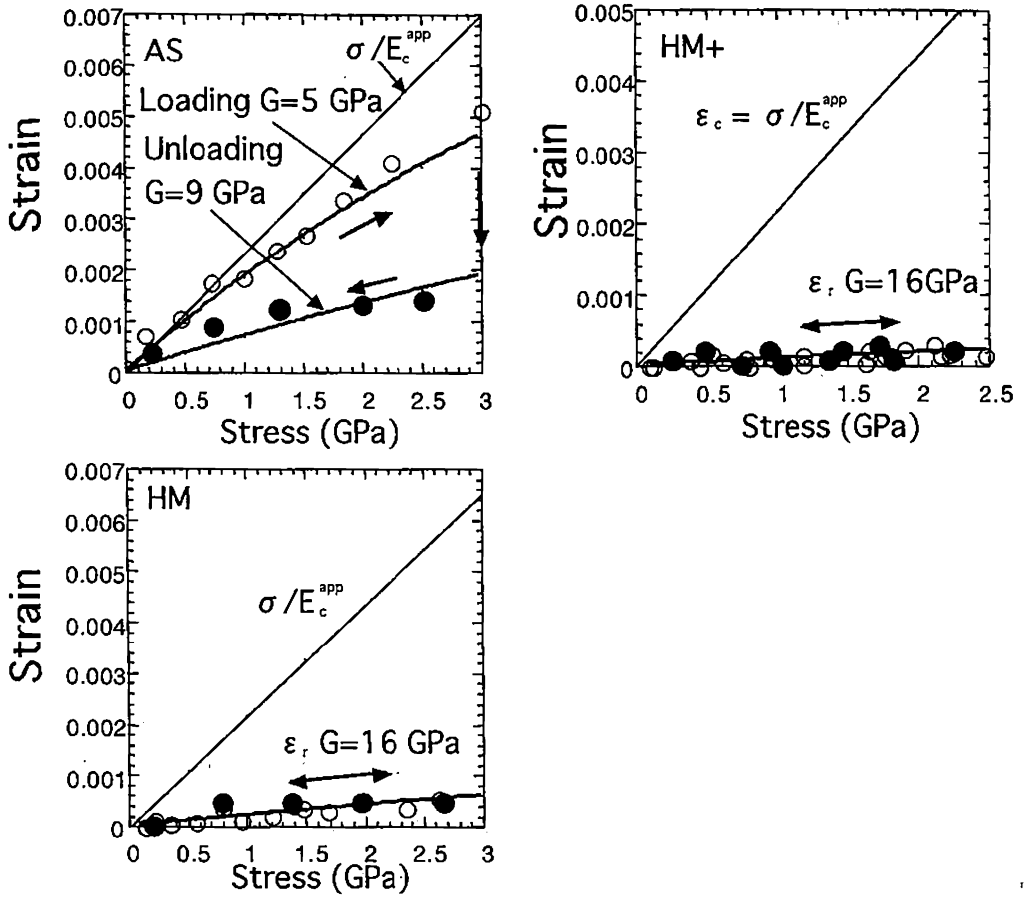

Figure 4-5. Comparison between observed and calculated strains due to molecular orientation change with applied stress. ○ : loading, ● : unloading.

the pleated-sheet structure[1] in the PPTA fiber and therefore rotation of the crystallite may easily occurs in PPTA fiber under deformation process.

The total strain due to molecular stretch and change of molecular orientation is calculated by equation (4-4) together with obtained parameters (E_c^{app}, G, and $<sin^2 \phi_0>$). The result is compared with the experimental fiber strain (by tensile test without twist) in Figure 4-6. The calculated curves do not trace the real strain for all the three fibers. This means that only the effects of molecular stretch (crystalline modulus) and molecular orientation cannot explain the real strain of the fiber. However, the difference between the theoretical and experimental curves becomes less in the order of fiber modulus. To explain this difference, another structural factors such as density fluctuation along the fiber axis should be taken into consideration.

4. 4. Conclusions

In this chapter, a change in molecular orientation and the broadening of meridional diffraction profiles of the PBO fibers under deformation are discussed. The total strain due to molecular stretch and change of molecular orientation is calculated under Northolt's theory but fails to explain quantitatively the actually measured fiber strain. But it is also noted that the difference between prediction and actual measurement becomes less for the sample with increasing fiber modulus. There still remains the source of strain acting along the fiber axis during deformation. As confirmed in this chapter, the meridional layer lines of X-ray diffraction not only move towards lower diffraction angle under stress but also become wider in the profile. It can be related to the induced stress distribution which may be detectable as lattice distortion.

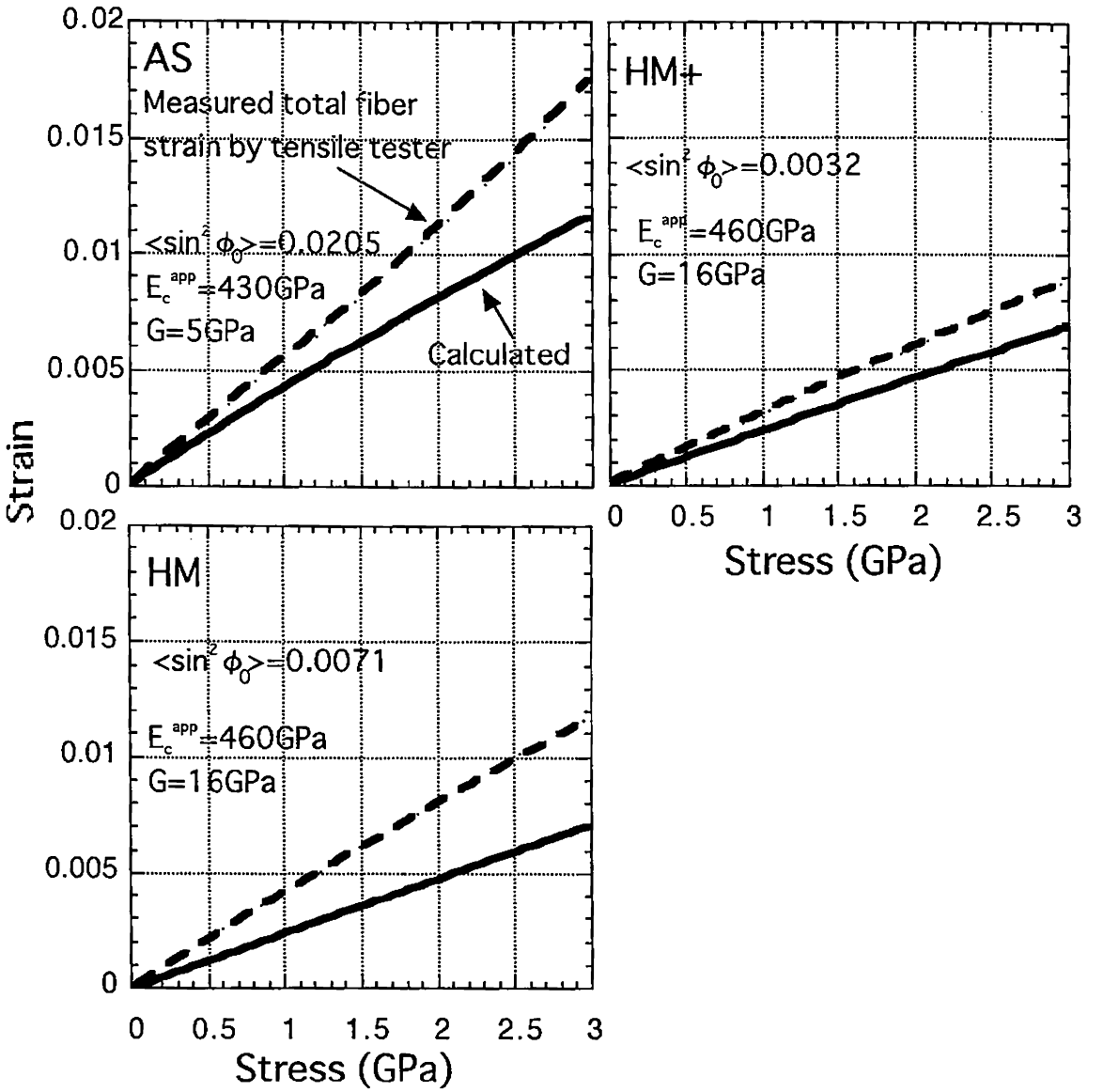

Figure 4-6. Comparison between measured and calculated total strains. Solid line : calculation based on Northolt's theory. Broken line : measured by tensile tester.

Chapter 5

Application of Hosemann's Paracrystal Theory and Induced Lattice Stress Distribution

5. 1. Introduction

As described in the previous chapter, it is understood that only the concept of molecular orientation is not enough to explain the gap between crystalline modulus and actual fiber modulus achieved so far. There remain some additional factors to induce strain along the fiber axis during deformation different from the molecular orientation. Moonen et al.,[83,84] and Wong et al.[85,86] reported that a gel-spun UHMW-PE fiber has bimodal stress distribution in the fiber under deformation as revealed by using WAXS and Raman methods. In this chapter, induced lattice stress distribution is estimated by measuring the X-ray meridional diffraction profiles of the PBO fibers under deformation and analyzed by Hosemann's theory.

5. 2. Experimental

In order to apply Hosemann's theory,[87,88] the X-ray equipment was used which was developed as the tensile apparatus in the previous chapter. The stress apparatus was set on a WAXS goniometer. Obtained peak profiles were corrected for the initial beam source broadening and the doublet of the CuK_α lines. The broadening of initial X-ray source beam was evaluated by directly measuring the profile of the attenuated direct beam around the zero diffraction angle, the diffraction profiles from LiF powder (d = 0.2325nm, 0.2013nm) and the profiles from SiO_2 powder (d = 0.3343nm). The thus obtained profiles showed almost the same value in half-height width (0.53 $\pm$ 0.03 $^\circ$). A deconvolution method was applied to the measured diffraction profiles for

correcting the direct beam broadening. To make correction for the doublet of incident X-ray beam, the α_1 and α_2 lines were assumed to be composed of the same shape with the intensity ratio of 2:1. A corrected diffraction profile was selected to fit the measured peak profiles well on the basis of the above assumption.

5. 3. Results and Discussion

5. 3. 1. Measurement of the Peak Profile

Measured peak profiles of the (005) and (00 10) diffraction spots are shown in Figure 5-1. The fibers are stressed in the range from near 0 up to 3.0 GPa and then were allowed to relax towards 0 GPa. Our main concern is to measure the shape of peak profiles, and therefore a change of absolute peak diffraction angle was not estimated. All the obtained profiles are aligned in the figure to meet the peak top positions at the center of the diffraction profile.

It is seen that the (005) peak does not appear to broaden when stress is applied while the (00 10) profile becomes wider definitely. Only the case for the HM fiber is shown in the figure but the same tendency is observed in the HM+ and AS fibers. To indicate this quantitatively, the data points are approximated with a linear combination of Gaussian and Lorentzian functions and the values of the half-height width (FWHM, full width at the half height maximum) are indicated beside the profiles in the figure. No peak splitting under stress as reported for the UHMW-PE fibers by Kip et al was observed.[83,84] We also see that the FWHM values of the (00 10) diffraction for the three PBO fibers increased with increasing stress while that of the (005) peaks is almost independent of applied stress. It is interesting to notice that the peak profile broadening of the PBO fibers shows the diffraction index dependence, suggesting that the broadening is due to the second kind of disorder. This point is discussed on the basis of Hosemann's paracrystal theory[87,88] in a later section.

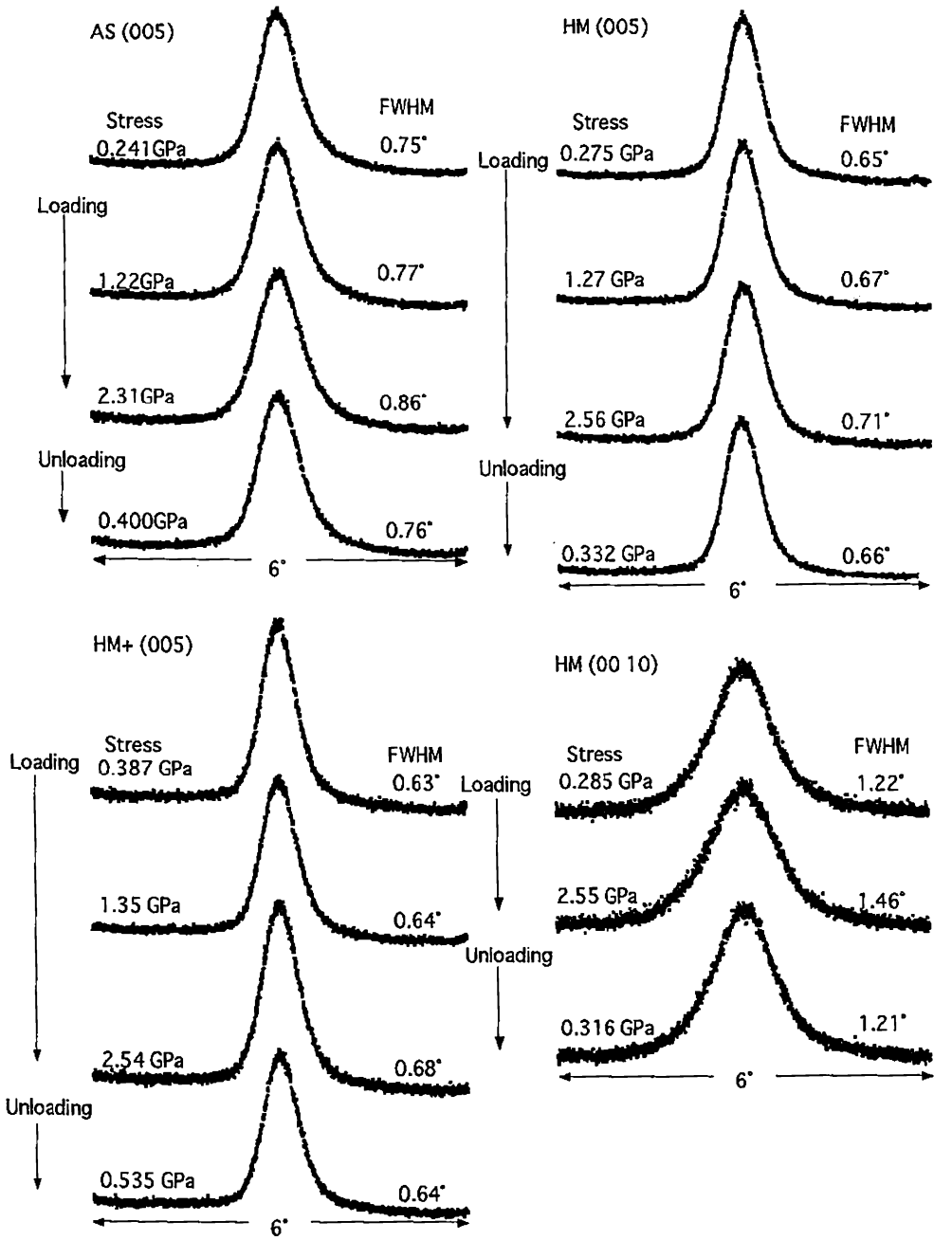

Figure 5-1. Stress dependence of X-ray meridional profiles.

5. 3. 2. Induced Disorder in the Crystal Structure under Deformation

Stress dependencies of FWHM for the (003), (005), (009) and (00 10) diffraction spots are shown in Figure 5-2. The increasing rate of FWHM against stress becomes steeper as the index number of the meridional diffraction is increased. The changes in FWHM follow the linear line over the stress range from 0 to 3 GPa and do not show the abrupt increase as confirmed in the UHMW-PE fiber.[83,84,89] These features are seen in common for all the three types of PBO fibers. In the loading and unloading processes the hysteresis can be detected for the (009) and (00 10) diffraction spots of AS but is not seen for the (003) and (005) diffraction spots. As a result, FWHM of the (009) and (00 10) diffraction spots broadens at zero stress after relaxation of stress. Reversible response of FWHM against stress can be seen in HM and HM+ under loading and unloading processes.

Hosemann[87,88] proposed a theory to analyze such dependence. This theory takes not only the crystallite size but also the degree of ordering in the crystalline lattice into consideration to explain the observed broadening of X-ray diffraction profile. All the meridional profiles obtained in this study were approximated well with the Lorentzian function. In that case the integral breadth $\delta\beta$ (the total area of the profile divided by the maximum peak height) is explained as follows :[87,88]

$$\delta\beta = \delta\beta_0 + (\pi g m)^2 / c \qquad (5\text{-}1)$$

where $\delta\beta_0$ is the integral breadth determined only by real crystallite size along the fiber axis, g the ordering parameter of the crystalline lattice, m the index of meridional diffraction and c the Bragg spacing of the (001) plane. Hosemann's plot at 0 GPa and 2.5 GPa of stress is made in Figure 5-3 from the estimated values of FWHM in Figure 5-2. The real crystallite size D is evaluated from the equation $D = 1/\delta\beta_0$ and is

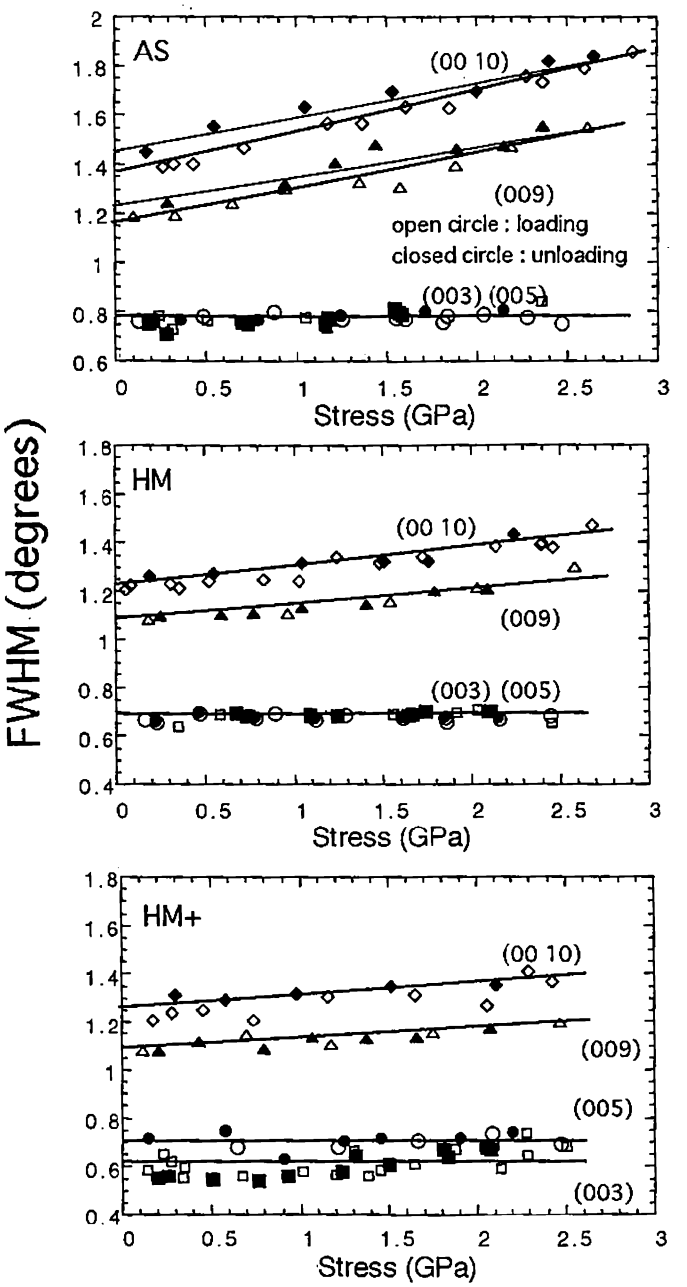

Figure 5-2. Stress dependence of half-height width of PBO meridional X-ray diffraction profiles.
○,□,△,◇; the loading process : ●,■,▲,◆; the unloading process.

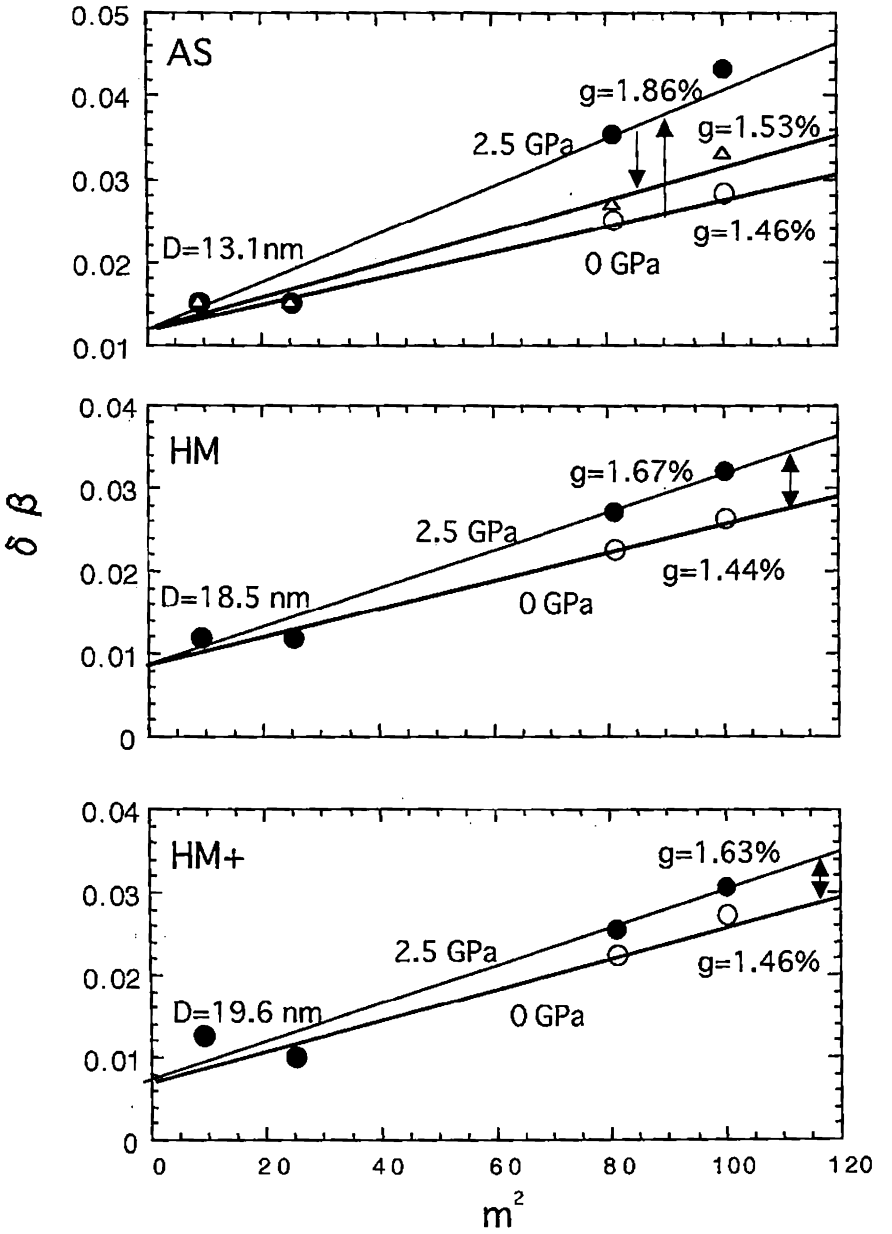

Figure 5-3. Stress dependence of Hosemann's plot for the three PBO fibers. ○ : 0.0 GPa, ● : 2.5 GPa, △ : 0.0 GPa after relaxation.

indicated in the same figures together with g. The ordering parameter g depends strongly on the applied stress while the crystallite size stays constant. It is also interesting that the AS fiber shows relatively large hysteresis with stress; the thick line in the figure after relaxation of stress deviates from the initial line at zero stress. As already mentioned in Chapter 4, molecular orientation is also changed with stress. The HM and HM+ fibers do not show such permanent structural change with stress; the response is confirmed to be reversible.

In Figure 5-4 the estimated g values are plotted against the fiber modulus. There is no fiber modulus dependence of g at zero stress while the g values under stress (2.5 GPa) are decreased in the order of AS (180 GPa) > HM (280 GPa) > HM+ (360 GPa). As reported in Chapters 2 and 3, the morphology of the PBO fiber is different among AS, HM and HM+. It is noted that HM+ especially takes more homogeneous structure along the fiber axis as revealed by SAXS (Chapter 2). This fact may give less change of the crystalline ordering under deformation in the HM+ fiber because the disordered part may give an origin of the strain.

Application of tensile stress induces the change in the stress distribution due to distortion of the periodicity in the crystalline lattice in the fiber, which was detected as X-ray diffraction broadening and an increase of g against external stress. The orderliness of the PBO crystal structure in the fiber changes with the applied external stress even though the crystallite size does not change with stress. In the case of UHMW-PE case, splitting of profile was observed in X-ray diffraction and Raman scattering[83-86] when tensile stress was put on the fiber. It can be understood that there are taut tie molecules in the UHMW-PE fiber structure. In such the region, chains are overstressed under deformation and would result in a bimodal distribution in X-ray and Raman profiles. The present analysis based on Hosemann's theory suggests that the PBO fiber does not have the above-mentioned structure for the UHMW-PE fiber due to

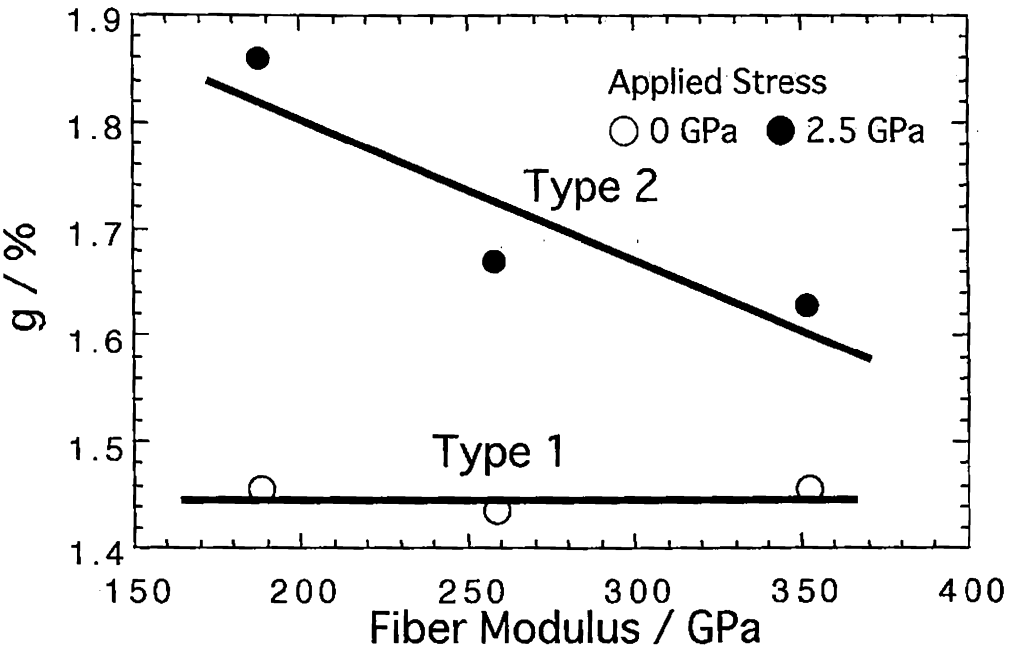

Figure 5-4. Fiber modulus dependence of the ordering parameter *g*. The explanation for Type 1 and 2 is given in Section 5. 3. 3.

the coexistence of the crystalline and amorphous parts. One of candidates to explain such phenomena of PBO fiber is that an occurrence of reversible micro-molecular slippage between neighboring molecules in the crystal lattice which may affect the behavior of the diffraction profile. As reported by Jones et al.[60] this slippage may be due to such irregularities that disconnect stress transfer at molecular ends along the fiber axis and also give the stress distribution along the molecule. To quantify this stress distribution induced in the molecules, Raman scattering measurement of stressed fiber will be made in Chapters 6 and 7.

5. 3. 3. The Relationship between Structural Parameters and Fiber Modulus

Estimated parameters are re-examined in Figures 5-4 and 5-5 to elucidate their fiber modulus dependence. It is found that they are categorized into two groups if they are plotted against fiber modulus.

(Type 1) Saturation type; E_c^{app} (apparent crystal modulus), D (real crystal size along the fiber axis), g (crystalline disorder at zero stress) and G (shear modulus due to change of molecular orientation) show saturation in the region above 280 GPa.
(Type 2) Fiber modulus dependent type; $\langle \sin^2 \phi_0 \rangle$ and g (at 2.5 GPa) change with fiber moduls.

It is interesting that structural parameters (D and g at zero stress) shows convergence against fiber modulus but g at 2.5 GPa depends on fiber modulus. This may imply that the factors that determine fiber modulus are not the size and disorder of crystallite composing a fiber but the molecular orientation and the degree of stress-induced crystalline lattice distortion of the fiber. The shear modulus (G) also shows a saturation, indicating that strength of the forces that act to forbid the molecular

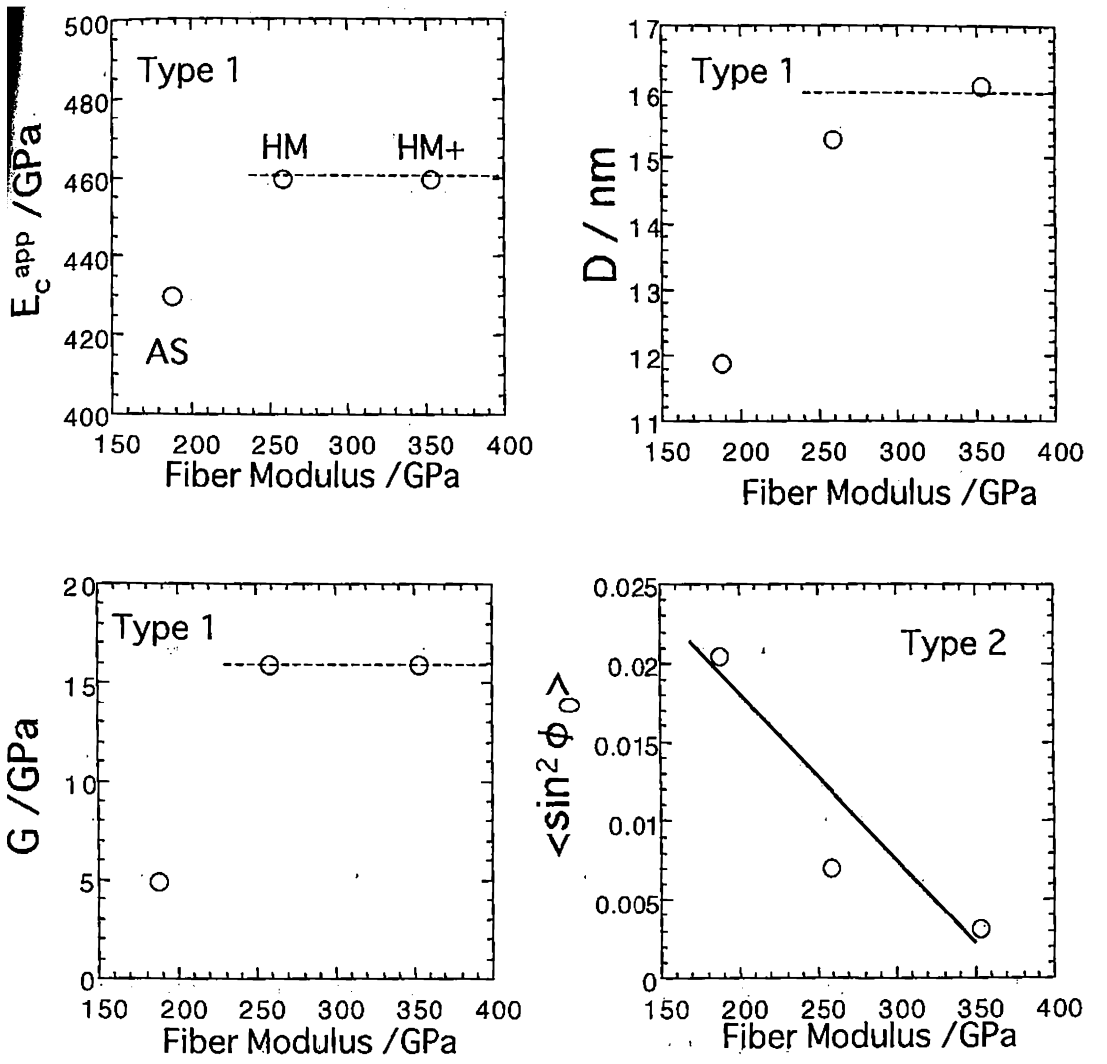

Figure 5-5. The correlation between estimated various structural parameters and fiber modulus.

orientation change with applied stress can not be improved in the higher fiber modulus region (of the HM+ fiber). As already discussed in this study, only the molecular orientation factor cannot explain a gap between the real PBO fibers and the crystalline modulus. To explain all these observations we may propose a hypothesis that concentration of defects that causes modulus reduction decreases in the HM+ fiber. The defects may induce not only disconnection of stress transfer but also stress distribution in the fiber structure. If the concentration of defects is low, induced stress distribution may be suppressed. The absence of the four-point SAXS pattern in the HM+ (Chapter 2) fiber and the behavior of g under stress support the hypothesis. The structural homogeneity along the fiber axis and g at 2.5 GPa of stress are correlated well, suggesting that the stress-induced crystalline lattice distortion is caused by the degree of inhomogeneity or the concentration of defects in the fiber.

5. 3. 4. Remaining Unsolved Problems to Realize PBO Fiber Modulus Close to the Limiting Value

In this section the importance of concentration of structural defects[46,60] in the PBO fiber is explained. The analysis of strain based on Northolt's theory which assumes that the stress is due to combination of molecular orientation and molecular stretch failed to explain the actually-observed stress-strain curves of the PBO fibers. As revealed in the previous chapter, an absence of the SAXS four-point pattern was found, which should be taken into account to understand the effects of the concentration of structural defects and inhomogeneity (density fluctuation) along the fiber axis. The interaction between the neighboring chains in the PBO fiber is due to the van der Waals forces and electrostatic forces.[53,60] The interaction strength is so weak that micro slippage between them occurs easily. To explain this concentration effect of defects, Jones et al.[60] performed a computer-simulation in order to clarify the

relationship between concentration of chain ends and modulus reduction and found that the fiber modulus decreases with the chain end concentration. There exists stress distribution in the molecules under tension. Termonia et al. proposed a lattice model to predict the effects of bond breakage of molecules on the stress-strain curves of the UHMW-PE[90,91] and PPTA[92,93] fibers. It is still an unsettled problem to what extent the chain ends contribute to the modulus reduction and the stress distribution due to the existence of the chain end. Other type of defect structures such as amorphous region and conformational irregularity[53,94] may also play a role.

5. 4. Conclusions

The peak profiles of the meridional X-ray diffraction obtained from PBO fibers under stress are investigated to see the mechanism of deformation in the fiber structure. It is found that peak broadening occurred during the deformation process. To analyze the peak broadening, Hosemann's theory was adopted. The analysis says that ordering in the crystal structure is distorted under deformation, which is proved by the increase of the *g* values, while crystallite size estimated from the slope in the Hosemann's plot at 0 GPa and 2.5 GPa of stresses is not changed. It is understood that the applied stress induces the distortion of the PBO crystalline lattice that will be related to an increase of stress distribution along the molecule in the fiber axis.

Chapter 6

Estimation of Stress Distribution in PBO Fibers by Raman Spectroscopy

6. 1. Introduction

In the previous chapter, strain-induced lattice stress distribution of the crystallite was discussed. This stress distribution is a reflection of structural incompleteness in the fiber structure. The source to give this stress distribution may be related to structural defects such as chain ends, molecular misorientation and inhomogeneity along the fiber axis. It is known that Raman spectroscopy can evaluate such stress distribution by measuring the band shift caused by tensile stress.[76,77] As will be explained theoretically in the next chapter,[27,28,95-97] the shift rate (the frequency shift of the Raman band by 1 GPa tensile stress) is expressed as a function of geometry of the molecule composing the fiber and force constants of the bonds connecting the atoms in the molecule. The rate value also varies with fiber structural inhomogeneity.[85,86]

In this chapter, the peak shift and broadening of one particular Raman band at 1619 cm^{-1} are estimated as functions of tensile stress and strain because the 1619 cm^{-1} band is assigned to the skeletal vibration of the phenylene ring[95-97] and is sensitive to stress distribution induced along the fiber axis.[98] General assignment of the observed Raman bands of PBO to molecular vibrational modes is performed in the next chapter. Fiber modulus dependence of these data is also discussed.

6. 2. Materials and Experimental Methods

6. 2. 1. Materials and Single Fiber Mechanical Testing

The three PBO sample fibers investigated were AS, HM and HM+. The fiber

modulus and strength were measured using an Instron 1121 universal testing machine. A monofilament (single filament) was mounted across a cardboard window using a quick-setting epoxy resin and stored at least two days to allow the resin to set completely prior to testing. Gauge (sample) lengths of 20, 50 and 100 mm were employed for at least 20 specimens by using a cross-head speed of 1%/min. All the tests were carried out at 23 ±2 °C and a relative humidity of 50 ± 5%. The load-time data were stored in a digital form by using a Macintosh computer and Workbench 3.1 software. The data were converted into stress-strain curves; the stress was determined from the load and fiber cross-sectional area and the strain was calculated from the gauge length and cross-head displacement.

The fibers were examined on a Philips 505M scanning electron microscope (SEM) operated at 10kV with its magnification calibration using a calibration specimen with 2160 lines/mm. The fiber was coated with a thin layer of gold to avoid charge build up during SEM operation and the diameter was obtained from the average of at least 25 measurements.

6. 2. 2. Raman Spectroscopy

Raman scattering measurements were conducted under both tensile and compressive loading by using a Renishaw System 1000 Raman microprobe with a newly-developed 25 mW IR laser. The 780 nm IR laser allows well-defined fluorescence-free spectra to be obtained from fibers such as PBO. A ×50 objective lens of an Olympus BH-2 optical microscope was used both to focus the laser beam on the specimen surface (spot size of ~2 μm in diameter) and to collect the 180° back-scattered radiation. A highly-sensitive Renishaw Charge-Coupled Device (CCD) camera was used to collect the Raman spectra. The degree of peak shift and peak broadening under stress of the 1619 cm^{-1} PBO Raman band, corresponding to the

vibration of the backbone *p*-phenylene ring,[95-97] were determined. The digital data were processed on a computer with the Renishaw analysis software in which a Lorentzian curve-fitting procedure was used to determine the peak position and width.

In order to apply tensile strain to a single fiber and obtain a Raman spectrum simultaneously, a single filament of 50 mm gauge length was fixed using cyanoacrylate adhesive between aluminium foil tabs. One end of the tab was connected to a miniature load cell to measure load and the other to a micrometer to apply and monitor the fiber displacement, with a precision of ± 0.005 mm. For compressive deformation, a four-point bending method was adopted.[99] An individual single filament was placed on the surface of a PMMA plate and covered with a thin layer of PMMA/chloroform solution that was allowed to dry. The strain was monitored by using a resistance strain gauge (Measurements Group, Inc.) carefully fixed near the filament on the plate using cyanoacrylate adhesive.

6. 3. Results and Discussion

6. 3. 1. Mechanical Testing

Typical stress-strain curves are shown in Figure 6-1 for the three PBO fibers (single filaments). It appears that there is some strain hardening for all three fibers. The strain-stress curve of AS fiber increases in slope until ~ 0.7% strain, the slope then becomes lower at intermediate strain, and finally increases again in the high stress region. The stress-strain curve for the HM fiber decreases in slope after the stress-strain curve reaches its steepest point around 1.0 % strain. For the HM+ fiber, which has the highest modulus value of the three fibers, the curve increases in slope from 0% until 1.2% strain, after which the slope becomes less. This shape is clearly different from that of the HM fiber and interesting because even the heat-treated HM+ fiber seems to show some limited strain hardening. It is also noteworthy that the stress-strain

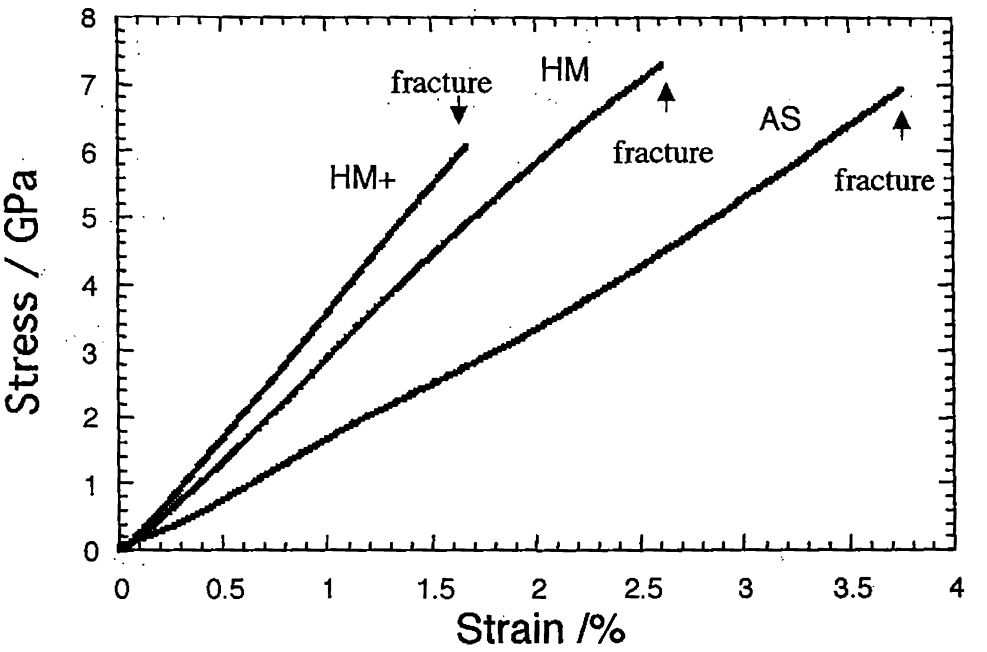

Figure 6-1. Stress-strain curves for the three PBO single filaments. The sample length is 50 mm.

curve for the AS fiber includes an intermediate region in which strain dependence of Young's modulus decreases before the hardening starts. Both of these phenomena cannot be explained solely by an improvement in molecular orientation as shown in Chapters 2, 4 and must therefore be related to the existence of density fluctuation along the fiber axis.

In order to estimate the modulus in the absence of end effects and intrinsic fiber strength, the mechanical properties of the fibers were measured using three different gauge lengths. The modulus was determined by extrapolating to infinite gauge length as shown in Figure 6-2(a) and the strength by extrapolating to zero gauge length as shown in Figure 6-2(b). It is thought that effect of defects (such as chain ends, dislocation, poor molecular orientation etc.) in the fiber is excluded at zero gauge length and the end effect of the sample fiber at infinite gauge length.[99,100] It can be seen that the modulus increases in the order AS < HM < HM+ (c.f. Figure 6-1) and that the HM+ fiber has a slightly lower strength than AS and HM fibers. The mechanical properties of the fibers (single filaments) are summarized in Table 6-1.

6. 3. 2. Raman Band Peak Shifts

Raman spectra measured at zero strain for the three fibers with no background subtraction are shown in Figure 6-3. It can be seen that there is an increase in background fluorescence scattering in the order of AS < HM < HM+, but in spite of this effect the spectra all show well-defined peaks which are far better-defined than those reported previously with a He-Ne laser (632.8 nm).[45] It is thought that this is due to change of laser wavelength to an IR laser (780 nm) that leads to much lower levels of fluorescence than those obtained by a He-Ne laser.

Figure 6-4 shows the effect of deformation upon the 1619 cm^{-1} band for the three different types of PBO fiber subjected to tensile and compressive strains. The band

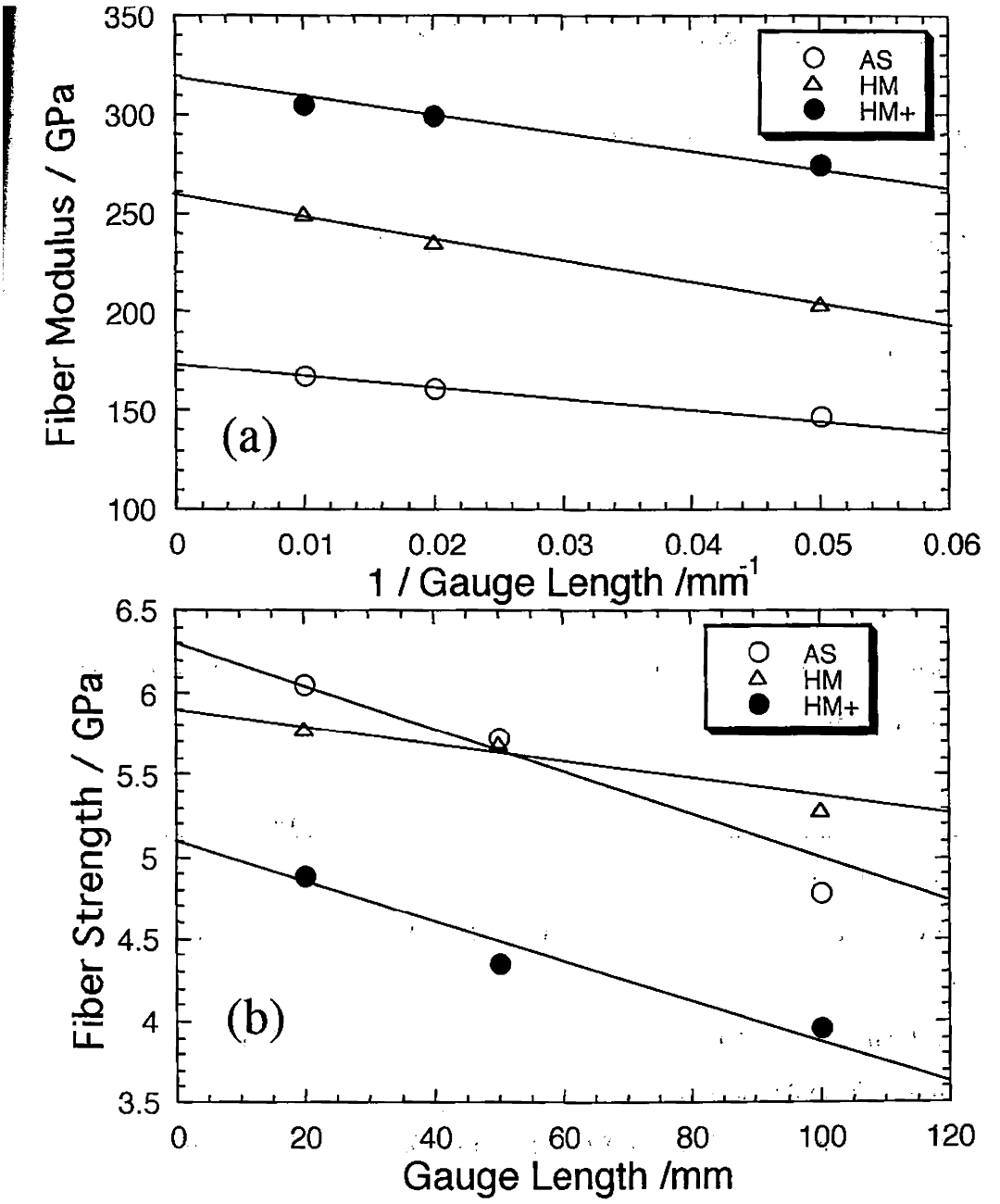

Figure 6-2. Gauge length dependence of the mechanical properties.

Table 6-1. Mechanical properties measured by tensile test for single fiber.

	Strength	Modulus
	GPa	GPa
AS	6.30 (0.88)	173 (16.3)
HM	5.90 (0.79)	260 (24.4)
HM+	5.10 (0.76)	320 (29.7)

( ) : standard deviation

Table 6-2. Raman shift and broadening factors measured for the band at 1619 cm^{-1} with single fiber.

		AS	HM	HM+
Strain-induced Raman				
band shift rate	cm^{-1}/%	-4.85 (0.40)	-8.60 (0.26)	-11.52 (1.37)
Stress-induced Raman				
band shift rate	cm^{-1}/GPa	-3.27 (0.30)	-3.75 (0.40)	-4.06 (0.34)
Stress-induced Raman band				
broadening rate	cm^{-1}/GPa	-4.18 (0.50)	-3.42 (0.50)	-2.60 (0.18)

( ) : standard deviation

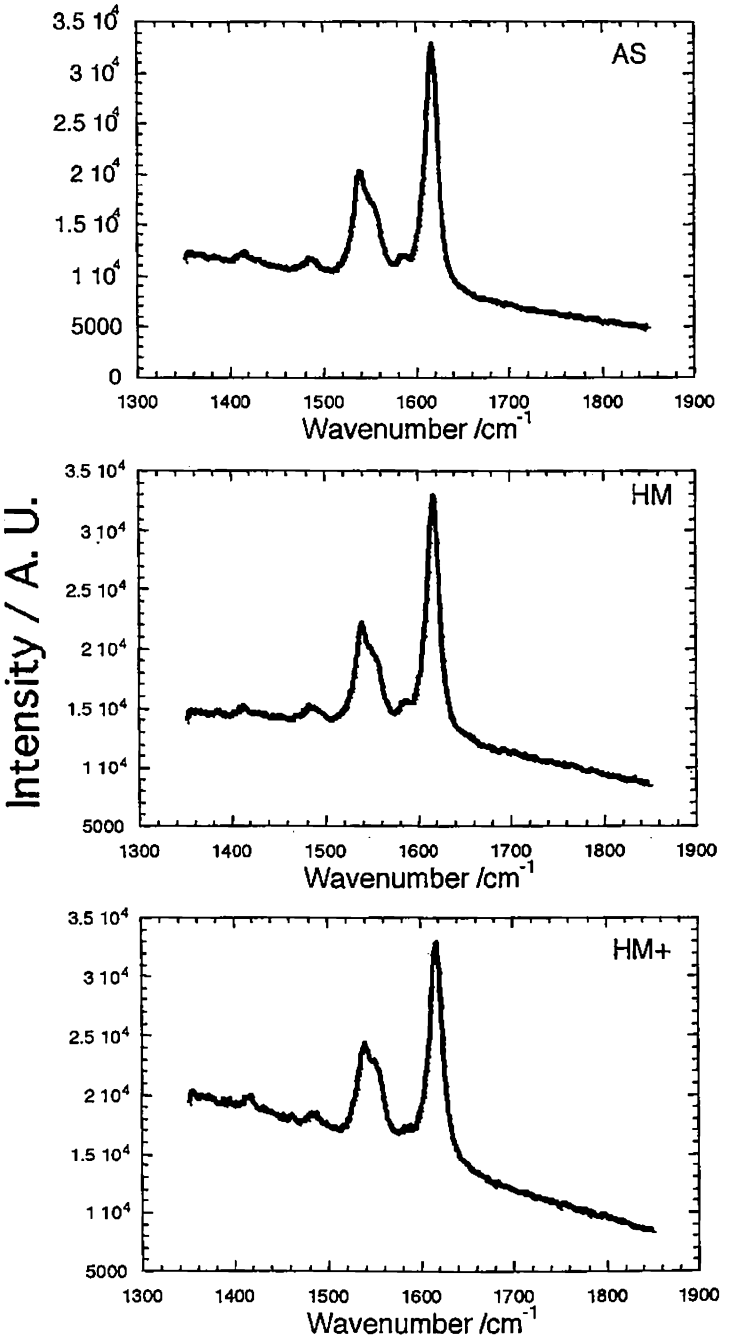

Figure 6-3. Raman spectra for the three PBO fibers with zero stress.

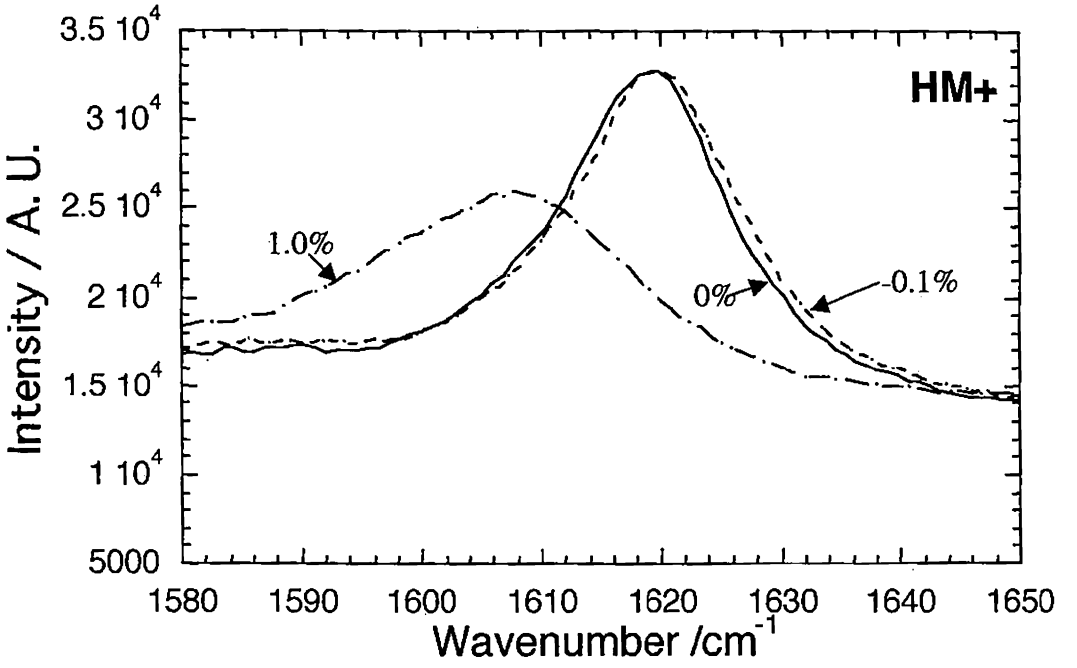

Figure 6-4. The effect of deformation for the HM+ fiber subjected to tensile and compressive stresses. The values in the figure indicate applied strain to the sample fiber.

can be seen to move towards low wavenumber and broaden with increasing tensile deformation but shift in the opposite direction and become narrower by compression. This indicates that molecules in the fibers respond to the external tensile deformation and that there is a distribution of the band shift observed in the fiber structure. The detailed behavior of the peak position and shape were analyzed in detail using a Lorentzian curve-fitting procedure.

Typical strain-induced Raman band peak shifts for the three PBO fibers are shown in Figure 6-5(a). It can be seen that the intercepts at zero strain of all the plots have the same value (1619 cm^{-1}). The data points for the AS fiber follow a linear line in the low strain region but deviate at intermediate strain. For the HM and HM+ fibers the points lie approximately on straight lines. The strain- and stress-induced Raman band shifts were determined from the initial slopes of the curves. It was found that the slopes increased with increasing fiber modulus and the value of strain-induced Raman shift for the HM+ fiber reached -12 cm^{-1}/%, which is the highest value reported for this band in aromatic polymer fibers such as PBO and PPTA.[101] It is known that the strain-induced band shift factor in such fibers is controlled by molecular orientation[82] and so this very large value must reflect the high degree of molecular orientation in the HM+ fiber.

Deformation-induced Raman band shifts were also determined as a function of stress for the PBO fibers as shown in Figure 6-5(b). In the literatures,[101-103] the Raman band corresponding to the vibration of the backbone *p*-phenylene ring is reported to have the same stress-induced shift rate (approximately -4.0 cm^{-1}/GPa) for PBO, PPTA, and PET (poly(ethylene terephthalate)) fibers i.e. irrespective of materials, when the molecules in the fiber are highly oriented. The molecules in all the PBO fibers are so highly extended that we may assume that they are all strained homogeneously and such that the three fibers should have the same values of stress-induced Raman band shift.

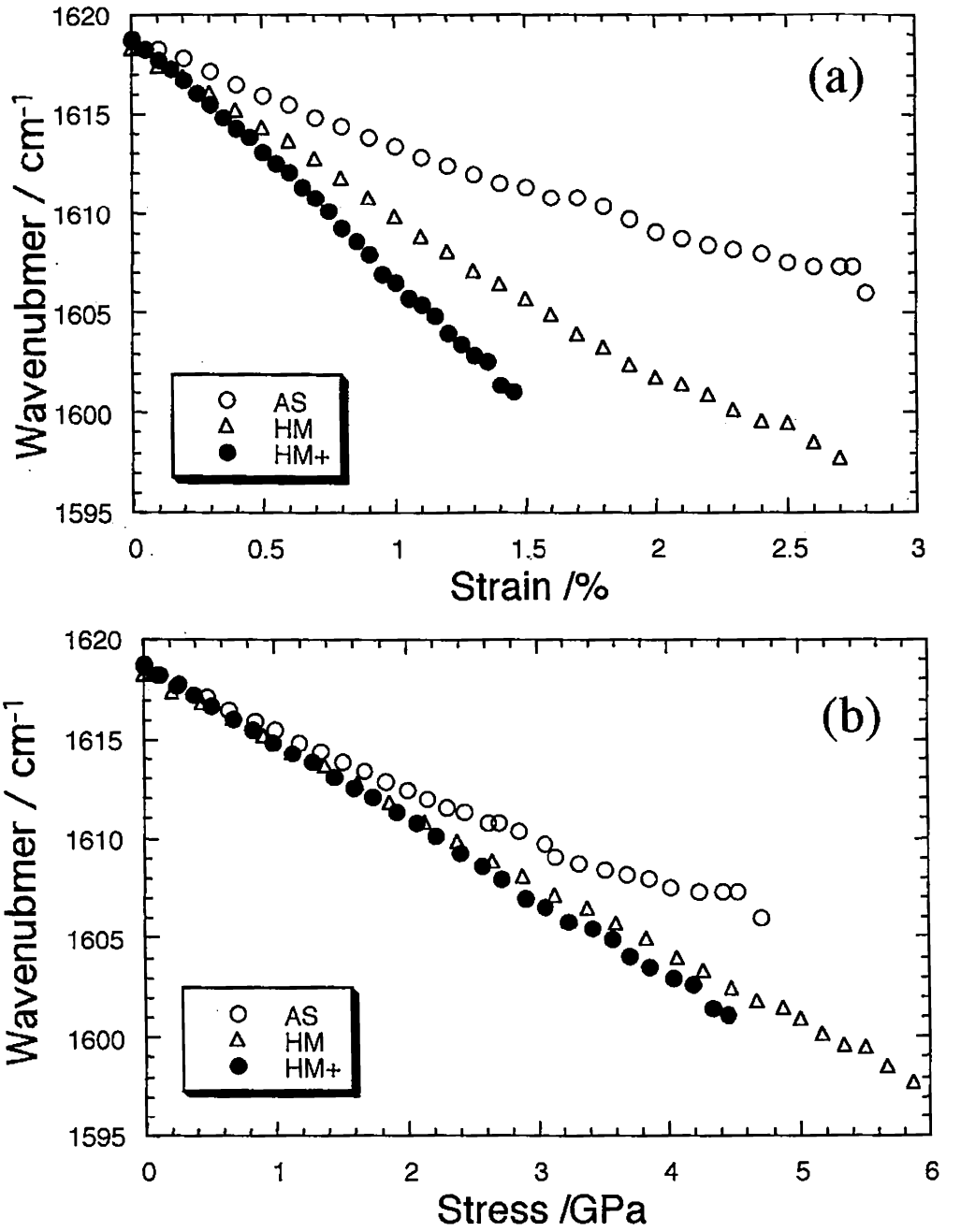

Figure 6-5. Strain and stress dependence of Raman frequency for the three PBO fibers.

Table 6-2 shows that the values obtained for the HM+ fiber follow this rule, but that the AS fiber showed a value significantly lower than –4 cm^{-1}/GPa. The shift factor has fiber modulus dependence. This may be due to the difference of fiber morphology, which will be analyzed with a series-parallel model in the next chapter.

6. 3. 3. Raman Band Broadening

The full width at half-height maximum (FWHM) values of the Raman bands are plotted against strain and stress in Figures 6-6(a) and (b). It can be seen that in each case there is significant peak broadening that is considered to be due to the stress distribution upon the molecules in the fibers.[102] From the slopes of the plots, the Raman band broadening can be estimated and the values are presented in Table 6-2. It is seen that the stress-induced Raman band broadening value for the HM+ fiber is the smallest (2.6 cm^{-1} /GPa) among the three fibers. The strain-induced Raman band broadening value of HM is less than that of HM+, but larger than that of AS fiber. This difference in band broadening behavior is complicated and thought to be due to both the molecular orientation and the presence of structural defects along the fiber axis. It is also noteworthy that the intercept at zero strain for the HM+ fiber (~17.2 cm^{-1}) is slightly higher than those of the AS and HM fibers (~16.0 cm^{-1}) which may indicate a higher level of initial residual stress in the HM+ fiber but the reason is still unresolved.

It is interesting to relate this phenomenon of stress-induced Raman band broadening to an absence of the SAXS four-point pattern (Chapter 2) for the HM+ fiber. This indicates that the HM+ fiber has a more homogeneous structure along the fiber axis than the HM fiber. It is possible that the inhomogeneity in the HM fiber comes from the periodicity of ordered and disordered regions; the disordered regions could include molecular chain ends, dislocations, poorer orientation etc. To achieve the homogeneous structure, the molecules in the HM+ fiber must take a more extended

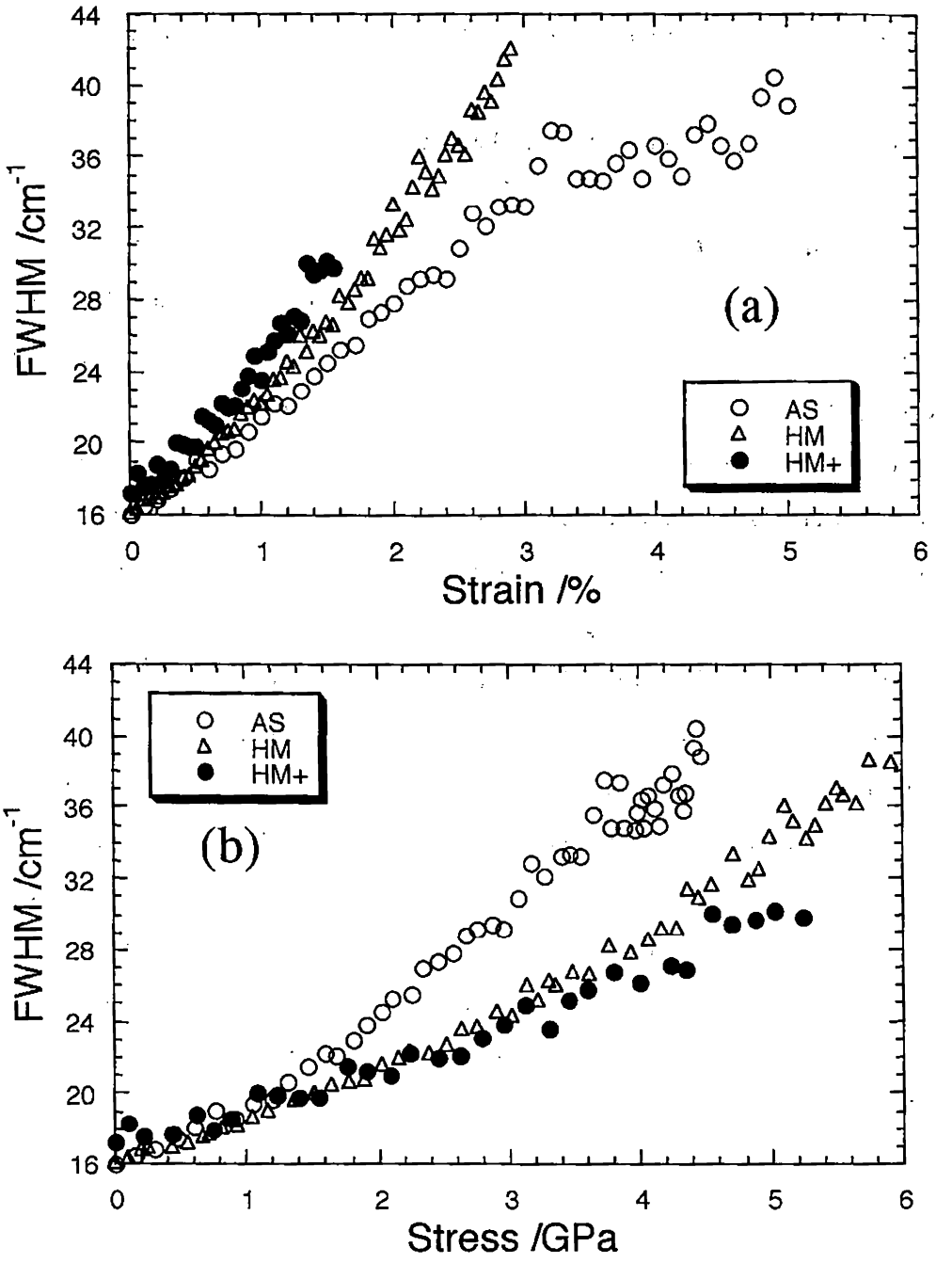

Figure 6-6. Strain and stress dependence of FWHM for the three PBO fibers.

form than in the HM fiber. Such a molecular conformation will necessarily cause both the broader FWHM at zero stress (initial state) and the smaller level of Raman band broadening. In conclusion it is believed that the small value of band broadening for HM+ originates from this homogeneous structure, which is investigated in the next chapter.

6. 3. 4. Compressive Deformation

Figure 6-7 shows the variation of the peak positions and FWHM of the 1619 cm^{-1} Raman bands with both tensile and compressive fiber strain for the three types of PBO fiber. It can be seen that there is an approximately linear relation between band position and fiber strain when fibers are deformed in tension. The behavior in compression, however, is quite different. The band shifts to a higher wavenumber until reaching a maximum value at a critical strain, after which it remains a plateau value. The fiber over the compressive yield point has kink bands. These behaviors are similar for all the three PBO fibers. At the same time, the FWHM increases by tension but becomes narrower when the fiber is compressed until a critical strain value, after which it becomes constant. This critical value of strain is similar to the value for which Raman band position reaches a plateau. The compressive strength of the PBO fibers can be estimated from the critical strain required to reach this plateau and the values are tabulated in Table 6-3. The heat-treated fibers show slightly higher compressive strength values than the AS fiber. These values are significantly less than those obtained for the polypyridobisimidazole (PIPD or M5)[99] fiber and so it appears that the compressive properties of high-modulus polymer fibers are determined by the basic molecular structure of the polymer.

It is interesting to observe that the FWHM narrows by compression, implying that the distribution of local molecular stress in the fibers is reduced. This behavior is

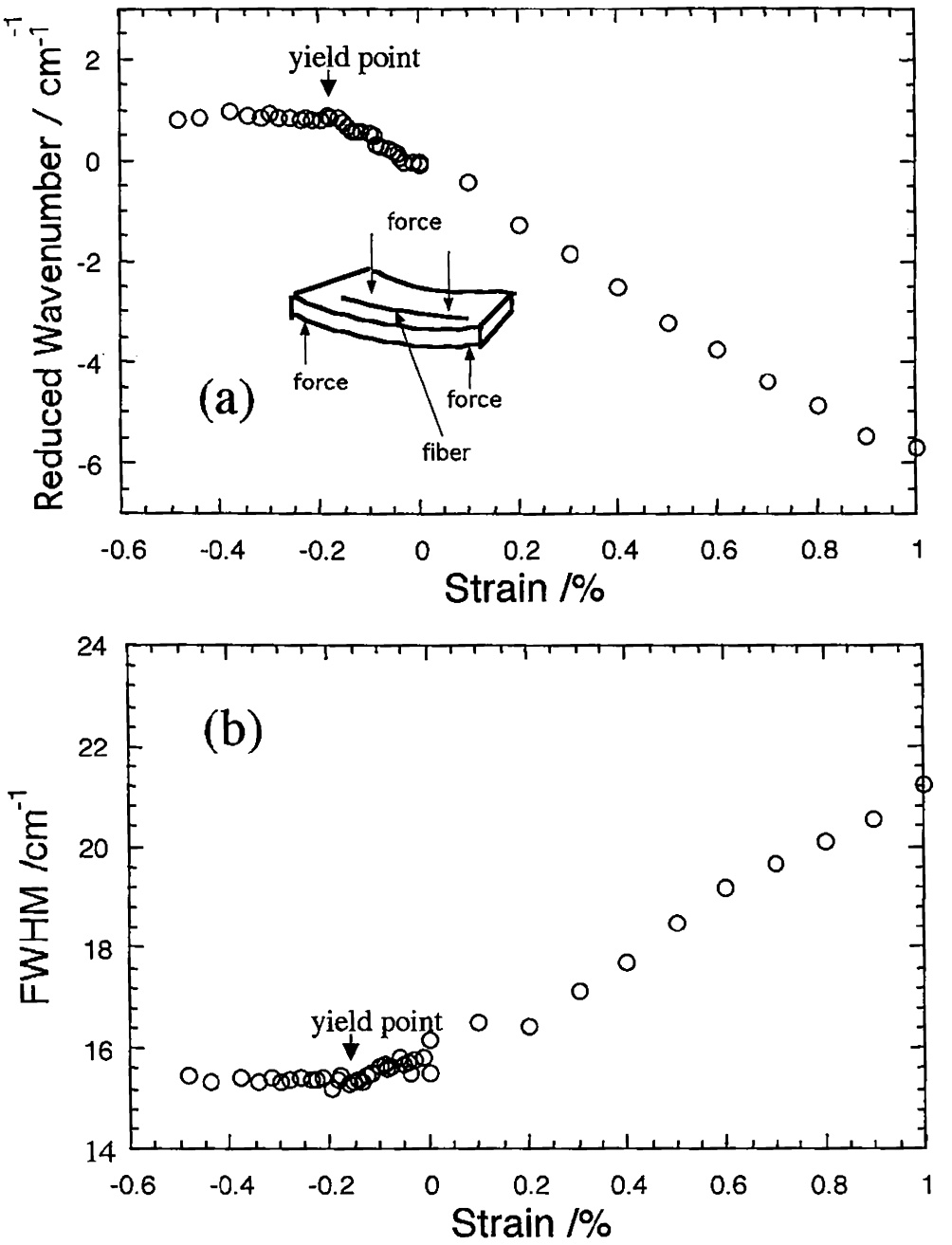

Figure 6-7. Strain dependence of reduced wavenumber and FWHM for the AS fiber.

Table 6-3. Compressive strength for the three PBO fibers

	Compressive Strength (GPa)
AS	0.29
HM	0.36
HM+	0.35

different from that of other fibers such as carbon fibers[104,105] that appear to show broadening in both tension and compression. The PBO molecule is not composed of a perfect three-dimensional crystal structure as in carbon fibers and the molecules are connected by the van der Waals forces and electrostatic forces.[52,53] It may be true that residual strain induced in the coagulation and heat-treatment processes is relaxed during compressive deformation leading to the Raman band narrowing.

6. 3. 5. Comparison with Crystalline Modulus

The relationship between stress-induced band broadening and fiber modulus is presented in Figure 6-8. Measured values of crystalline modulus of up to 460-480 GPa have been found for PBO in literatures[33,34] and in Chapter 4 using X-ray diffraction. Early theoretical calculations of modulus by Wierschke[31] for PBO predicted a modulus value of over 600 GPa whereas a value of 460 GPa has been reported by Tashiro and Kobayashi following a theoretical calculation based on lattice mechanics.[32] In Figure 6-8 the linear line fit to the data points of the PBO fibers extrapolates to 530 ± 50 GPa for zero band broadening. This value is higher than the measured values of PBO crystalline modulus but within the range of values calculated theoretically.

6. 4. Conclusions

A newly developed PBO fiber (HM+) with a Young's modulus higher than 350 GPa has been investigated together with commercial AS and HM fibers using Raman spectroscopy. It is found that rate of strain-induced Raman shift for the HM+ fiber is the highest among the three fibers, consistent with its high-modulus as a result of its high level of molecular orientation. The values of stress-induced Raman band shift for the PBO fibers are around -4.0 cm^{-1}/GPa except for AS (-3.3 cm^{-1}/GPa). Raman band broadening shift is sensitive to fiber modulus and is needed with the observation of

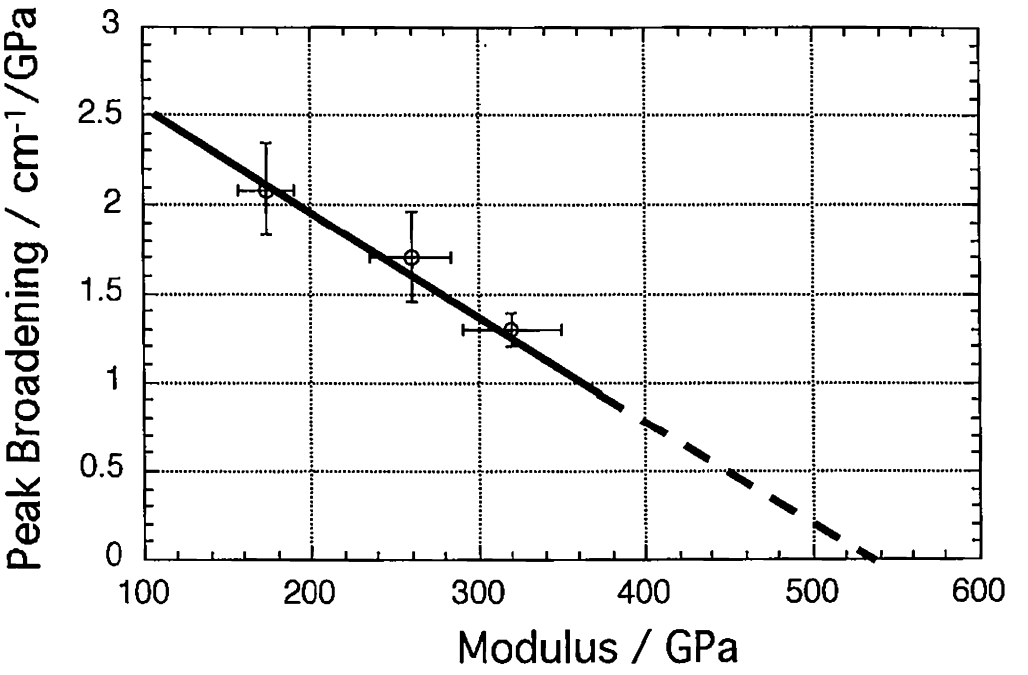

Figure 6-8. Modulus dependence of Raman peak broadening.

extinction of the SAXS four-point pattern in the HM+ fiber. There should be a relation between density fluctuation in the fiber structure and the stress distribution of individual molecules that form the fiber structure. In compression the Raman bands become narrower. This might be due to the relaxation of residual strain in the fibers during processing.

Chapter 7

Stress Distribution in PBO Fibers as Viewed from Vibrational Spectroscopic Measurement under Tension

7. 1. Introduction

In the previous chapter, structural change of PBO fibers subjected to a tensile force has been discussed on the basis of Raman spectroscopic measurement. The stress-induced frequency shift of Raman band at 1619 cm^{-1} was investigated and the shift factor or the frequency shift caused by 1 GPa tensile stress was evaluated. This factor was smaller for the sample with lower fiber modulus. This behavior of PBO is quite contrast (opposite) to that of polyoxymethylene (POM), where the Raman shift factor became smaller for the sample of higher crystallinity.[98] This difference between PBO and POM may reflect the difference in the stress distribution in the bulk samples. Tashiro et al.[98] treated this problem for POM and PE with a mechanical series-parallel model and succeeded to explain the relationship among apparent crystallite modulus, bulk fiber modulus, and Raman shift factor. In order to investigate this stress distribution problem in PBO samples, however, we need to know more details about the behavior of not only the 1619 cm^{-1} Raman band but also the various Raman bands of PBO fibers subjected to the tensile stress.

Before the discussion about the relationship between Raman band shifts and sample morphology, the origin of the band shifts must be clarified from the microscopic point of view. For this purpose we can carry out the lattice dynamical calculation[32] with the anharmonic effect taken into account.[27] Calculation gives the limiting values of the band shift factors and the crystalline modulus. Based on this information, the shift factors of the actual samples may be interpreted in relation with the morphology of

the PBO fibers. This idea will be applied to the case of PBO fibers.

In this chapter Raman scattering measurement was carried out over the frequency range of 200 - 4000 cm^{-1} by means of a Fourier-transform Raman spectrometer. The spectrometer gives well-defined spectra of PBO fibers without background scattering. Normal modes calculation[95-97] under a quasi-harmonic approximation[27,28] is also conducted to predict the vibrational frequencies as well as the Raman shift factors. A crystallite modulus was calculated by the lattice dynamics theory,[32] which will be compared with the measured one. Finally, the relation between the Raman shift factor and the bulk modulus of a sample will be treated on the basis of a modified mechanical model proposed by Tashiro et al.[98]

7. 2. Experimental

The three types of PBO samples (AS, HM and HM+) were adopted. The Raman spectra were measured by using a BioRad FTS Fourier-transform Raman spectrometer equipped with a Ge detector. The laser beam of 1.064 μm wavelength was irradiated as an excitation beam and the 180° scattering was collected. A bundle of PBO fibers was set to a home-made tensile apparatus with a load cell to detect the applied stress. This apparatus was set in the spectrometer. The position and full width at half-height maximum (FWHM) of Raman bands were evaluated by carrying out the deconvolution of the overlapped band profiles.

7. 3. Results

The Raman spectrum measured for a PBO fiber under free tension is shown in Figure 7-1. Vibrational frequency and relative intensity of the observed Raman bands are summarized in Table 7-1. Compared with the general polymers, the Raman intensity from PBO fiber was appreciably high due to the resonance Raman effect

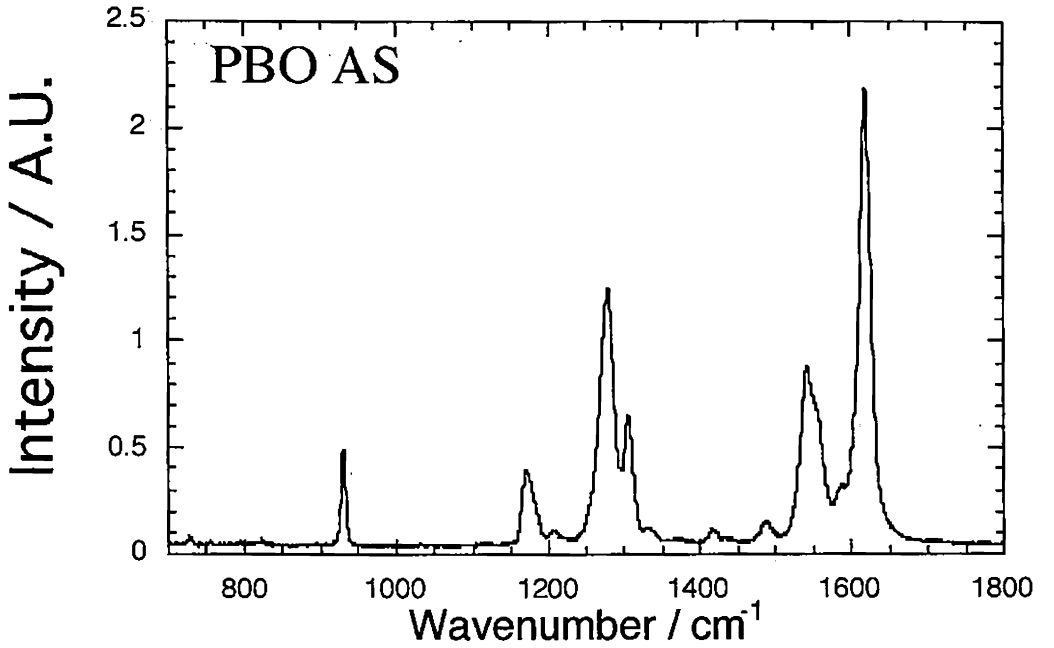

Figure 7-1. Raman spectrum of PBO AS fiber.

Table 7-1. Comparison between measured and calculated normal mode vibration frequencies.

Measured[a] IR // cm^{-1}	IR ⊥ cm^{-1}		Raman cm^{-1}		Calculated cm^{-1}	Symetry Species	Approximate Description of normal mode[b]
	3099	m			3052	A1	C-H stretch
					3052	B2	C-H stretch
	3068	m			3051	A1	C-H stretch
					3050	B2	C-H stretch
	3036	m			3050	A1	C-H stretch
					3050	B2	C-H stretch
					1738	A1	PB ring stretch
1630		s			1657	B2	P ring stretch
	1619	s	1619	vs	1609	A1	PB ring stretch + C-C' stretch
1581		s	1586	vw	1649	B2	P ring stretch + C-C' stretch
	1557	s	1557	s	1575	A1	P ring stretch + B ring def + C-C' stretch
	1540	sh	1542	s	1553	A1	P ring stretch + B ring def
	1497	s			1518	A1	C-O + C-C' + O ring def
1495		s					
	1488	sh	1488	vw	1502	A1	P ring stretch + C-C' stretch
1460		w			1481	B2	O ring stretch + P ring def
	1430	w			1490	A1	BO ring stretch
	1414	s	1418	vw	1412	B2	PO ring stretch
	1392	w			1452	A1	O ring def
1390		w					
1366		s			1368	B2	C-N
	1330	w	1336	vw	1338	A1	BO ring stretch
1310		w	1307	m	1306	A1	P ring def
	1308	w					
1292		w					
1285		w					
	1275	w	1279	s	1284	A1	P ring def
1237		vw			1203	B2	BO ring def
	1209	w	1208	vw			
	1176	vvw	1176	m	1126	A1	PBO ring def
			1168	m	1116	A1	PBO ring def
1156		sh					
1147		m			1176	B2	PB ring def
1118		m					
	1116	m			1091	A1	BO ring def
1110		m			1157	B2	PB ring def
1059		m			1065	B2	BO ring def
	1055	m					
	1041	sh					
1010		w			1018	B2	B ring def
					980	B1	B C-H o.p.
					976	B1	P C-H o.p.
					974	B1	B C-H o.p.
	927	m	930	s	974	B1	P C-H o.p.
					959	A2	P C-H o.p.
					956	A2	P C-H o.p.
919		m			1003	B2	C-O
871		m			888	B2	B ring def
	852	m			858	A1	O ring def
	832	vvw					
830		vvw			839	B2	BO ring def
	820	w	822	vvw	784	A1	BO ring def
	806	sh	795	vw	741	A1	O ring def
758		vw	755	vvw	810	B2	BO ring def

			728	vvw	718	B2	O ring def
708		w					
	706	w			614	B2	P ring def
					549	B2	B ring def
					542	A2	C-C' torsional mortion
					524	B1	C-C' torsional mortion
			487	vw	492	A1	B ring def
					466	A1	BO ring def
					429	B2	C-C' anti-symmetric stretch
					408	A2	P tortional mortion
					381	B2	C-C' bend
					372	A2	P tortional mortion
					345	A2	B tortional mortion
					312	A2	B tortional mortion
					296	B1	O tortional mortion
					258	B1	BO tortional mortion
					249	B1	C-C' tortional mortion
					211	A2	C-C' tortional mortion + P o.p.
					208	B1	C-C' tortional mortion
			215	vvw	197	A1	C-C' bend
					165	B1	B tortional mortion
					152	A2	C-C' tortional mortion
					124	B1	B tortional mortion
					112	B2	C-C' bend
					61	A2	O tortional mortion
					52	B1	B tortional mortion

a. v : very, s : strong, m : medium, w : weak, sh : shoulder
b. P : phenylene, B : benzene, O : oxazole, def : deformation, o.p. : out-of-plane

coming from the electronically conjugated structure of the skeletal chain. The tensile stress dependence of the Raman spectra is shown in Figure 7-2. It is seen that most of the Raman bands shift towards lower frequency side by the application of tensile stress. The width of these bands became wider.

The vibrational frequencies of the observed Raman bands are plotted against the applied stress as shown in Figure 7-3. The frequencies are found to move towards lower frequency side almost linearly with an increase of applied stress. The frequency shift is reversible; the bands were recovered to the original positions with decreasing tensile stress for the HM and HM+ fibers. Also we find in the figure that the rate of frequency shift differs from band to band. The rate is determined by the balance between harmonic and unharmonic force constants,[27,28] and the vibrational mode of this bands, as will be discussed in a later section. As seen in Figure 7-4 some bands of the AS fiber give a hysteresis between the processes of increasing and decreasing stresses as already confirmed in the previous chapter. This hysteresis was observed also in the previously reported X-ray diffraction data (Figure 4-4).

The band shift was found to depend on the preparation history of the samples or the fiber modulus as shown in Figure 7-5. It is interesting to note that the rate of Raman shift decreases for most of Raman bands as the fiber modulus is higher. Similar phenomenon was observed for POM[98] but the tendency was opposite to this PBO case. This dependence is related to the morphology of the fiber sample, especially to the orderliness of the fiber structure; the morphological change affects the stress distribution that results in a change in the behavior of stress-induced Raman shift, as will be discussed in a later section. In order to develop this discussion we need to establish at first the shift factors intrinsic of the observed crystalline state. For this purpose, we carried out the extrapolation of the observed shift factors to the point of the crystalline modulus, as indicated in Figure 7-5. These extrapolated values of shift

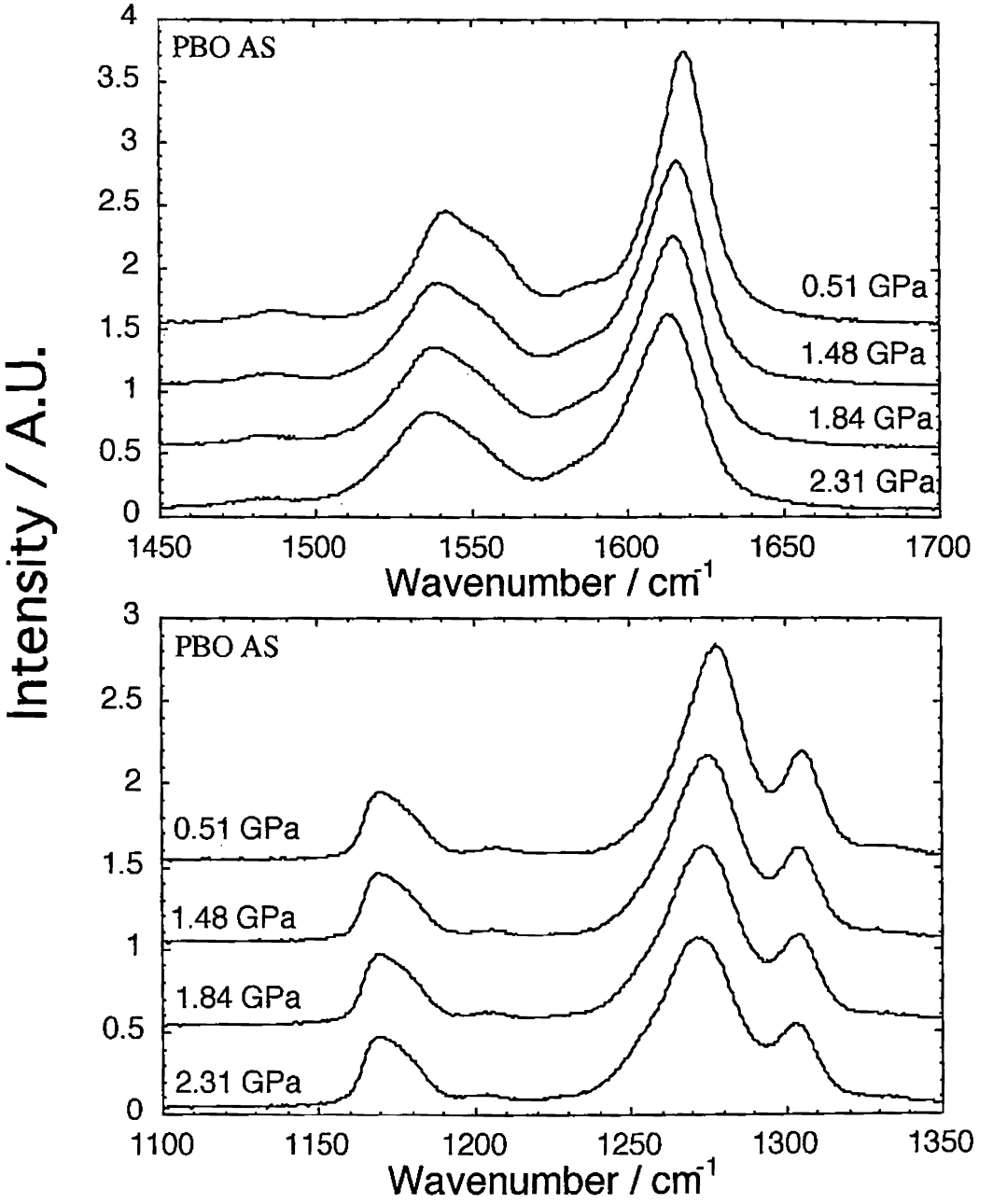

Figure 7-2. Stress dependence of Raman spectra of PBO AS.

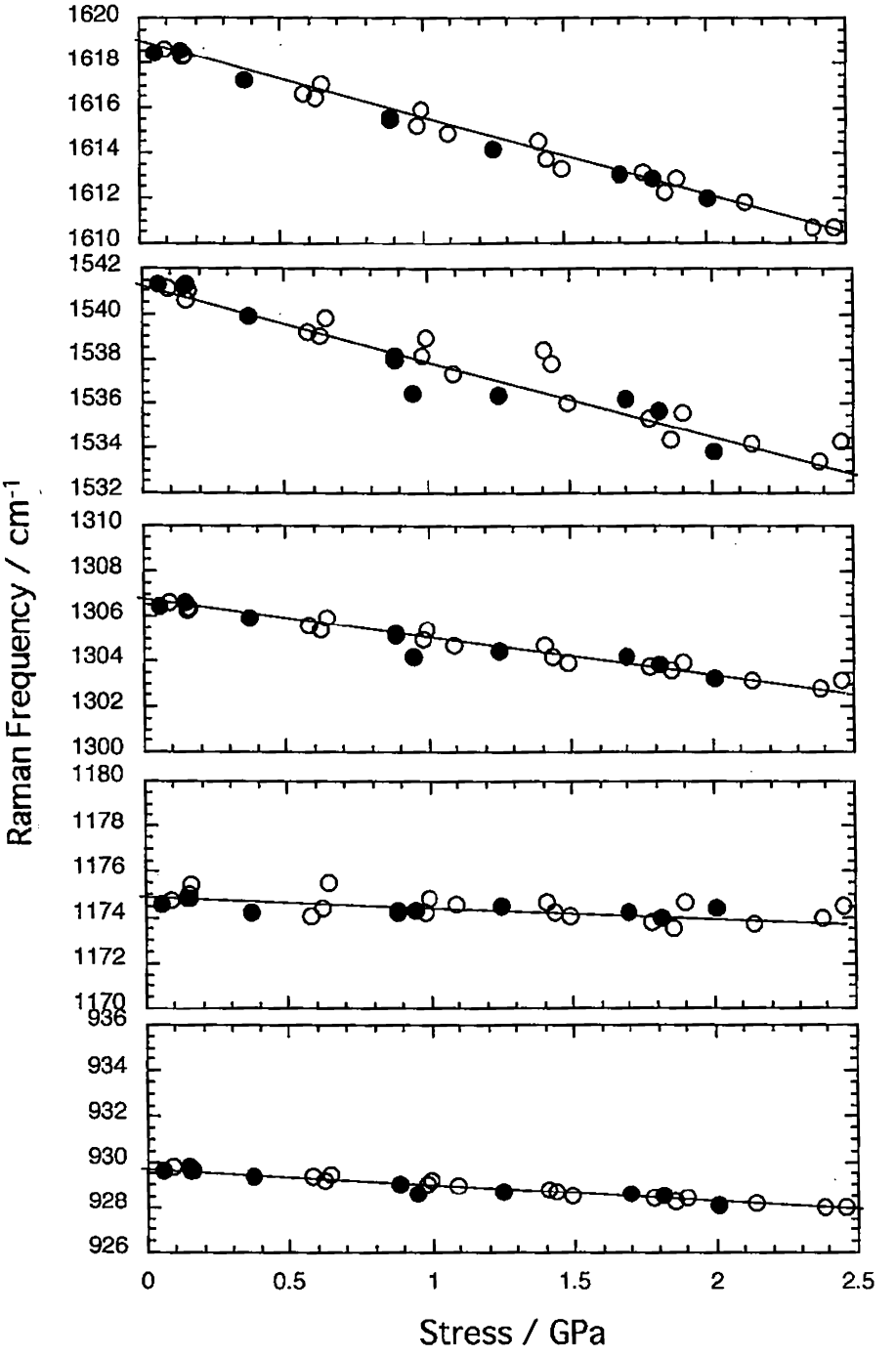

Figure 7-3. Stress dependence of Raman frequency for HM+. ○:loading process, ●:unloading process.

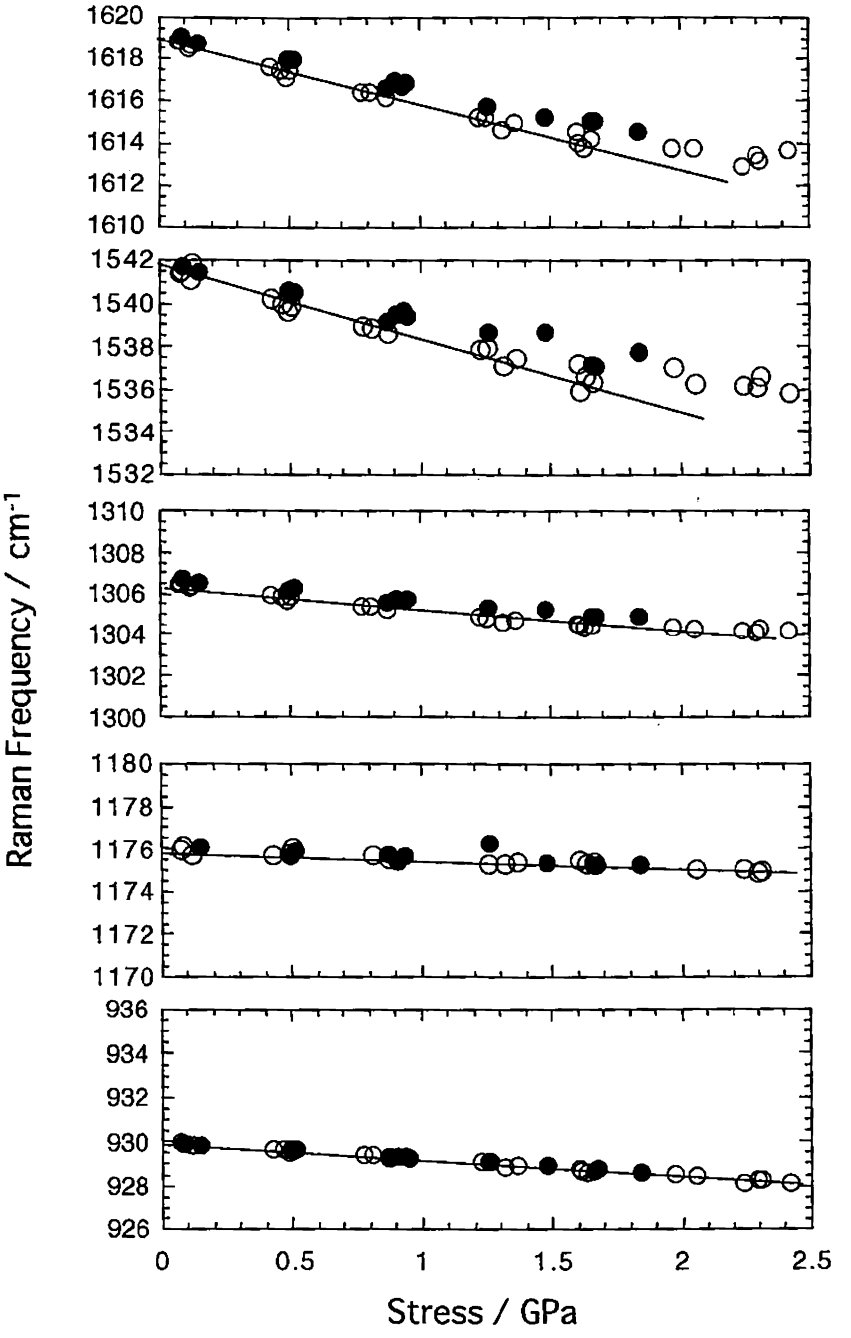

Figure 7-4. Stress dependence of Raman frequency for AS. ○:loading process, ●:unloading process.

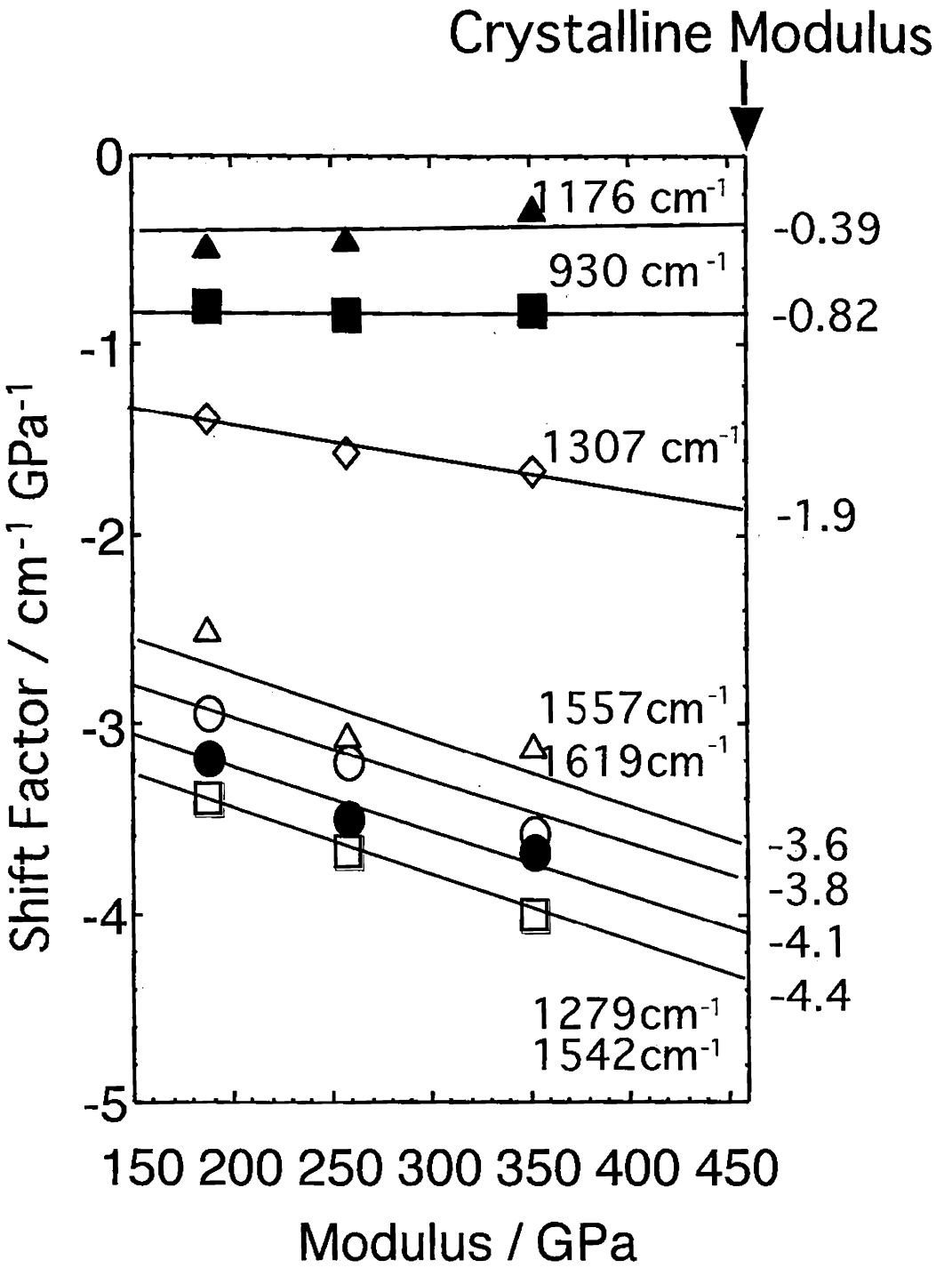

Figure 7-5. Modulus dependence of Raman shift factor.

factors are compared with the theoretical calculation[27,28] as will be described in a later section.

The band broadening is also related to the stress distribution in the fiber.[102] In Figure 7-2, the band profile was found to become broader as the applied tensile stress was increased. The estimated FWHMs are plotted as a function of stress in Figure 7-6. Most of the bands broaden with increasing stress, but a few peaks keep the same FWHMs. It implies that the stress distribution in the fiber becomes broader with increasing stress. It is found that the bands giving smaller broadening show smaller shift factors. This increasing rate of the FWHM may work as a measure to express how the broadening of the stress distribution is increased with increasing stress. In Figure 7-7 is shown the plot of this parameter against the fiber modulus. The plot is also extrapolated to the limit of crystalline modulus (460 GPa) in Chapter 3. If the broadening parameter represents only the increasing rate of stress distribution inside the fiber, the extrapolation to the crystalline modulus value should give the null value to FWHM for all the bands. But, in the actual case, some bands fall into zero FWHM and some have still non-zero FWHM. One reason might come from the usage of the observed crystalline modulus in this extrapolation : even the crystalline modulus itself shows the morphology dependence. Besides, the Raman bands should have their own intrinsic widths originating from the limited life time of thermal vibrations. We need further study about this problem.

7. 4. Analysis and Discussion

7. 4. 1. Normal Mode Calculation under Quasi-harmonic Approximation

In this section, theoretical calculation is made for the Raman band shift. As for the theoretical equations, only the outline will be presented here because the details have been described already in references.[27,28] The normal-mode frequencies are

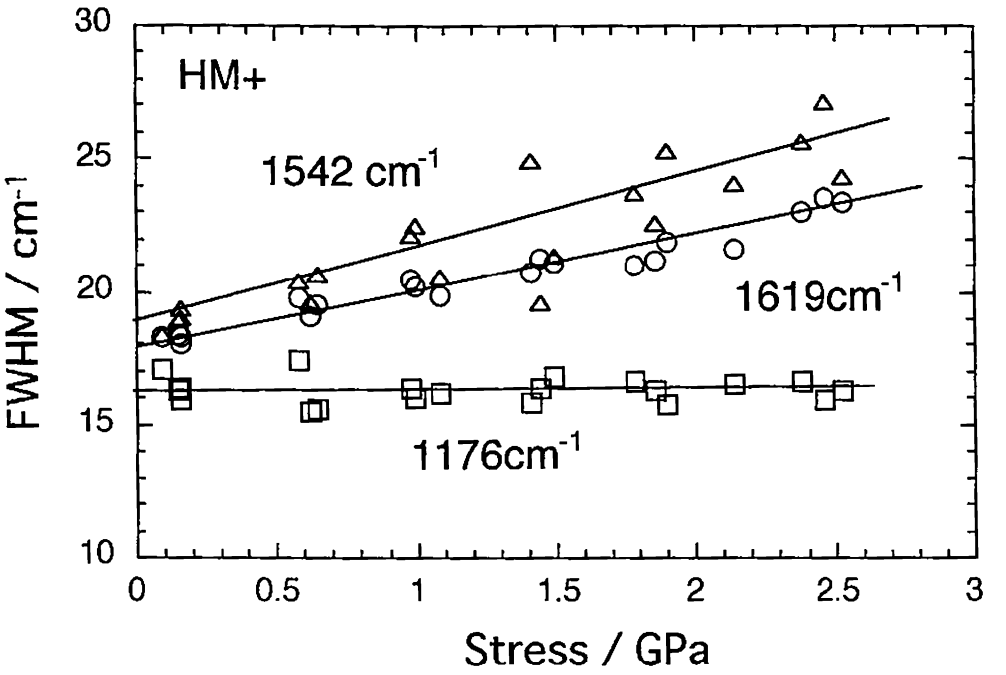

Figure 7-6. Stress dependence of FWHM evaluated for the HM+ sample.

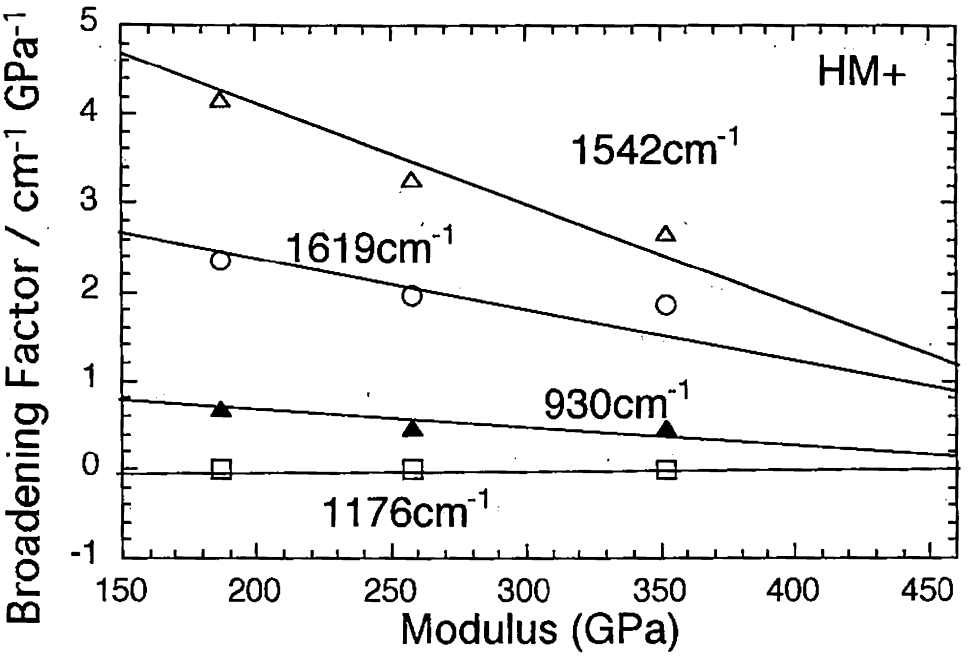

Figure 7-7. Modulus dependence of Raman broadening factor obtained for the HM+ sample.

obtained by solving the following equation,

$$\mathbf{D}_x \mathbf{L}_x = \Lambda_x \mathbf{L}_x \qquad (7\text{-}1)$$

where Λ_x is an eigenvalue matrix and $\mathbf{L}_x$ is an eigenvector. The dynamical matrix $\mathbf{D}_x$ is expressed as

$$\mathbf{D}_x = {}^t\mathbf{M}^{-1/2}\, {}^t\mathbf{B}_{op}\, \mathbf{F}_R\, \mathbf{B}_{op}\, \mathbf{M}^{-1/2} \qquad (7\text{-}2)$$

$\mathbf{B}_{op}$ is a B matrix which relates the internal displacement coordinates $\Delta\mathbf{R}_{vib}$ to the Cartesian displacement coordinates $\Delta\mathbf{X}_{vib}$ as $\Delta\mathbf{R}_{vib} = \mathbf{B}_{op}\, \Delta\mathbf{X}_{vib}$ where the "vib" denotes the quantities relating to spectroscopically active normal mode vibrations. $\mathbf{F}_R$ is a force constant matrix representing interactions among the internal displacement coordinates. $\mathbf{M}$ is a diagonal matrix consisting of atomic masses. The superscript "t" indicates the transpose of the matrix. Under the quasiharmonic approximation the force constant $\mathbf{F}_R$ is assumed to be a linear functions of $\Delta\mathbf{R}$ as expressed below.

$$F_{ij} = F_{0ij} + \Sigma F'_{ijk} \Delta R_k \qquad (7\text{-}3)$$

In this equaion the ΔR_k is the k th component of $\Delta\mathbf{R}$, the internal displacement coordinates due to the mechanical deformation. The F'_{0ij} is a harmonic force constant term to represent the interaction between the ΔR_i and ΔR_j. ΔR_i is given as a function of strain ε (or stress σ) by

$$\Delta\mathbf{R} = [\, - {}^t\mathbf{B}_\rho (\mathbf{F}_\rho)^{-1}\, \mathbf{F}_{\rho\varepsilon} + \mathbf{B}_\varepsilon \,]\, \varepsilon \qquad (7\text{-}4)$$

By putting the F_{ij} given by equations (7-3) and (7-4) into equations (7-1) and (7-2), the vibrational frequency can be calculated as a function of applied stress. That is, we can say that the mechanical deformation gives the $\Delta \mathbf{R}$, which affects the $\mathbf{F}_R$ and then the vibrational frequencies. Therefore the vibrational frequency is expressed as a function of stress σ as follows.

$$\nu = \nu_0 + \alpha\sigma \tag{7-5}$$

where α is a frequency shift factor. The calculation was made by using the set of force constants and the atomic coordinates reported in references[32,39] with a slight modification, which are listed in Table 7-2.

7. 4. 2. Comparison with the Observed Data

In order to compare the calculated results of the normal-mode frequencies with the observed data, the factor group analysis was made. Since the PBO chain in the crystalline region takes essentially the planar structure,[38,39] the analysis was made for this planar model. In this case the factor group is isomorphous to the point group C_{2v}. The vibrational modes can be classified into the following four symmetry species,

$$\begin{aligned}\Gamma = {} & 23A_1(\perp, \alpha'_{xx}, \alpha'_{yy}, \alpha'_{zz}) + 10A_2(\alpha'_{yz}) \\ & + 12B_2(\perp, \alpha'_{xy}) + 23B_2(/\!/, \alpha'_{xz})\end{aligned} \tag{7-6}$$

where $\perp$ and // are, respectively, the directions of the transition dipoles perpendicular and parallel to the chain axis and α'_{ij} is the ij-component of transition polarizability tensor. In order to assign the bands to these symmetry species, the polarized infrared and Raman spectra were measured. For the polarized infrared spectral measurements,

Table 7-2. Force constants for normal mode calculation.

Coordinates[a] Involved	Harmonic	Unharmonic
1. Stretching	(mdyn/Å)	(mdyn/Å^2)
1-2	6.433	-0.9
4-19	5.055	-0.9
12-20	5.055	-0.9
10-12	6.03	-0.9
5-7	6.0	-0.5
9-11	5.22	0.1
8-10	6.4	0.1
2. Bending	(mdyn Å/rad^2)	(mdyn Å/rad^3)
1-2-4	0.934	-0.25
4-5-7	0.75	-0.15
7-9-11	1.14	-0.15
7-8-10	1.96	-0.15
8-7-9	1.41	-0.15
9-11-10	1.96	-0.15
8-10-11	1.72	0.15
11-10-12	0.907	-0.25
10-12-14	0.937	-0.25
9-11-13	0.727	0.15
19-4-5	0.511	0.13
20-12-10	0.511	0.14
C-H(Out-of-plane)	0.2	-4000
3. Skeletal Torsion	(mdyn Å/rad^2)	(mdyn Å/rad^3)
all the skeletal bonds	0.1	-0.1
4. Stretch-Stretch	(mdyn/Å)	
1-2,2-4	0.75	-
1-2,4-5	-0.32	-
1-2,5-6	0.31	-
4-5,5-7	0.49	-
7-9,9-11	0.56	-
10-12,12-14	0.758	-
9-11,11-13	0.614	-
8-10,10-12	0.614	-
7-8,7-9	0.478	-

5-7,7-9	0.70	-
9-11,10-11	0.70	-
7-8,8-10	0.70	-
8-10,10-11	1.05	-
5-7,7-8	1.05	-
7-8,9-11	-0.20	-
10-11,10-12	0.758	-
7-9,10-11	-0.20	-
10-12,11-13	-0.242	-
10-11,15-17	-0.169	-
10-12,13-15	0.30	-
10-11,14-15	-0.069	-
8-10,14-15	-0.069	-
9-11,13-15	-0.122	-
9-11,10-12	0.146	-
8-10,11-13	0.146	-
9-11,10-12	0.146	-
7-9,12-14	0.03	-
5. Stretch-Bend	(mdyn/rad)	
1-2,1-2-4	0.3	-
5-4,5-4-19	0.14	-
7-9,7-9-11	0.80	-
7-8,7-8-10	0.85	-
10-11,11-10-12	0.85	-
8-10,8-10-11	0.85	-
10-12,10-12-14	0.414	-

a : The number indicates atoms in the repeat unit shown below.

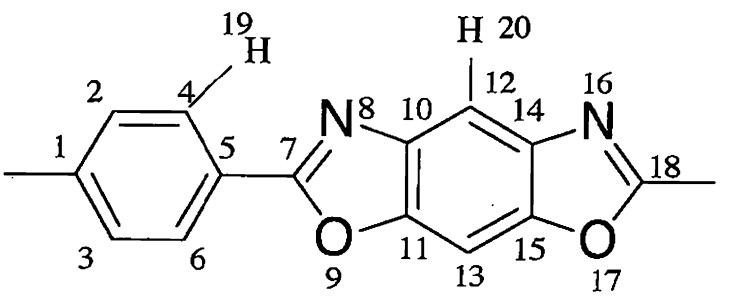

the PBO fiber was rolled to get a small flat film. The infrared spectra were measured by using an infrared microscope (Spectra Tech Ir μ S/SIRM). The obtained spectra are shown in Figure 7-8. The result is tabulated in Table 7-1. The polarized Raman spectra were also tried to measure but could not be obtained because of the polarization scrambling due to the turbidity of the fibers.

In Table 7-1 are summarized the thus calculated normal-mode frequencies and the corresponding frequency shifts. As seen in this table, the agreement between the observed and calculated frequencies is fairly good. At the same time the crystalline modulus was calculated to give the value 458 GPa, which is comparable to the measured values of 460 – 480 GPa.[33,34] The calculated shift factors α are shown in Table 7-3. Agreement between the observed and calculated values is also good. In this way, the Raman band shift can be reproduced reasonably by taking into account the anharmonic effect of vibrations. As reported in the previous papers,[27,28] the Raman shift factor is a function of the molecular geometry and the harmonic and anharmonic force constants. An internal coordinate showing higher efficiency for stretching a polymer chain shows higher frequency shift of the corresponding vibrational band. At the same time, if the anharmonicity is larger for this vibrational mode, the shift factor becomes furthermore larger. For example, the band at 1619 cm^{-1} was assigned to the stretching mode of the phenylene and benzothiazole rings coupled with the stretching mode of CC bond connecting these two rings. This band is shifted at the observed and calculated rates of –3.80 cm^{-1}/GPa and –4.04 cm^{-1}/GPa, respectively. This relatively large shift factor is considered to come from the high efficiency of these stretching modes for the chain deformation as well as the high anharmonity of the electronically conjugated ring structure. On the other hand, the band at 930 cm^{-1} is assigned to the CH out-of-plane deformation mode of phenylene ring and has the shift factor of –0.82 cm^{-1}/GPa (the calculated value -0.39 cm^{-1}/GPa). This relatively small shift factor is

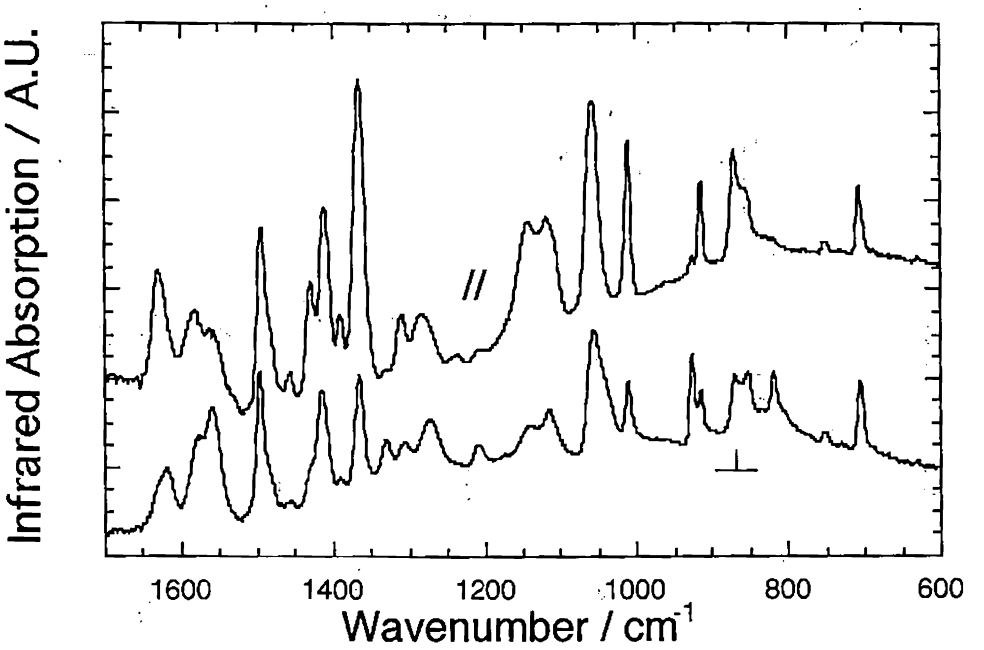

Figure 7-8. Infrared spectra of the rolled PBO AS fiber. // and ⊥ are, respectively, the directions of the transition dipoles parallel and perpendicular to the chain axis.

Table 7-3. Raman shift and broadening factors.

Frequency	Shift Fctor					Broadening Factor			
cm^{-1}	cm^{-1}/GPa					cm^{-1}/GPa			
	AS	HM	HM+	Extrapolated	Calculated	AS	HM	HM+	Extrapolated
1619	-2.93	-3.20	-3.57	-3.8	-4.04	2.36	1.96	1.87	1.44
1586	-	-	-	-	-3.93	-	-	-	-
1557	-2.49	-3.05	-3.12	-3.6	-4.46	0.00	0.00	0.00	0.00
1542	-3.40	-3.67	-4.00	-4.4	-4.42	4.17	3.27	2.67	1.50
1488	-3.45	-4.00	-4.41	-4.9	-3.05	-	-	-	-
1336	-	-	-	-	-0.94	-	-	-	-
1307	-1.38	-1.56	-1.66	-1.9	-1.34	0.27	0.00	0.00	0.00
1279	-3.17	-3.50	-3.67	-3.8	-2.39	4.45	2.67	2.43	0.60
1208	-	-	-	-	-0.56	-	-	-	-
1176	-0.47	-0.43	-0.27	-0.39	-0.94	0.00	0.00	0.00	0.00
1168	-0.45	-0.39	-0.43	-0.43	-0.94	-0.41	-0.34	-0.34	-0.36
930	-0.8	-0.84	-0.82	-0.82	-0.39	0.69	0.48	0.46	0.55
822	0.00	0.00	-	0.00	-0.41	-	-	-	-
795	-	-	-	-	0.16	-	-	-	-
755	0.00	0.47	-	0.25	-0.27	-	-	-	-
728	-0.6	-0.77	-	-0.70	-0.34	-	-	-	-
487	-1.12	-1.3	-1.41	-1.5	-0.62	-	-	-	-
215	-	-	-	-	-0.41	-	-	-	-

considered to relate with the origin of this band. The CH out-of-plane mode does not contribute very much to the effective stretching of the skeletal chain.

As pointed out already, the Raman shift factor and band broadening are dependent on the sample used for the Raman measurement. If the so-called homogeneous distribution of stress can be applied to these samples, the Raman shift factors should be constant in spite of the sample history. In other words the PBO fibers are considered to have the heterogeneous stress distribution depending on the morphology.

7. 4. 3. Raman Shift Factor and Morphology of Fibers

In order to understand this morphological effect on the Raman shift factor, a mechanical series-parallel model was introduced here. In the cases of POM and PE, as reported by Tashiro et al.,[98] the morphology-dependent shift factor could be interpreted on the basis of this mechanical mode. The Raman shift factor decreased with an increment of the bulk modulus, being explained reasonably by assuming a concentration of stress on the part of crystalline tie chains. In this interpretation the amorphous part was assumed not to contribute to the Raman bands tabulated in the analysis, because these observed bands come mainly from the crystalline region. In PBO case, on the other hand, Raman band shift factor was smaller for the sample of lower fiber modulus, quite contrast (opposite) to the case of POM and PE. PBO fiber is made of rigid-rod chains. Therefore, it is assumed that the chains in the amorphous part may take the extended form, which contributes more or less to the Raman scattering as the crystalline part does. In the amorphous region the parallel packing of the rigid chain segments seems difficult and so these chain segments do not contribute to the X-ray scattering from the crystal lattice.

According to a mechanical series-parallel model shown in Figure 7-9, the apparent crystalline modulus (E_c^{app}) and the bulk fiber modulus (E_{bulk}) are given as

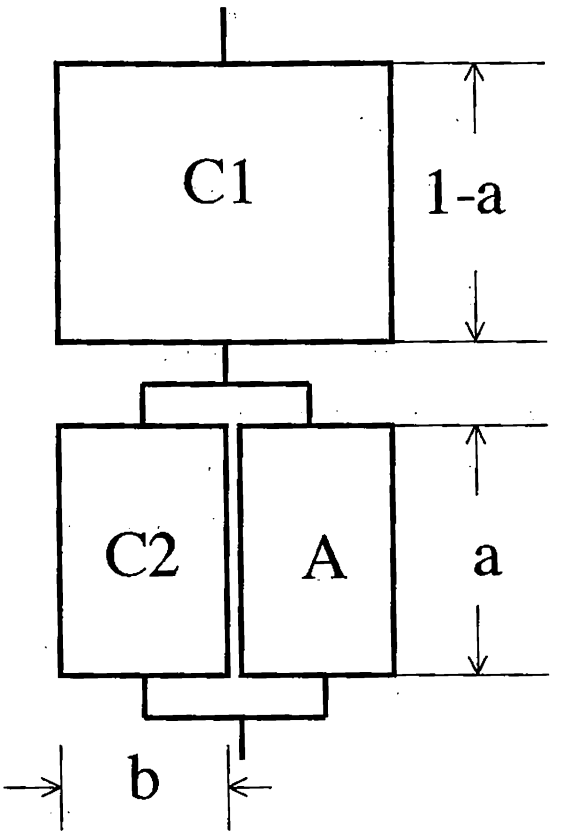

Figure 7-9. A mechanical series-parallel model. C1 and C2 stand for crystalline part and A for amorphous part.

follows.

$$E_c^{app} = E_c^{true}\, x \,/\, [1 - a + ab/(b + (1\text{-}b)E_a/\, E_c^{true})] \tag{7-7}$$

$$E_{bulk} = 1 \,/\, [\,(1\text{-}a) \,/\, E_c^{true} + a \,/\, (b\, E_c^{true} + (1\text{-}b)E_a)] \tag{7-8}$$

where E_c^{true} is a true Young's modulus of the crystalline part, E_a is a Young's modulus of the amorphous part, and the degree of crystallinity is given by $x = 1 - a + ab$. The parameters a and b are defined in Figure 7-9.

The observed Raman intensity $I(\nu)$ is assumed to be a summation of the intensity $i(\nu)$ for each vibrating oscillator or in proportion to the number of oscillators. If N oscillators exist in the crystalline region, then :

$$I(\nu) = N\, i(\nu) \tag{7-9}$$

In the low stress region, the observed Raman band is assumed to be an average of the bands ν_{C1}, ν_{C2} and ν_A, which come from the individual components of C1, C2 and A designated in Figure 7-9. The average frequency $<\nu>$ is expressed as follows :

$$<\nu> = \nu_0 + \alpha_C\, q\, \sigma_{bulk} \tag{7-10}$$

$$q = [b\, E_c^{true} + (1\text{-}b)E_a - a(1\text{-}b)\, E_a\, (1\text{-}\, \alpha_A/\, \alpha_C)]/[b\, E_c^{true} + (1\text{-}b)E_a]$$

where σ_{bulk} is the bulk stress, α_C is the Raman shift factor for the crystalline part and α_A is the factor for the amorphous part. The parameters a, b, E_c^{true}, E_a, α_C and α_A were adjusted so that the observed values of E_{bulk}, E_c^{app} and $<\nu>$ could be reproduced as reasonably as possible. The thus obtained parameters are tabulated in Table 7-4.

Table 7-4. Obtained suitable parameters for the series model.

E_c^{true}	GPa	460
E_a	GPa	70
α_C	cm^{-1} / GPa	-3.80
α_A	cm^{-1} / GPa	0.0

Table 7-5. The comparison between measured and calculated shift factors α

		AS	HM	HM+
E_{bulk}	GPa	187	258	352
a		0.26	0.14	0.055
b		0.0	0.0	0.0
α	cm^{-1} / GPa			
Measured		-2.93	-3.20	-3.57
Calculated		-2.80	-3.27	-3.59

The E_c^{app}, E_{bulk} and α ($=\alpha_C q$: apparent Raman shift factor) calculated for the models are tabulated in Table 7-5. The parameter b is almost zero for all the samples, indicating an application of the mechanical series model to PBO fibers. The parameter α_A, a shift factor of the amorphous band, is almost zero, too. In Chapter 3, measured apparent crystalline modulus differs slightly lower in AS (430 GPa) than in HM and HM+ but the result based on the simulation shows the constant value (460 GPa). Therefore the Raman band of the amorphous region is considered to contribute to the intensity of the crystalline band at the original frequency position. Figure 7-10 shows an illustration of the mechanical model of the PBO samples of AS, HM, and HM+. By increasing the quality of the PBO fiber from AS to HM and HM+, the contribution of the C phase is increased more reasonably, consistent with the observation of X-ray diffraction and electron microscope (Chapters 2 and 3). Because the amorphous region is assumed to contribute to the Raman bands but not to the X-ray scattering profile, the Raman shift factor is changed depending on the relative content of C and A parts but the crystalline modulus is essentially the same for the three types of fibers. They are also consistent with the observation.

7. 4. 4. Simulation of Vibrational Shift under Stress

The band profile of a vibrating oscillator $g(\nu)$ is assumed to be expressed by the following Lorentzian function.

$$g_i(\nu, \sigma) = g_0 / (\nu - \nu_{0i} + \alpha_i \sigma)^2 + r_i^2 \qquad (7\text{-}11)$$

where ν_{0i} is the peak frequency and $\alpha_i \sigma$ is the shift by stress σ. g_0/r_i^2 is the peak height and $2r_i$ is the half width. It is assumed that the crystalline (C1) and the amorphous (A) parts take the common original values for the peak frequency (ν_{0C} =

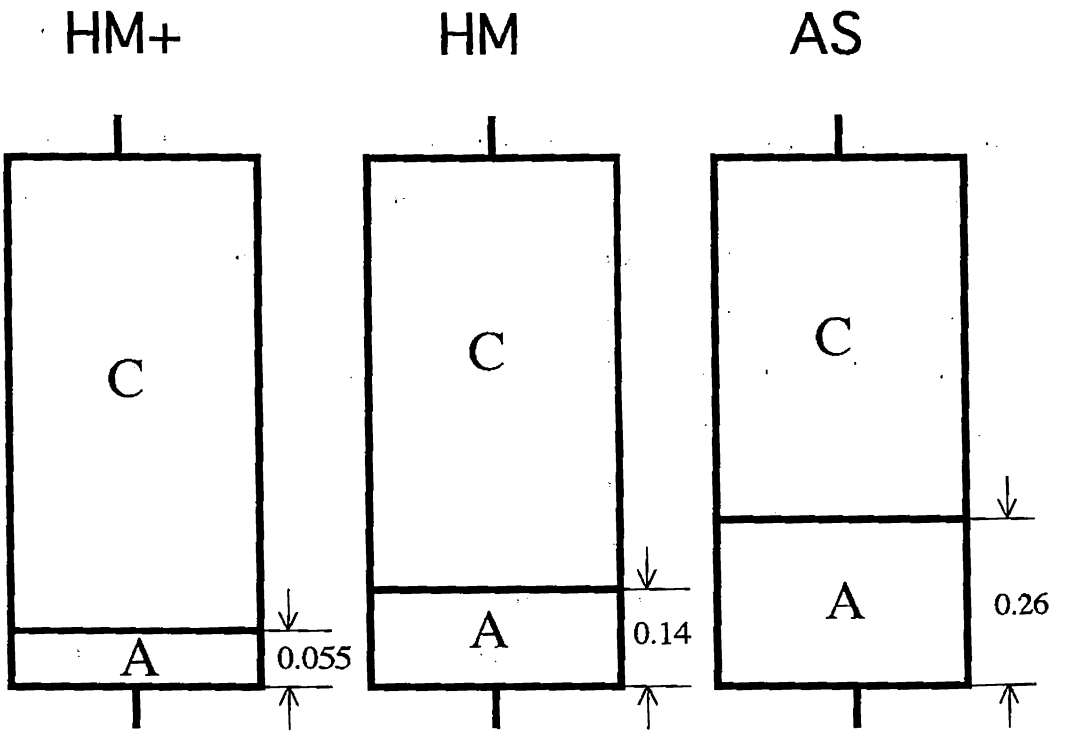

Figure 7-10. Estimated mechanical models for the three PBO fibers.

$\nu_{0A} = \nu_0$) and the halfwidth ($r_C = r_A = r$). The whole profile is the summation of the profiles of the crystalline and amorphous parts and is given by

$$G(\nu) = (1\text{-}a)g_{C1}(\nu, \sigma_{c\nu}) + ab\, g_{C2}(\nu, \sigma_{c2}) + a(1\text{-}b)\, g_A(\nu, \sigma_A)$$
$$= (1\text{-}a)g_C(\nu, \sigma_{bulk}) + a\, g_A(\nu, \sigma_{bulk}) \qquad (7\text{-}12)$$

where C1 is renamed as C. Because C2 component is actually null in the simulation, the C2 term is omitted and C1 is replaced with C in the following discussions. In this way, the profile $G(\nu)$ can be calculated as a function of applied stress σ_{bulk}. The result is shown in Figure 7-11. The profile becomes broader and asymmetric as the stress is increased, because the Raman scattering band from the crystalline part shifts toward lower frequency side while the band from the amorphous part stay at the same frequency. The FWHM is estimated at each stress and compared with the observed data as shown in Figure 7-12. In the case of AS sample, the predicted frequencies trace the actual data fairly well, but some discrepancy is detected for the HM and HM+ cases over 1 GPa of stress. In order to fulfill this gap, a larger value was assigned to r of the amorphous part and the FWHM was recalculated but the result was not improved. It is suggested that the actually-induced stress is more remarkable than our expectation from this model. Another reason may come from the assumption that band width r of the crystalline and amorphous parts is not changed by an applied stress : the Raman band of the oscillator may become broader as the stress is increased.

7. 5. Conclusions

In order to understand the mechanical deformation process of PBO fiber, the Raman spectra were measured under tensile force at room temperature. The evaluated shift factors were found to depend on the sample morphology. These shift factors

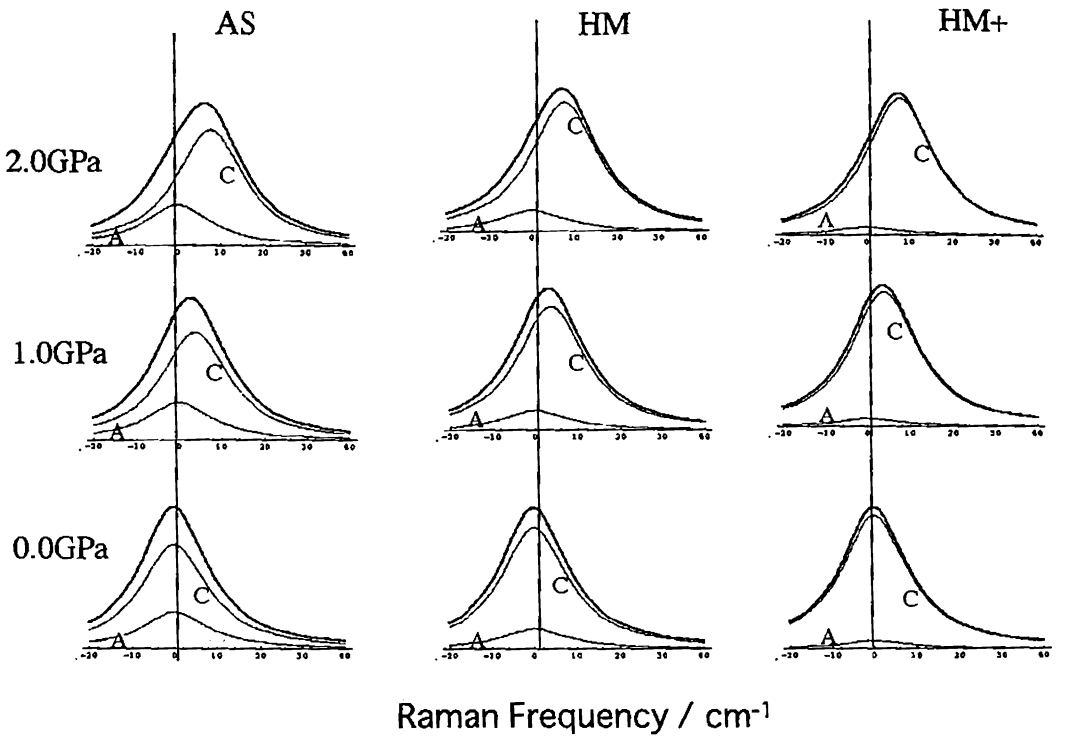

Figure 7-11. The result of simulating Raman band profiles. Thin line C represents from the crystalline part, A from the amorphous part. The thick line is the sum of the Raman spectral components of these two parts.

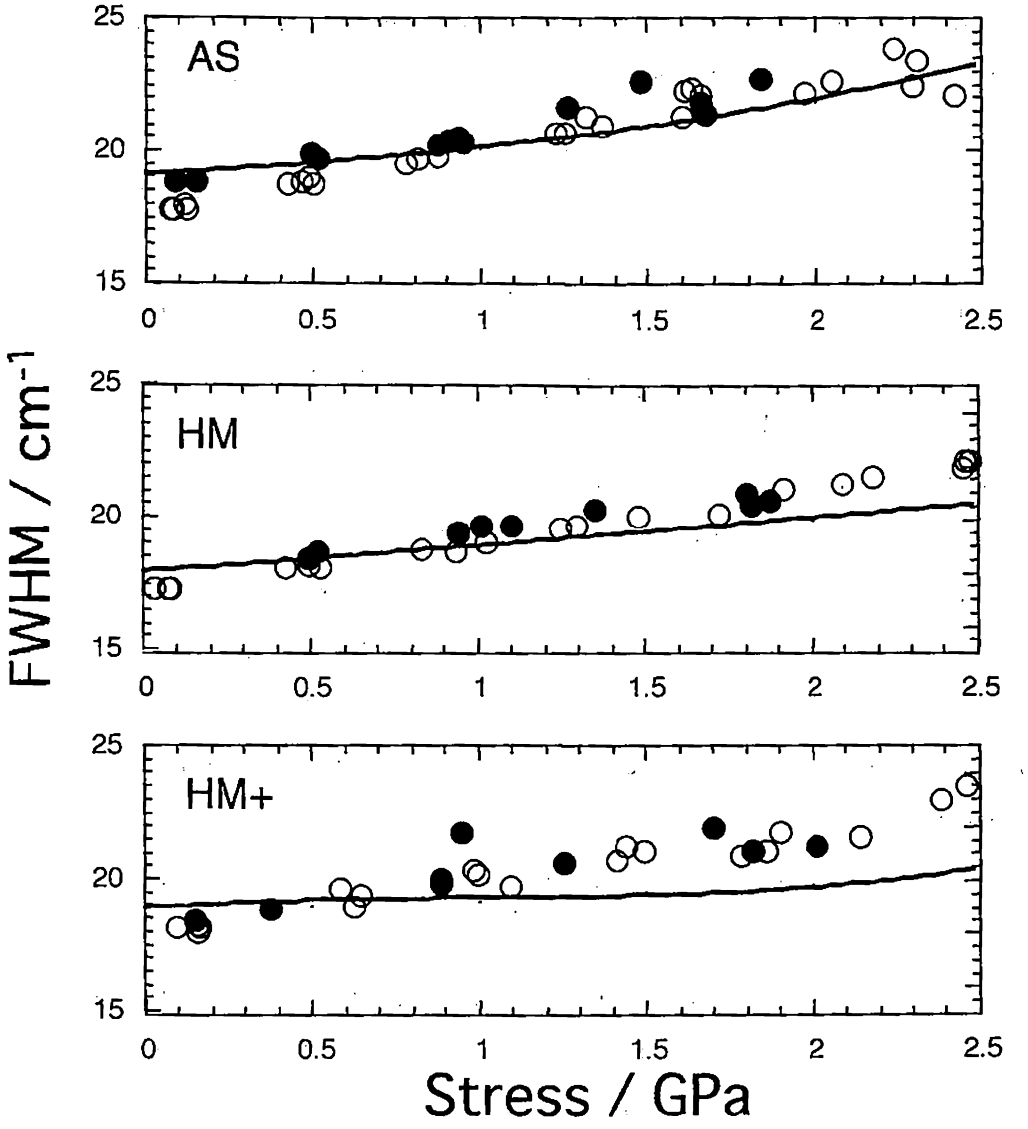

Figure 7-12. The comparison between estimated and measured FWHMs made for the various PBO fibers. ○ : measured on the loading process and ● : measured on the unloading process. Solid line : simulated result.

were plotted against the bulk modulus and the limiting shift factors were estimated by extrapolation of the observed data to the points corresponding to the pure crystalline state or the point of X-ray crystalline modulus. The theoretical calculation of the normal mode frequencies under the quasi-harmonic approximation gave the good reproduction of the obtained vibrational frequencies and their stress dependence. The Raman bands were observed to be broader for the sample of lower modulus and to increase their FWHM with increasing stress, implying an increase in the stress distribution within the sample. In this way the stress distribution was found to be very important in the Raman data analysis of PBO fibers. Then the mechanical series-parallel model was introduced, which consisted of the crystalline and amorphous phases, and the observed a set of E_{bulk}, E_c^{app} and Raman shift factor could be interpreted reasonably. As a result, the mechanical behavior was found to be treatable on the basis of so-called the mechanical series model of the crystalline and amorphous phases. The morphology-dependent Raman shift data could be interpreted reasonably by assuming that the amorphous chains contribute also to the Raman band profile, although the shift factor intrinsic of the amorphous phase is not so large as that of the crystalline phase.

PBO fibers show the highest Young's modulus among many types of commercial fibers. But, even this ultra-high-modulus fiber shows the stress distribution among the crystalline and amorphous regions. In order to get the PBO fiber with much higher Young's modulus, we need to control the morphology of this fiber so that the homogeneous stress distribution of totally crystalline state can be attained. This is an important and challengeable future problem.

Chapter 8
Concluding Remarks

This study is devoted to find a relationship between fiber modulus and structure of PBO fibers. Morphological features have been inspected by X-ray diffraction and electron microscopic methods in Chapters 2 and 3, in which an ultra-high modulus HM+ fiber was newly prepared by a non-aqueous coagulation method with a conventional heat treatment under tension. It is found that molecular orientation of the fiber as well as its structural inhomogeneity along the fiber axis is the factor to control fiber modulus.

In order to know the deformation mechanism of the fiber, X-ray diffraction patterns from the fiber under tensile stress were investigated and analyzed in Chapters 4 and 5. On the basis of Northolt's theory, apparent crystalline modulus and molecular orientation change induced by tensile force were evaluated from the changes in the position and half width of X-ray diffractions measured for the PBO fiber subjected to the tensile force. When the fiber is stretched, the molecular chains in the crystal region are stretched and the orientation angle of the molecular chains is changed. But the strains due to these molecular stretch and orientation change were found to be too small to cover the observed strains of the bulk fiber. At the present stage, however, this discrepancy of strains between the bulk fiber and the crystalline region cannot be explained well and requires us to search some additional factors. Based on Hosemann's paracrystal theory, ordering parameter for lattice distortion was also evaluated. This ordering parameter was found to decrease with an increase in the fiber modulus. Lattice distortion is thought to relate with the distribution of stress along the molecular chain and therefore with the structural inhomogeneity or the structural defects in the fiber. HM+ fiber was considered to contain very low concentration of defect

and low degree of structural inhomogeneity, giving the highest Young's modulus among the three types of fibers.

In Chapter 6, Raman spectroscopy was applied to clarify the relationship between the stress distribution in the fiber structure and the morphology. The Raman shift factor of the 1619 cm^{-1} band corresponding to phenylene ring vibration was investigated. It was understood that the shift factor strongly depends on the fiber modulus. It was also found that band-profile broadening occurs and the degree becomes higher as fiber modulus decreases, indicating that stress distribution is induced in the fiber structure and the rate also depends on inhomogeneity in the fiber structure.

In Chapter 7, normal-mode calculation under quasi-harmonic approximation was made and the Raman shift factor for PBO was also predicted. The measured values agree with the theoretically predicted values. Fiber modulus dependencies of the band shift and peak-profile broadening were treated with a mechanical series-parallel model. The model explains them fairly well but some further study is still needed to understand the stress distribution under strong tensile stress.

Over the whole study, it is well understood that mechanical properties strongly depend on fiber structure. From the analytical point of view, the exhibition of high modulus nature in PBO fiber is considered to come from its molecular geometry, strong chemical bonds (large force constants) and extended fiber structure along the fiber axis. The relationship between mechanical property and fiber structure could be quantitatively well interpreted with a mechanical series-parallel model. This study has told us many useful indications needed for the development of new polymer materials with excellent mechanical properties. The author believes a possibility of making novel polymers, the mechanical property of which exceeds remarkably that of PBO fiber in a near future.

References

1. M. G. Dobb, D. J. Johnson and B. P. Saville, *J. Polym Sci., Part B : Polym. Phys.*, **15**, 2201 (1977).
2. M. G. Dobb, D. J. Johnson and B. P. Saville, *J. Polym Sci., Polym. Symp.*, **58**, 237 (1977).
3. K. Yabuki, H. Ho and T. Ota, *Sen-i Gakkaishi*, **31**, T524 (1975).
4. M. G. Northolt, *Euro. Polym. J.* **10**, 799 (1974).
5. E. W. Choe and S. N. Kim, *Macromolecules*, **14**, 920 (1981).
6. J. Blackwell, R. A. Cageao and A. Biswas, *Macromolecules*, **20**, 667 (1987).
7. K. Ueda, *Sen-i Gakkaishi*, **43**, P135 (1987).
8. S. J. Krause, D. L. Vezie and W. W. Adams, *Polymer Comm.*, **30**, 10 (1989)
9. P. Smith and P. J. Lemstra, *J. Mater. Sci.*, **15**, 505 (1980).
10. T. Ohta, *Polym, Eng. Sci.*, **23**, 697 (1983).
11. L. Wamg, R. S. Porter and T. Kanamoto, *Polym. Comm.*, **31**, 457 (1990).
12. A. Zwijnenburg and A. J. Pennings, *Coll. Polym. Sci.*, **253**, 452 (1975).
13. B. Kalb and A. J. Pennings, *J. Mater. Sci.*, **15**, 2584 (1980).
14. A. K. Powell, G. Craggs and I. M. Ward, *J. Mater. Sci.*, **25**, 3990 (1990).
15. W. R. Busing, *Macromolecules*, **23**, 4608 (1990).
16. W. Wu, P. G. Simpson and W. B. Black, *J. Polym Sci., Part B : Polym. Symp.*, **18**, 751 (1980).
17. R. Hosemann, *Polymer*, **3**, 349 (1962).
18. A. Peterlin, *Text. Res. J.*, **42**, 20 (1972).
19. D. R. Ulrich, *Polymer*, **28**, 533 (1987).
20. L. R. Denny, I. J. Goldfarb and E. J. Soloski, *Mater. Res. Soc. Symp. Proc.*, **134**, 295 (1989).

21. T. Kuroki, Y. Tanaka, T. Hokudoh and K. Yabuki, J. *Appl. Polym. Sci.*, **65**, 1031 (1997).

22. T. Shimanouchi, M. Asahina and S. Enomoto, *J. Polym. Sci.*, **59**, 93 (1962).

23. Y. Shiro and T. Miyazawa, *Bull. Chem. Soc. Jpn.*, **44**, 2371 (1971).

24. K. Tashiro, M. Kobayashi and H. Tadokoro, *Macromolecules*, **11**, 908 (1978).

25. K. Tashiro, M. Kobayashi and H. Tadokoro, *Macromolecules*, **11**, 914 (1978).

26. K. Tashiro, *Kobunshi Ronbunshu*, **49**, 711 (1992).

27. K. Tashiro , G Wu and M. Kobayashi, *J. Polym. Sci., Part B : Polym. Phys.*, **28**, 2527 (1990).

28. K. Tashiro, S. Minami, G. Wu and M. Kobayashi, *J. Polym Sci., Part B : Polym. Phys.*, **30**, 1143 (1992).

29. G. C. Parrinello and U. W. Suter, *Polymer*, **32**, 2179 (1991).

30. K. Tashiro and M. Konayashi, *Polymer*, **37**, 1775 (1996).

31. S. G. Wierschke, J. R. Shoemaker, P. D. Haaland, R. Pachter and W. W. Adams, *Polymer*, **33**, 3357 (1992).

32. K. Tashiro and M. Kobayashi, *Macromolecules*, **24**, 3706 (1991).

33. P. G. Lenhert and W. W. Adams, *Mater. Res. Soc. Symp. Proc.*, **134**, 329 (1989).

34. T. Nishino, R. Matsui, K Nakamae, Y. Gotoh and M. Nagura, *Sen-i Gakkai Preprints*, **1995**, G-149 (1995).

35. S. J. Krause, T. B. Haddock, D. L. Vezie, P. G. Lenhert, W. –F. Hwang, G. E. Price, T. E. Helminiak, J. F. O'Brien and W. W. Adams, *Polymer*, **29**, 1354 (1988).

36. W. W. Adams, S. Kumar, D. C. Martin and K. Shimamura, *Polym. Comm.*, **30**, 285 (1989).

37. D. C. Martin and E. L. Thomas, *Macromolecules*, **24**, 2450 (1991).

38. A. V. Fratini, P. G. Lenhert, T. J. Resch and W. W. Adams, *Mater. Res. Soc. Symp.*

Proc., **134**, 431 (1989).

39. K. Tashiro, J. Yoshino, T. Kitagawa, H. Murase and K. Yabuki, *Macromolecules*, **31**, 5430 (1998).
40. Y. Takahashi, *Macromolecules*, **32**, 4010 (1999).
41. M. E. Hunsaker, G. E. Price and S. J. Bai, *Polymer*, **33**, 2128 (1992).
42. S. J. Bai and G. E. Price, *Polymer*, **33**, 2136 (1992).
43. S. J. Bai, *J. Polym. Sci., Part B : Polym. Phys.*, **32**, 2575 (1994).
44. S. Kumar, S. Warner, D. T. Grubb and W. W. Adams, *Polymer*, **35**, 5408 (1994).
45. R. J. Young, R. J. Day and M. Zakikhani, *J. Mater. Sci.*, **25**, 127 (1990).
46. D. C. Martin, *Macromolecules*, **25**, 5171 (1992).
47. K. Nakamae, T. Nishino, Y. Shimizu and T. Matsumoto, *Polym. J.*, **19**, 451 (1987).
48. K. Tashiro, M. Kobayashi and H. Tadokoro, *Macromolecules*, **10**, 413 (1977).
49. M. G. Northolt and J. J. V. Aartsen, *J. Poly, Sci., Polym. Symp.*, **58**, 283 (1977).
50. K. Suehiro, Y. Chatani and H. Tadokoro, *Polym. J.*, **7**, 352 (1975).
51. W. W. Adams, L. V. Azaroff and A. K. Kulshreshtha, *Zeitschrift fur Kristallographie*, **150**, 321 (1979).
52. W. J. Welsh, *Polym. Eng. Sci.*, **25**, 965 (1985).
53. D. Bhaumik, W. J. Welsh, H. H. Jaffe and J. E. Mark, *Macromolecules*, **14**, 951 (1981).
54. S. R. Allen, *Polymer*, **29**, 1091 (1988).
55. D. I. Green, A. P. Unwin, G. R. Davies and I. M. Ward, *Polymer*, **31**, 579 (1990).
56. D. B. Roitman, R. A. Wessling and J. McAlister, *Macromolecules*, **26**, 5174 (1993).
57. K. Shimamura, J. R. Minter and E. L. Thomas, *J. Mater. Sci. Let.*, **2**, 54 (1983).
58. K. Shimamura and A. Hashimoto, *Sen-i Gakkaishi*, **47**, P324 (1991).

59. M. G. Northolt, *Polymer*, **21**, 1199 (1980).

60. M. C. G. Jones and D. C. Martin, *Macromolecules*, **28**, 6161 (1995).

61. Y. Cohen and E. L. Thomas, *Polym. Eng. Sci.*, **25**, 1093 (1985).

62. Y. Cohen and E. L. Thomas, *Macromolecules*, **21**, 433 (1988).

63. Y. Cohen and E. L. Thomas, *Macromolecules*, **21**, 436 (1988).

64. Y. Cohen and W. W. Adams, *Polymer*, **13**, 2767 (1996).

65. V. I. Gerasimov, Y. V. Genin, A. I. Kitaigorodski and D. Y. Tsvankin, *Kolloid-Z. Z. Polym.*, **250**, 518 (1972).

66. K. Yabuki, M. Iwasaki and Y. Aoki, *Text. Res. J.*, **56**, 41 (1986).

67. C. Galiotis, R. T. Read, P. H. Yeung and R. J. Young, *J. Polym. Sci., Part B : Polym. Phys.*, **22**, 1589 (1984).

68. R. J. Young, D. Lu, R. J. Day, W. F. Knoff and H. A. Davis, *J. Mater. Sci.*, **27**, 5431 (1992).

69. H. Murase, T. Kitagawa and K. Yabuki, *Polym. Prep. Jpn.*, **47(13)**, 3605 (1998).

70. R. H. Ericksen, *Polymer*, **26**, 733 (1985).

71. T. Ii, K. Tashiro, M. Kobayashi and H. Tadokoro, *Macromolecules*, **20**, 347 (1987).

72. T. Ii, K. Tashiro, M. Kobayashi and H. Tadokoro, *Macromolecules*, **20**, 552 (1987).

73. S. R. Allen and E. J. Roche, *Polymer*, **30**, 996 (1989).

74. B. Chu, C. Wu, Y. Li, S. R. Allen, T. F. Mcnulty and J. C. Phillips, *J. Polym. Sci., Part C : Polym. Let.*, **28**, 227 (1990).

75. K. Prasad and D. T. Grubb, *J. Polym Sci., Part B : Polym. Phys.*, **27**, 381 (1989).

76. R. S. Bretzlaff and R. P. Wool, *Macromolecules*, **16**, 1907 (1983).

77. R. P. Wool, R. S. Bretzlaff, B. Y. Li, C. H. Wang and R. H. Boyd, *J. Polym. Sci., Part B : Polym. Phys.*, **24**, 1039 (1986).

78. R. J. Day, I. M. Robinson, M. Zakikhani and R. J. Young, *Polymer*, **28**, 1833 (1987).

79. M. G. Northolt and R. v. d. Hout, *Polymer*, **26**, 310 (1985).

80. M. G. Northolt, J. J. M. Baltussen and B. Schaffers-Korff, *Polymer*, **36**, 3485 (1995).

81. I. Sakurada and Y. Nukushina, *J. Polym. Sci.*, **57**, 651 (1962).

82. S. v. d. Zwaag, N. G. Northolt, R. J. Young, I. M. Robinson, C. Galiotis and D. N. Batchelder, *Polym. Comm.*, **28**, 276 (1987).

83. B. J. Kip, M. C. P. V. Eijk and R. J. Meier, *J. Polym. Sci., Part B : Polym Sci.*, **29**, 99 (1991).

84. J. A. H. M. Moonen, W. A. C. Roovers, R. J. Meier and B. J. Kip, *J. Polym. Sci., Part B : Polym Sci.*, **30**, 361 (1992).

85. W. F. Wong and R. J. Young, *J. Mater. Sci.*, **29**, 510 (1994).

86. W. F. Wong and R. J. Young, *J. Mater. Sci.*, **29**, 520 (1994).

87. A. M. Hindeleh, R. Hosemann, G. Hinrichsen and H. Springer, *Polymer*, **31**, 205 (1990).

88. A. M. Hindeleh and R. Hosemann, *J. Mater. Sci.*, **26**, 5127 (1991).

89. K. Prasad and D. T. Grubb, *J. Polym. Sci., Part B : Polym Phys.*, **28**, 2199 (1990).

90. Y. Termonia, P. Meakin and P. Smith, *Macromolecules*, **18**, 2246 (1985).

91. Y. Termonia and P. Smith, *Polym. Comm.*, **28**, 60 (1987).

92. Y. Termonia and P. Smith, *Polymer*, **27**, 1845 (1986).

93. P. Smith and Y. Termonia, *Polym. Comm.*, **30**, 66 (1989).

94. D. H. Reneker and J. Mazur, *Polymer*, **29**, 3 (1988).

95. G. M. Venkatesh, D. Y. Shen and S. L. Hsu, *J. Polym. Sci., Part B : Polym. Phys.*, **19**, 1475 (1981).

96. K. Tashiro and M. Kobayashi, *Sen-i Gakkaishi*, **43**, 78 (1987).

97. P. K. Kim, C. Chang and S. L. Hsu, *Polymer*, **27**, 34 (1986).

98. K. Tashiro, G. Wu and M. Kobayashi, *Polymer*, **29**, 768 (1988).

99. J. Sirichaisit and R. J. Young, *Polymer*, **40**, 3421 (1999).

100. R. J. Young and P. P. Aug, *Polymer*, **33**, 975 (1992).

101. W. –Y. Yeh and R. J. Young, *Polymer*, **40**, 857 (1998).

102. W. –Y. Yeh and R. J. Young, *J. Macromol. Sci., Phys.*, **B37**, 83 (1998).

103. J. Young and W. –Y. Yeh, *Polymer*, **35**, 3844 (1994).

104. N. Melanitis and C. Galiotis, *J. Mater. Sci.*, **25**, 5081 (1990).

105. N. Melanitis, P. L. Telow, C. Galiotis and S. B. Smith, *J. Mater. Sci.*, **29**, 786 (1994).

List of Publications

The contents of this thesis have been or will be published in the following papers.

1. Structural Study on Poly-*p*-phenylenebenzobisoxazole (PBO) Fiber, T. Kitagawa, H. Murase and K. Yabuki, *J. Polym. Sci., Part B : Polym. Phys.* **36**, 39 (1998).
2. An Analysis of Deformation Process on Poly-*p*-phenylenebenzobisoxazole (PBO) Fiber and a Structural Study of the New High-modulus Type PBO HM+ Fiber, T. Kitagawa, M. Ishitobi and K. Yabuki, *J. Polym. Sci., Part B : Polym. Phys.* **38**, 1605 (2000).
3. An Investigation into the Relationship between Internal Stress Distribution and a Change of Poly-*p*-phenylenebenzobisoxazole (PBO) Fiber Structure, T. Kitagawa and K. Yabuki, *J. Polym. Sci., Part B : Polym. Phys.* **38**, 2901 (2000).
4. A Relationship between the Stress Distribution and the Peak Profile Broadening of Meridional X-ray Diffraction from Poly-*p*-phenylenebenzobisoxazole (PBO) Fiber, T. Kitagawa and K. Yabuki, *J. Polym. Sci., Part B : Polym. Phys.* **38**, 2937 (2000).
5. An Investigation into the Relationship between Processing, Structure and Properties for High-modulus PBO Fibers, Part 1. Raman Band Shift and Broadening with tension and Compression, T. Kitagawa, K. Yabuki and R. J. Young, *Polymer*, **42**, 2101 (2001).
6. An Investigation into the Relationship between Processing, Structure and Properties for High-modulus PBO Fibers, Part 2. Hysteresis Effect on Raman Band Shift and Peak Broadening with Strain and Skin-core Structure Analysis of Selected-area Electron Diffraction with Ultramicrotome Technique, T. Kitagawa, K. Yabuki and R. J. Young, *J. Macromol. Sci., Phys.* under submission
7. An Investigation into the Relationship between Processing, Structure and

Properties for High-modulus PBO Fibers, Part 3 Fiber Structure Analyses with using Transmission Electron Microscopy, T. Kitagawa, K. Yabuki, A. C. Wright and R. J. Young, *Polymer*, in preparation

8. Stress Distribution in PBO Fiber as Viewed from Vibrational Spectroscopic Measurement under Tension, T. Kitagawa, K. Tashiro and K. Yabuki, *Macromolecules*, in preparation

Other related papers

1. An Analysis of Capillary Water Behavior in Poly-*p*-phenylenebenzobisoxazole (PBO) Fiber, T. Kitagawa and K. Yabuki, *J. Appl. Polym. Sci.*, in press.